Enhanced Dynamics at the Free Surface of a Molecular Glass Film

by

Chad Daley

A thesis
presented to the University of Waterloo
in fulfillment of the
thesis requirement for the degree of
Master of Science
in
Physics

Waterloo, Ontario, Canada, 2010

I hereby declare that I am the sole author of this thesis. This is a true copy of the thesis, including any required final revisions, as accepted by my examiners.

I understand that my thesis may be made electronically available to the public.

Abstract

In this thesis we describe two separate experiments involving the use of gold nanoparticles. The first experiment looks at the use of gold nanoparticles as a localized heat source and the potential application as a cancer treatment. The second experiment, which is the real focus of this thesis, applies gold nanoparticles in the study of the free surface dynamics of glassy thin films.

Gold nanoparticles have the ability to strongly absorb the energy in an incident laser beam and convert that energy into heat. Photothermal therapy is a proposed cancer treatment which exploits this ability to irreparably damage cancerous tissues surrounding gold nanoparticles. In the first chapter of this thesis we explain an experiment designed to probe the local temperatures achieved in such a process. Gold nanoparticles are used to stabilize the boundary of an inverse micelle system which contains an aqueous fluorescent dye solution on it's interior. A temperature dependent fluorescence intensity allows us to probe the temperature changes induced by laser irradiation.

In the remainder of this thesis we describe a separate experiment involving the use of gold nanoparticles to study the free surface dynamics of thin glassy films. There is a growing body of evidence in the literature that thin polymer films in the glassy state exhibit heterogeneous dynamics; specifically that the first few nanometers from an air-polymer interface exhibit enhanced mobility relative to the interior of the film. The underlying mechanism responsible for this enhanced mobility remains elusive, however some believe it to be a direct consequence of the polymeric nature of these films. We describe in detail an experiment aimed at addressing this concern. We deposit gold nanoparticles onto the surface of a molecular (non-polymeric) glassy film and monitor their behaviour upon heating using atomic force microscopy. Our results clearly show the existence of enhanced surface mobility in the system studied and provide strong evidence that enhanced surface mobility should be expected in all glass forming systems.

Acknowledgments

I would like to acknowledge all those who have helped in my research. For their helpful advice and assistance I thank my coworkers Zahra Fakhraai, Dongping Qi, Mark Ilton, Kanwarjeet Kaur, Ryan Speller, Jonathan Teichroeb, and James Benson. For their assistance in the role of my committee member I thank professors Zoya Leonenko, Qing-Bin Lu, and Roger Melko. Most importantly I thank my supervisor James Forrest for his guidance throughout.

Contents

List of Figures

Part I

PHOTOTHERMAL THERAPY

Chapter 1

Introduction

The first part of this thesis is dedicated to describing an experimental study of the local temperatures achieved in a process known as photothermal therapy. We begin this chapter with a discussion on the photothermal therapy technique and why an experimental study of the local temperatures is needed. The subsequent chapters describe the experimental details (2) and preliminary findings (3).

Photothermal therapy (PTT) is a promising cancer therapy which belongs to a larger class of treatments known as hyperthermia. The overall approach in hyperthermia cancer treatments is to cause destruction of cancerous cells through heating. In PTT the localized surface plasmon resonance of metallic nanoparticles (typically gold) is exploited in order to produce a localized heating in the vicinity of a nanoparticle. This effect can be used to cause selective destruction of cancerous tissue in a biological system if the nanoparticles can be accumulated at the cancerous site. This can be achieved by conjugating the nanoparticle surface with antibodies which are specific to receptors expressed in cancerous cells. Irradiation of the cancerous tumor at the resonant wavelength of the nanoparticles will then result in a highly localized heating effect leading to cell destruction. Although the technique has been shown to work, some fundamental issues remain unsolved, namely the magnitude of the local heating and the physical process through which cell destruction occurs. The present study aims to address these concerns by providing an experimental temperature measurement in a model system.

In this chapter we provide an introduction to the subject. We begin with a discuss on the process through which gold nanoparticles convert optical energy into heat. From there we

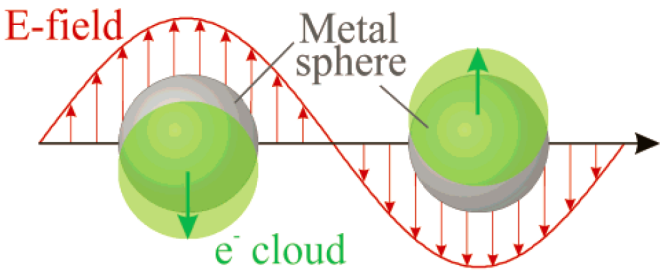

Figure 1.1: Illustration of the interaction between an electric field and a metal nanoparticle. The conduction electrons are displaced which creates an oscillating polarization across the sphere. Image reproduced from [1].

discuss some of the practical aspects of designing a photothermal therapy experiment; the choice of nanoparticle and the targeting of cancerous cells. Finally we turn to the literature for a discussion of the existing estimates of the local temperatures and the physical process which leads to cell destruction.

1.1 Localized Surface Plasmon Resonance

Surface plasmons refers to the collective excitation of conduction electrons in planar metal systems. This collective excitation is in the form of an electron density wave formed at the surface boundary, at the resonant frequency these excitations are greatly enhanced. Localized surface plasmon is a related process in metallic nanoparticles rather than metallic planar surfaces. In a localized surface plasmon process an oscillation of the conduction electrons is induced in the nanoparticle, figure 1.1. When applied in the role of a localized heat source in PTT this resonance effect gives gold nanoparticles many advantages over therapies using conventional organic dyes; their absorption coefficient is orders of magnitude larger than conventional dyes which means a much lower laser intensity can be used thereby minimizing the damage to the surrounding environment, and they are much more stable against photobleaching. The resonant frequency for this process is heavily dependent on the size and shape of the nanoparticle. Figure 1.2 shows a plot of absorbance as a function of wavelength for spherical gold nanoparticles of three different sizes. Two points to notice about this plot; a rather large shift towards longer wavelengths is found

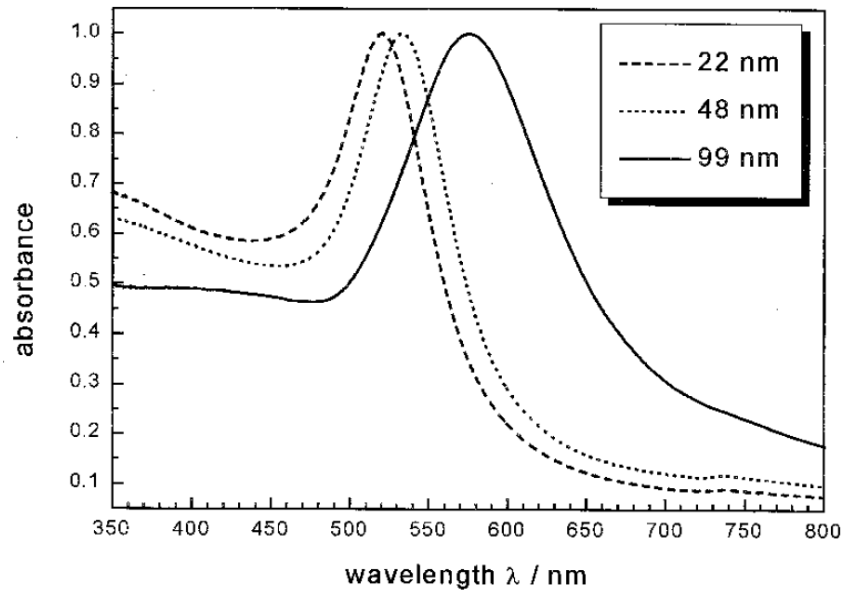

Figure 1.2: Plot of absorbance as a function of wavelength for three spherical nanoparticles of different sizes. Image reproduced from [2].

as the nanoparticle size is increased, and the absorption peak broadens with increasing nanoparticle size. This behaviour can be understood in the context of the Mie theory. A full discussion of the Mie theory is not required but a brief qualitative discussion following that of Link et al. is provided [2]. Mie theory looks for a solution to Maxwell's equations for the interaction between a small sphere and an electromagnetic field. Series solutions for the extinction, scattering, and absorption cross sections are obtained in terms of the order of oscillations (ie. dipole, quadrupole, etc.). In the small sphere limit ($\sim$ 20 nm) the dipole approximation can be made and only the term representing the dipole oscillations of electrons is retained. As the sphere size is increased so does the relative contributions of the higher order terms in the series solution. This can be intuitively understood as an increase in the difficulty of creating a uniform polarization across the whole nanoparticle. As these higher order modes enter at lower energies, this leads to both a shift to lower energies and a broadening of the absorption peak.

Following an excitation of the conduction electrons via absorption of incoming photons, a collective oscillation of electrons is induced. However this excitation will decay over time through collisions between the electron gas and the surrounding lattice, this decay typically

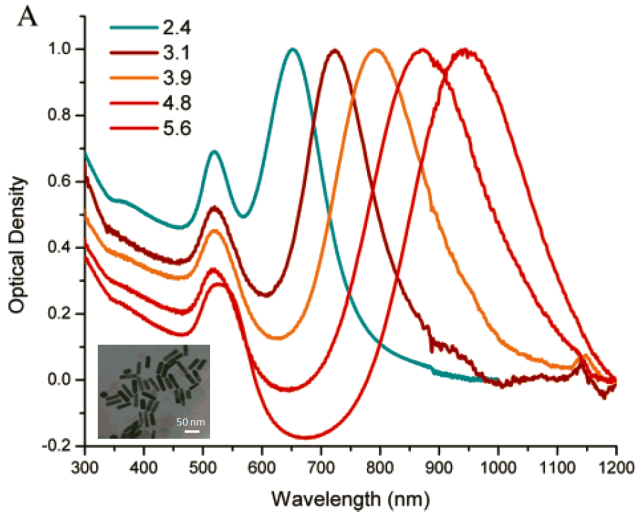

Figure 1.3: Series of absorption spectra for gold nanorods illustrating the changes in the spectrum as the aspect ratio of the nanorod is varied from 2.4 to 5.6. The inset shows a TEM image of nanorods with an aspect ratio of 3.9. Figure adapted from [3].

occurs on the timescale of picoseconds [2]. These collisions results in a transfer of energy into the lattice in the form of heat, and consequently an increase in the lattice temperature. This in turn will heat the surroundings as thermal equilibration is approached and heat diffuses away from the nanoparticles. It is through this process that the gold nanoparticles used in PTT studies can provide a localized heating of their surroundings.

1.2 Effect of Different Nanoparticle Size and Shapes

In the previous section we have seen how the resonant wavelength of gold nanoparticles depends on the size of the spheres. An additional factor which influences the shape of the absorption spectrum is the shape of the nanoparticles. Figure 1.3 shows a series of absorption spectra as the aspect ratio of gold nanorods is changed. Nanorods represent one of the many possible shapes that can be used to tune the absorption peak of the system, tetrahedra, cubes, cylinders, cages, and shells have also been studied [1, 4, 5, 6, 7] In designing a cancer therapy the wavelength of radiation must be chosen so as to maximize the effectiveness of the treatment while simultaneously minimizing unwanted damage to

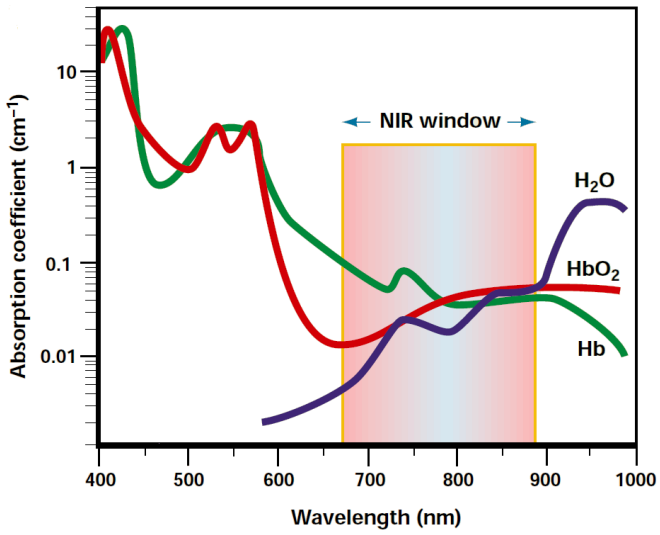

Figure 1.4: Plot of the absorption coefficients of the primary absorbers in native human tissue, water and hemoglobin. Image adapted from [8].

healthy tissues. Figure 1.4 plots the absorption coefficients of water and hemoglobin, the primary absorbers of light in human tissue from the visible to infrared regions. With this plot in mind we see that the optimal wavelength for an *in vivo* PTT application lies in the near-infrared range (NIR). Nanoshells, a thin gold shell surrounding a dielectric core, represent an interesting system because their scattering cross sections can also be tuned by varying the core and shell radii. This means that nanoshells can be designed which have both a large scattering cross section and an absorption peak in the NIR. The advantage of this is that the nanoshells can then be used simultaneously for heating and as a contrast agent for *in vivo* imaging.

1.3 Targeting Cancerous Cells

In order to avoid unwanted damage to healthy tissue during a PTT treatment, nanoparticles need to be targeted to bind primarily to the cancerous cells. This is a well developed technique used extensively in cellular imaging and bioassaying. Strategies here are either active or passive. In active targeting methods the strategy is to find a receptor which is either overexpressed or specific to the cancerous cells. Since a cell's normal functions

are inherently disrupted in the cancerous state, the structure of cancerous cells are often distinct from normal cells. This makes identification of a suitable receptor molecule possible. The nanoparticle surface is then functionalized with a molecule which has a high affinity of binding to the receptor. Typically an antibody-antigen pair are used due to the remarkable specificity of their interaction. Antigen-antibody pairs are naturally used in the human immune system, but with current techniques antibodies can be synthetically produced with a particular antigen specificity.

In passive targeting methods the differences in cellular structure between normal and malignant cells is exploited to achieve an accumulation of nanoparticles. Tumor blood vessels are found to have rather large pores which allow nanoparticles to pass into the tumor. The nanoparticles are injected into the vicinity of the tumor and a circulation time is introduced to give the nanoparticles time to accumulate. Figure 1.5 shows fluorescent images of tumor carrying mice following three different targeting schemes. The success of each strategy is indicated by the strength of the fluorescence signal at the tumor site. All three schemes modify the surfaces of the nanoparticles by attaching different molecules to the nanoparticle. The first two images use passive targeting with the first image using a larger group attached to the surface. The third image uses active targeting. We see that the passive targeting results in a lower accumulation of quantum dots at the tumor sites when compared to the active targeting. Comparing the first two images we see that a larger surface group results in lower accumulation at the tumor site; the nanoparticles have a tougher time penetrating into the tumors.

1.4 Temperature Estimates and Damage Mechanism

Although various studies have been published proving the viability of PTT as a way of selectively destroying cancerous tissues, two fundamental questions regarding the process remain unanswered; What is the physical mechanism through which cellular destruction occurs? And how large are the resultant temperature increases in the cellular tissue surrounding the nanoparticles? Although it is clear that cell death occurs as a result of local heating, the mechanism which is directly responsible for cell death is unknown. Several mechanisms have been proposed,

- Denaturation of cellular proteins leading to necrosis/apoptosis

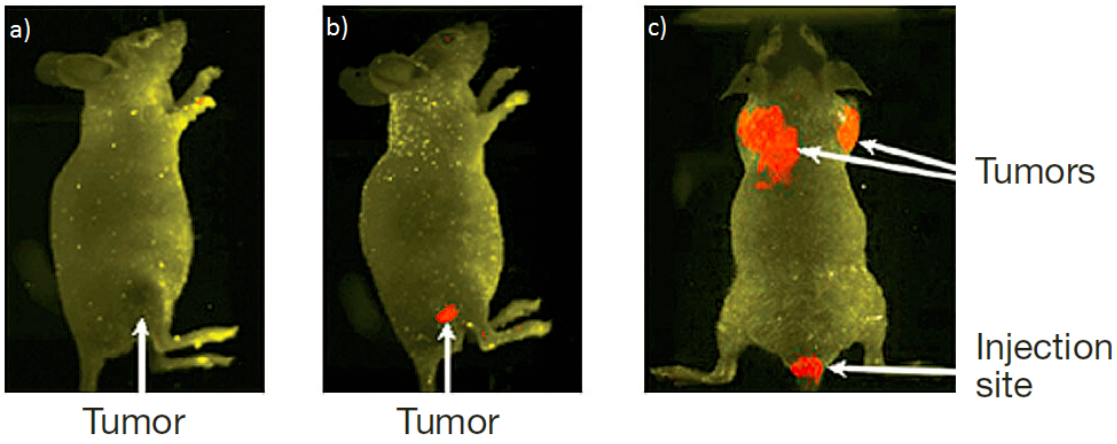

Figure 1.5: Fluorescent images of tumor carrying mice following three different targeting schemes. (a) Passive targeting of quantum dot probes with carboxylic acids groups attached to the surface, a circulation time of 6 hours. (b) Passive targeting of quantum dot probes with polyethylene glycol groups on the surface, circulation time of 24 hours. (c) Active targeting of quantum dots with PSMA antibodies, circulation time of 2 hours. Image reproduced from [9].

- Rapid thermal expansion of the nanoparticle and surrounding fluid leading to acoustic shockwaves causing physical damage to the cellular structure
- Formation and subsequent explosion of vapour bubbles from the surrounding liquid again leading to shockwaves
- Penetration of molten gold into the cellular structure
- Formation and subsequent explosion of gold vapour bubbles leading to shockwaves
- Generation of gold plasma and associated shockwave
- Explosive fragmentation of the gold nanoparticles

Figure 1.6 illustrates these mechanisms in order of their estimated activation temperatures/energies.

One way to gain insight into which of these mechanisms may be active is to gain a solid understanding of the temperatures involved in the process. For example if the temperature

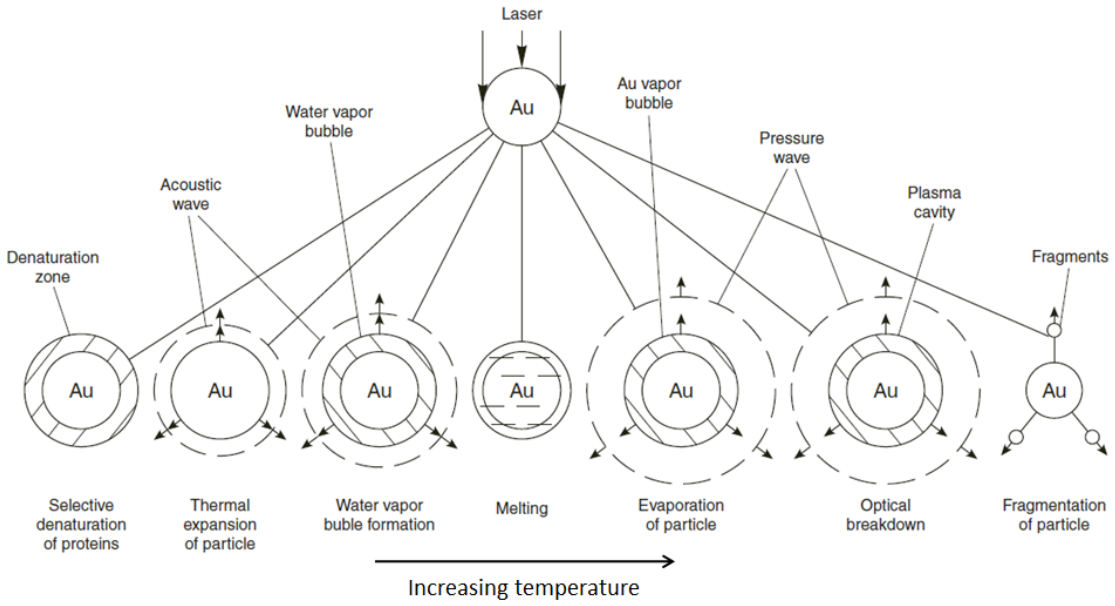

Figure 1.6: Illustrating the various damage mechanisms which could be responsible for cell death in increasing order of the temperatures required. Image reproduced from [10].

of the nanoparticle was found to have an upper bound which is lower than the melting point of gold then the last four mechanisms listed here could be ruled out. Multiple studies have been published which make estimates of the local temperatures, however their is no consistency in their estimates. We now discuss these various estimates. A distinction must be made first between the temperature of the nanoparticle and the surrounding medium. These temperatures should be drastically different as a result of both the large differences in specific heat, and the drop in energy density as heat diffuses away from the sphere ($\sim d^3$).

The first study we consider is by Huang et al. [11] who performed a finite differences solution of the heat equation.

$$\frac{\partial T}{\partial t} = \alpha \nabla^2 T + Q(r,t) \tag{1.1}$$

Where $\alpha = k/\rho c$, k is the thermal conductivity, c is the specific heat, ρ is the density, and Q is a heating source term. It should be noted that α will in general be temperature dependent but that this temperature dependence is commonly neglected. The study was interested in the temperature of the surrounding cellular medium so α was based on the

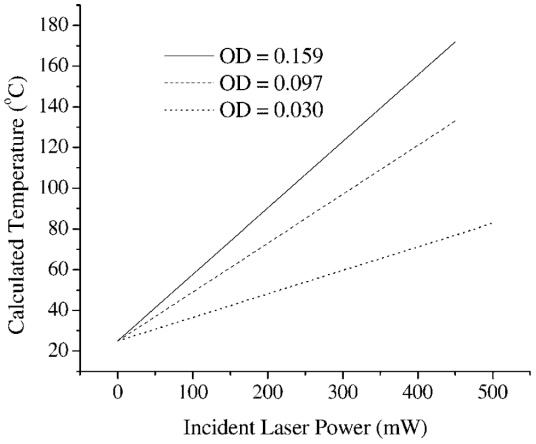

Figure 1.7: Calculated temperature in the vicinity of the nanoparticle versus the incident CW laser power. The different curves are for different optical densities of the nanoparticle/cell system. Image reproduced from [11].

cell properties and not the nanoparticle. The Q term is representative of the heating due to the nanoparticles. The calculated temperature versus the incident continuous-wave (CW) laser power is plotted in figure 1.7. We see that the estimated temperature rises are on the order of 100 K. This result suggests that denaturation of cellular proteins and shockwaves from liquid vapours are possible. It cannot address the possibility of the other proposed mechanisms which depend on the temperature of the nanoparticle. Some concerns regarding this result are that the optical density used by the researchers is the combined effect of scattering and absorption, however they have assumed that the scattering is negligible. Furthermore the study models the temperature as a result of continuous laser heating while *in vivo* PTT treatments should be carried out using a pulsed laser to localize the heating. It is also unclear here what the 'vicinity' of the nanoparticle is as the authors do not provide a distance. By heating cellular cultures in an oven at temperatures similar to those estimated by their modeling the authors seem to suggest that it is denaturation of cellular proteins which leads to cell death.

Pitsillides et al. [12] have also modeled the temperature increase in the tissue surrounding the nanoparticles, they have made use of a solution to the heat equation developed by Goldenberg and Tranter [13]. The Goldenberg and Tranter solution is for a sphere generating heat at a constant rate embedded in an infinite medium. Through this model

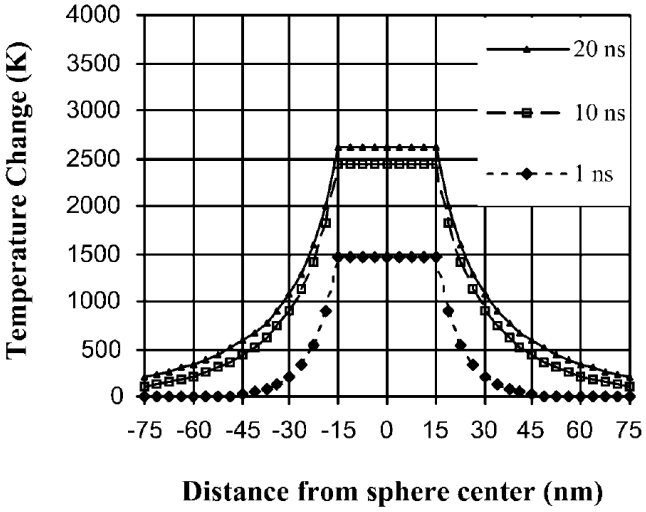

Figure 1.8: Plot of the estimated temperature change using the Goldenberg and Tranter solution to the heat equation. This figure was produced assuming an absorbance of 2, laser fluence of 0.5 J/cm^2, and a 30 nm sphere. Image reproduced from [12].

the authors estimated the temperature rise of the nanoparticle to be $\sim$ 2500 K, figure 1.8. Such a temperature would be sufficient to cause melting of the nanoparticle (T_{melt} = 1337 K) and produce gold vapours (T_{boil} = 2340 K). In figure 1.8 are the predicted temperatures profiles during a 20 ns laser pulse. Some concerning issues regarding this result are a lack of details regarding the values of the absorption coefficient, and heat capacity of the sphere. The result is also limited in that the temperature profile following a laser pulse cannot be investigated due to the assumption of a constant heating rate. The researchers point to the bubble effect as the likely cause of cell death, the idea that a rapid heating of the nanoparticle results in an explosive vapourization of a thin layer of liquid at the particle boundary which rapidly expands. The bubble effect is estimated to have an activation temperature $\sim$ 500 K [14]. The images are not provided in the paper but the authors say that electron microscopy had also revealed evidence of nanoparticle fragmentation.

The largest estimate in the literature comes from Kurita et al. [15]. Who make a simplified assumption that the observed extinction coefficient of an aqueous nanoparticle solution can be attributed entirely to the absorption of light by the nanoparticles, ignoring absorption and scattering from water and scattering from the nanoparticles. They then assume that all of this energy goes into increasing the temperature of the nanoparticles (no

diffusion to surroundings) and find a temperature rise of 30000 K, using a more modest estimate for the absorption coefficient of the nanoparticles they then report temperature rises of 10000 K. However if one attempts to reproduce these estimates, by performing simple calculations using the values of the laser fluence reported earlier in the paper a consistency is not found and an estimate of $\sim 3500K$ is found instead. Despite this the result is still referenced by some authors in the field when attempting to enforce the idea of nanoparticle fragmentation as a primary mechanism in cell destruction.

Zharov et al. [16] have considered a kernel solution to the heat equation (equation 1.1),

$$\Delta T(r,t) = \Delta T_{MAX} \left(\frac{4\alpha t + R^2}{R^2} \right)^{-3/2} exp\left(-\frac{r^2}{4\alpha t + R^2} \right) \tag{1.2}$$

where ΔT_{MAX} is an estimate of the maximum temperature achieved by the nanoparticle based on the input laser fluence and the particles properties, R is the nanoparticle radius, and $\alpha = \kappa/\rho c$ with κ, ρ, c being thermal conductivity, density, and specific heat of the surrounding medium respectively. Using an 8 ns laser pulse with energy $0.5J/cm^2$ they report an estimate of the temperature in the immediate vicinity of a nanoparticle to be $\sim$ 1500 K and suggest bubble formation as the main cause of cellular damage. Unfortunately there is a lack of information in the paper regarding the absorption coefficient used in the calculation.

Letfullin et al. [17] have performed a thorough analysis on the temperature rise of a nanoparticle due to absorption. In this paper the authors consider two models, a two temperature model which considers the temperatures of the electron gas and the gold lattice separately through a set of coupled differential equations, and a one temperature model which assumes the temperature of the electron gas and lattice to be equal. Both models incorporate a transfer of heat to the surroundings throughout the laser pulse, something which is neglected by the other approaches discussed so far. Both models are solved numerically and it is found that the two temperature model breaks down for pulse lengths exceeding the femtosecond scale. Figure 1.9 plots the temperature of a nanoparticle as solved by the one temperature model for different biological environments; fat, blood, tumor and prostate. The plot shows maximum temperature increases on the order of 400-700 K depending on the surrounding medium. This result makes it clear that even in the short 8 ns duration of the laser pulse the properties of the surrounding medium are important and cannot be neglected when modeling the process.

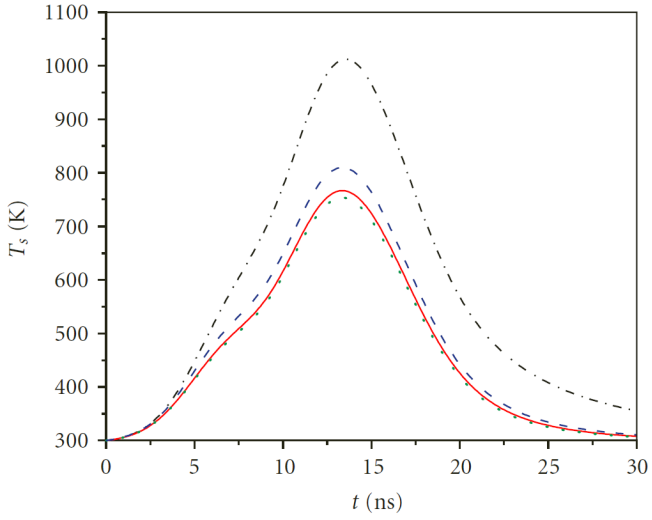

Figure 1.9: Plot of nanoparticle temperature versus time for a 8 ns pulse with energy density 10 mJ/cm^2. Different curves represent different biological environments: fat (dash-dot curve), blood (dashed curve), tumor (solid curve), and prostate (dotted curve). Image reproduced from [17]

So far we have discussed many attempts at estimating the local temperatures achieved due to the absorption of light by gold nanoparticles, all theoretical. The results of these estimates range over many orders of magnitude and unfortunately comparisons to experiment are limited. To date there are two experimental measures which are cited. O'Neal et al. [18] performed an *in vivo* study of tumor ablation in live mice. Tumors were grown subcutaneously (just below the skin) in live mice, nanoshells were injected and allowed to passively accumulate at the tumor site. During the laser treatment with NIR light the surface temperature at the tumor site was measured with a handheld IR thermometer. In this study a CW laser was used rather than a pulsed laser and after 30 seconds of treatment the surface temperature was measured to be $\sim$ 323 K, assuming an initial temperature of $\sim$ 295 K this represents an increase of $\sim$ 28 K. Although this provides no estimate of the temperatures in the immediate vicinity of the nanoparticles it is a good measure for the temperature at distances on the order of mm away form the heat source. In addition to providing this temperature measurement the study was among the first to show the viability of PTT, all of the treated mice survived while the control group was not so lucky.

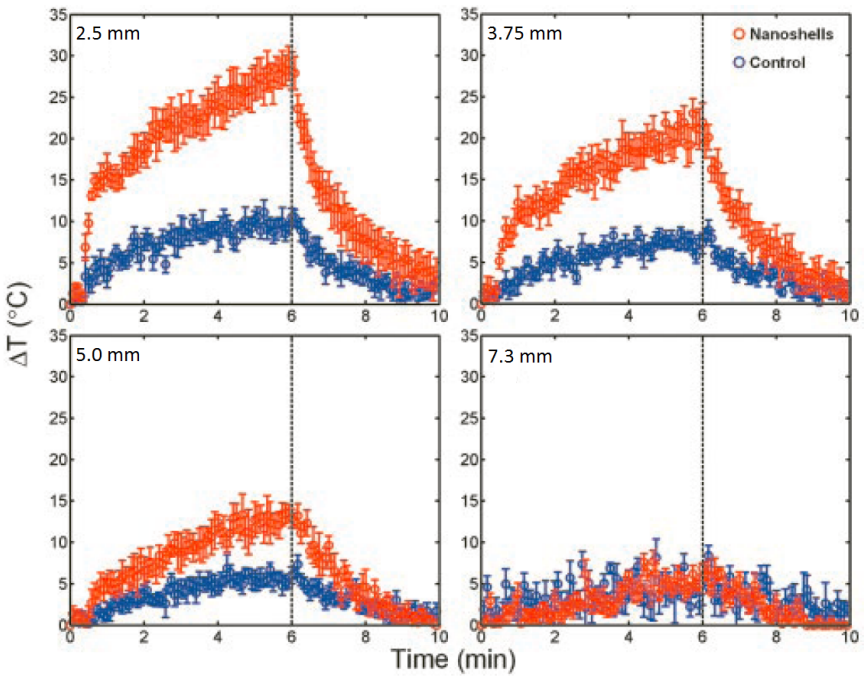

Figure 1.10: Temperature increase versus time for several positions from the tumor surface (as indicated in the upper left), the lower curves in blue represent a control experiment with no nanoshells present. Image adapted from [19].

Hirsch et al. [19] performed a tumor ablation study using nanoshells on live mice as well as under *in vitro* conditions. During and following the NIR treatment in live mice, the temperature in the surroundings was measured using MRI with a spatial and temporal resolution of 0.16 mm and 5 sec. respectively. The tumor site was illuminated with a CW laser with power density of 4 W/cm^2 for 6 minutes. Figure 1.10 plots the temperature increase as a function of time at various depths within the tumor. The maximum temperature rise was found to be $\sim$ 30 K, similar to the result of O'Neal et al.. In the upper left plot it is clear to see that there are three processes; a rapid ($\sim$ 1 min) initial heating, followed by a slower heating up to 6 minutes where the laser is shut off, and a cooling as heat diffuses away from the tumor.

1.5 Summary

Although being a well developed technique with a proven viability as a cancer therapy, there are some fundamental outstanding issues regarding both the damage mechanism and the local temperatures achieved in the process. The experimental measures of Hirsch et al. and O'Neal et al. suffered from limited temporal and spatial resolution, while the theoretical estimates vary substantially between studies. Theoretical studies and physical intuition suggest that temperatures in the vicinity of the nanoparticles will decay rapidly. Thus there is a need for an experimental measure of the local temperatures with an improved sensitivity to the short time scale response, specifically following a pulsed heating event. An experiment with this aim in mind is described in the following chapters.

Chapter 2

Experimental Details

This chapter contains the experimental details regarding a study we have designed to probe the temperatures achieved in the vicinity of gold nanoparticles acting as localized heat sources due to the strong absorption of incoming light. The basic strategy is to use a system of inverted micelles containing a fluorescent dye solution on their interior. Using a dye which has a temperature dependent intensity we can measure the temperature rise on the interior of the cell by tracking the changes in fluorescence intensity. The chapter is broken down into two sections, sample preparation and experimental method.

2.1 Sample Preparation

In this study we apply a model system in place of biological cells in order to have better control over the environment and improve the reproducibility of the results. The system we use is that of an inverted micelle solution with an aqueous phase on the interior and an organic solvent (toluene) on the exterior. Glogowski et al. [20] published a study on the production of such systems. Using the previously reported method of Brust et al. [21] they created solutions of gold nanoparticles ($\sim$ 2.5 nm) which had a thiol surface coating of n-dodecanethiol ($CH_3(CH_2)_{10}CH_2SH$). This surface coverage proved to be unable to stabilize the water-oil interface, and the nanoparticles remained dispersed in solution. The researchers then substituted the thiol for a ligand 11-mercapto-1-undecanol ($OH(CH_2)_{11}SH$) which was also unsuccessful with the nanoparticles precipitating out of the

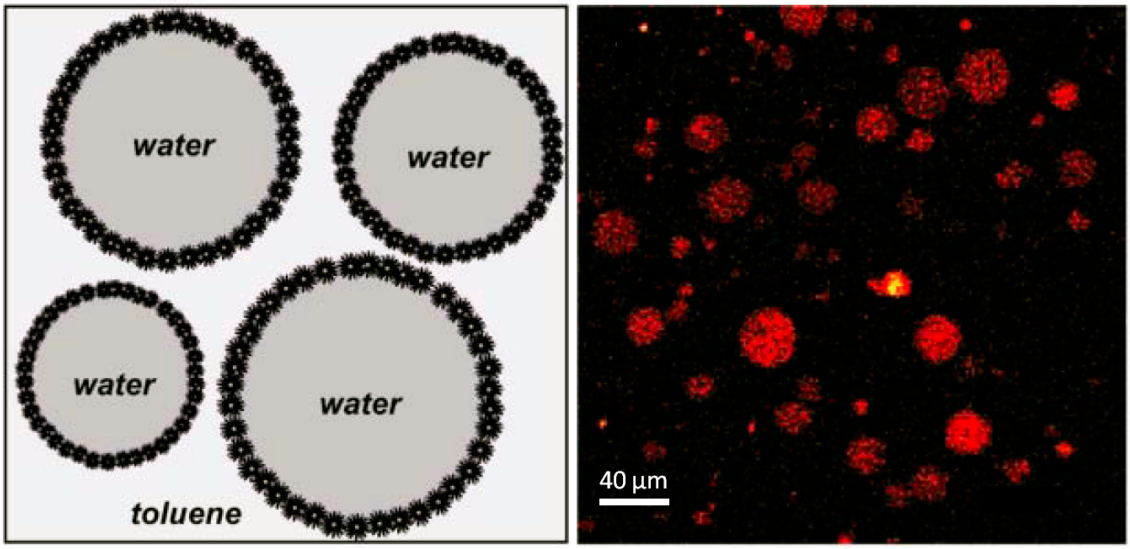

Figure 2.1: Left: A schematic illustration of the inverted micelle system. Right: Fluorescence confocal microscopy image of stabilized inverted micelles, the fluorescent dye sulforhodamine B appears red. Image adapted from [20].

solution. Given these behaviours they then partially substituted the n-dodecanethiol with 11-mercapto-1-undecanol to produce a mixed surface coverage and by tuning the ratios of the two components managed to find a coverage which stabilized the oil-water interface. It was then verified that the aqueous phase was on the interior by repeating the process with a water soluble fluorescent dye, sulforhodamine B, present. Fluorescence confocal microscopy was then used to image the micelles, figure 2.1. In our experiments we have engaged in a collaboration with the research group led by Todd Emrick from the Polymer Science and Engineering Department at the University of Massachusetts who were responsible for this study. They have kindly provided us with a toluene based solution of nanoparticles with this mixed surface coverage of n-dodecanethiol and 11-mercapto-1-undecanol.

In order to form the inverted micelle system we simply take the toluene based solution, add it to a water/fluorescent dye solution, and shake. The procedure is as follows:

1. We use the fluorescent dye Rhodamine 6G (R6G, M = 479.02 g/mol) which comes as a dry powder. A 2 mM aqueous solution is prepared in ~ 40 μL of distilled deionized water using a microbalance with 0.1 mg precision.

2. This solution is then mixed with the gold nanoparticle/toluene solution and extra HPLC grade toluene at a ratio of 45:200:250 parts water/dye solution, nanoparticle/toluene solution, and toluene respectively.

3. This solution is then shaken vigorously by hand and transferred into a thin glass vial.

The fluorescent dye used in this study was selected based upon several considerations:

- Strong absorption at available laser wavelengths 488 nm or 532 nm
- Emission at wavelengths greater than 532 nm, in our experimental setup we use an optical filter to block all light at wavelengths below 532 nm from reaching the detector so this is required to avoid losing the fluorescence signal.
- A temperature dependent fluorescence intensity. This is crucial to the experiment because the changes in fluorescence intensity are to be used to infer changes in temperature
- Water soluble
- Good photostability, dye does not photobleach throughout the experiment

Rhodamine 6G was found to be a good candidate based on these criterion. Figure 2.2 plots the normalized extinction coefficient and fluorescence intensity for R6G versus wavelength. From this figure we see that R6G satisfies our first two requirements. Figure 2.3 plots the R6G emission spectra at several sample temperatures, the changes in intensity are clearly visible.

2.2 The Experimental Method

The concept of the experiment is quite simple, the solution of inverted micelles containing an aqueous dye solution on the interior is loaded into a sample holder and a laser is focused onto the solution. The absorption coefficient of the nanoparticles has a peak $\sim$ 532 nm which is approximately the same as the absorption peak of R6G. This means that a single laser can be used for both heating and excitation of the dye, we use a 532 nm

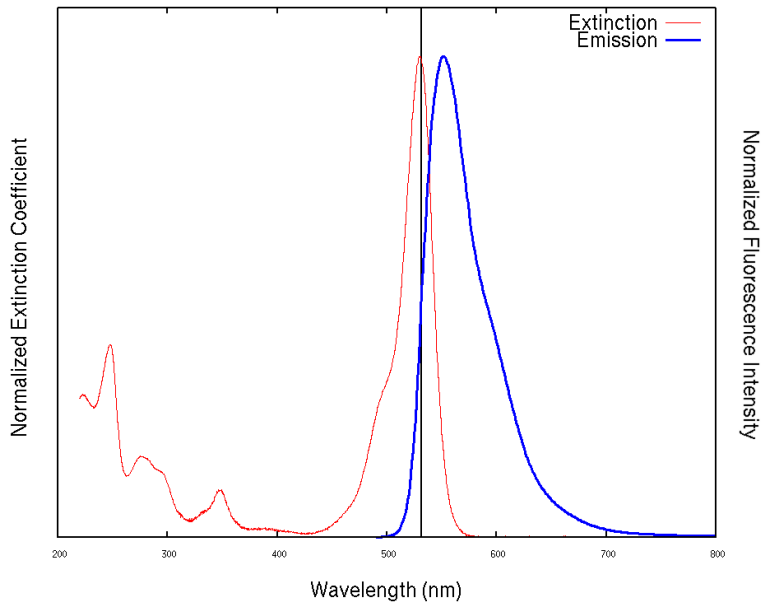

Figure 2.2: Normalized extinction coefficient and fluorescence intensity of R6G. The vertical line is placed at $\lambda = 532$ nm. Image based on data from Du et al. [22].

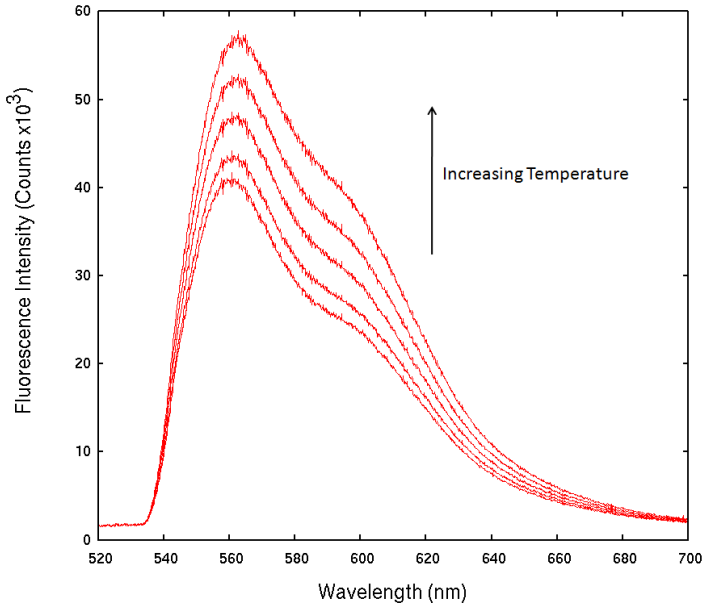

Figure 2.3: R6G emission spectra taken at different sample temperatures from 313 K to 353 K.

CW laser (Coherent V-2, 2 Watts) for this. The advantage of this is that the excitation of the dye molecules is guaranteed to occur in the same volume as the heating. However the disadvantage of this is that the strengths of the two processes become coupled; one cannot increase the amount of heating without increasing the degree of excitation. This could pose an issue if one wants to study high heating rates because the dye may begin to photobleach at the higher intensities. In our lab we have two available laser sources, a 488 nm CW laser (Melles Griot) and the 532 nm CW laser, we have also had access to a 527 nm Q-switched pulsed laser. In earlier stages of this study we had considered an alternate choice of dye, specifically Cy2 which has an excitation peak close to 488 nm. We could have separated the excitation and heating intensities with this dye, however the emission peak of Cy2 is slightly below the 532 nm wavelength that the low wavelength filter blocks from our detector, significantly reducing our usable fluorescence signal. This 532 nm short wavelength filter is used in order to block scattered laser light from overwhelming the detector. This could be partially remedied by using a 532 nm notch filter which only blocks a small window of wavelengths around 532 nm.

After illumination, the fluorescent signal needs to be collected and focused onto the detector. We use a large ($\sim$ 10 cm diameter) lens placed close to the sample in order to collect light over a large subtended angle. This collected light is then directed through a small tube which contains the short wavelength filter before being focused onto the detector. A mirror is placed between the laser aperture and sample, this mirror and the lens are mounted on translation stages so that the laser can be steered onto the sample and the collected light can be focused onto the detector. Two detectors have been used, an avalanche photodiode (APD) (Perkin Elmer) and a spectrometer (Ocean Optics USB2000). The APD has an improved sensitivity to low signals and faster response time than the spectrometer, but it comes at a loss of spectral information. When using the spectrometer it can be directly connected to computer through the supplied USB cable and parameters such as integration time and averaging can be controlled through the Ocean Optics OOIBase32 software. The APD has a single BNC output which carries a voltage representative of the frequency at which photons are striking the detector. This signal is read by an oscilloscope (Teknix) which connects through USB-GPIB to the computer. A LabVIEW program permits computer control over the oscilloscope settings and presents the results on the computer screen. The APD setup is advantageous when a pulsed laser is used for heating because the oscilloscope can be set to trigger on a pulse event (or just before) and the

fluorescence intensity immediately following the pulse can be observed.

Chapter 3

Results

We now discuss the preliminary findings of this experiment. The project remains unfinished, success was had using the 532 nm CW laser and an increase in fluorescence intensity was observed upon illumination. However the experiment really needs to be carried out while using a pulsed laser which would restrict the heating to smaller volumes and better replicate the conditions of PTT. We present the preliminary findings here which at the very least offer a proof of concept.

3.1 Temperature Calibration

In order to relate changes in the fluorescence intensity to changes in the temperature of the aqueous phase a calibration is required to determine the scaling of the intensity with temperature. This is done using an aqueous solution containing only the fluorescent dye in distilled deionized water. The solution is loaded into one of the glass vials used for the real experiment and a thin thermocouple is placed into the solution. This vial is submersed into a small beaker of water which is placed onto a hotplate and slowly heated while monitoring the solution temperature with a thermocouple. The large thermal mass of the beaker of water helps to ensure that the heating is uniform in the vial. The solution can then be excited with the 532 nm CW laser and due to the absence of nanoparticles the heating due to the laser is negligible, as confirmed by the stability of the intensity without external heating. The spectrometer can then be used to collect a spectrum at regular intervals and

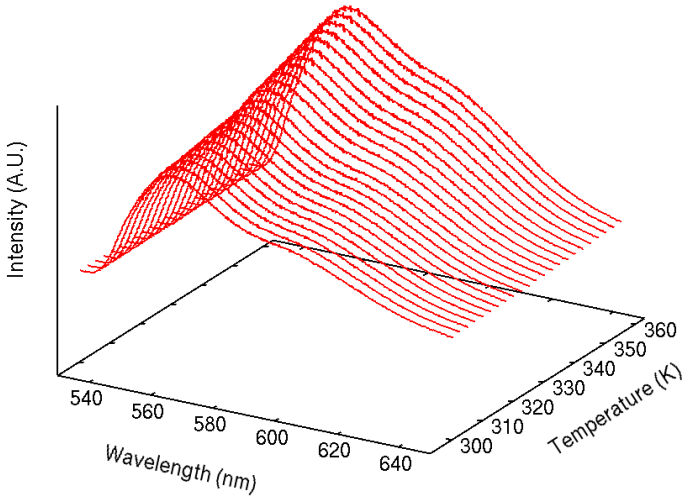

Figure 3.1: Fluorescence spectra taken at different times during the cooling of an aqueous R6G solution.

the spectrum number at specific temperatures as read by the thermocouple is noted. Data is collected upon cooling from $\sim$ 360 K.

Figure 3.1 shows a 3-dimensional plot of the fluorescence spectra at different temperatures. From this data we extract out the peak intensity to characterize the spectrum, and look at the normalized peak intensity as a function of temperature, figure 3.2. From this plot we see that the temperature dependence of the normalized peak intensity can be reasonably well described by a linear relation.

3.2 Proof of Concept

Taking the solution of inverted micelles with aqueous R6G solution we observe the fluorescence spectrum as a function of the time spent in the laser focus at a power of 0.15 Watts; this produces figure 3.3. We can then extract the peak intensity, normalize it to the t = 0 intensity, and use the previously determined relationship to calculate the change in temperature. Figure 3.4 plots this data, since the relative increase in intensity is linearly proportional to the temperature rise we can represent both quantities by one data set, normalized peak intensities are on the left and the corresponding temperature rise is given

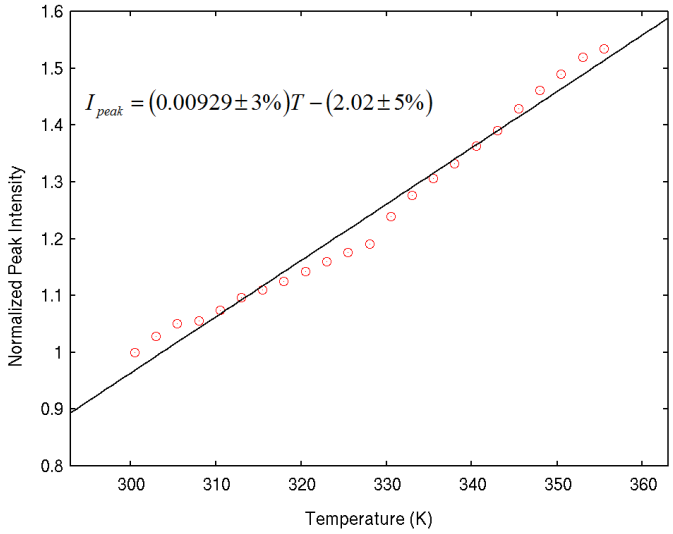

Figure 3.2: Plotting the peak fluorescence intensity normalized to T = 301 K versus temperature to establish as relationship between the two. A linear fit is provided.

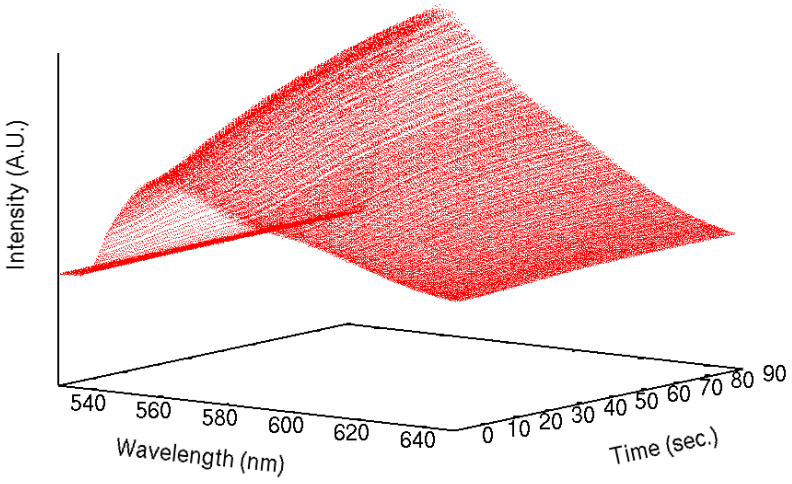

Figure 3.3: Fluorescence spectra taken at increasing laser exposure times. Increases in fluorescence intensity are a direct result of heating from nanoparticles absorbing the incoming radiation.

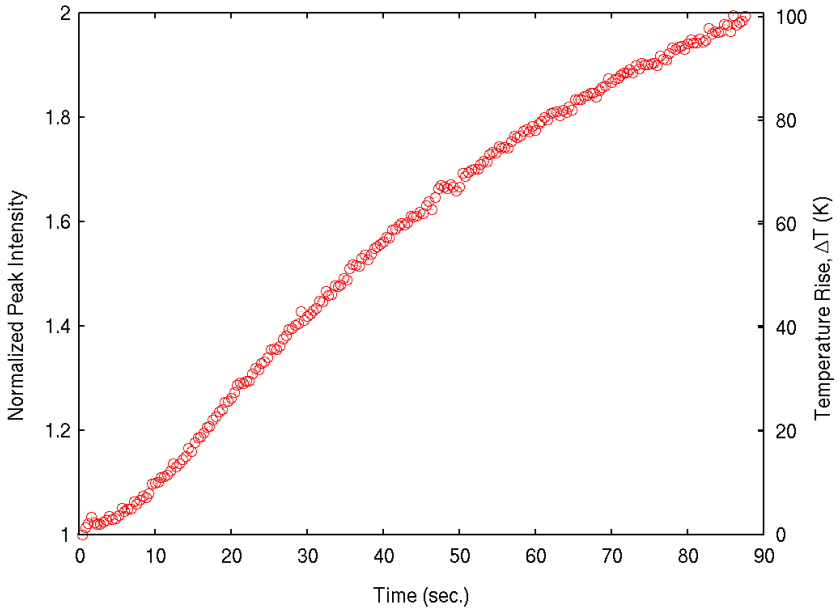

Figure 3.4: Normalized peak intensity (left axis) and corresponding temperature rise (right axis) versus laser exposure time.

on the right. The measured temperature rise was found to be approximately 100 K over the 90 second experiment. This is an encouraging result as it shows that the experimental approach is working. The next logical step in this experiment is to move to a pulsed laser setup. Not having a suitable laser in our lab we began a collaboration with Dr. Joe Sanderson in the Physics department at the University of Waterloo and tried the experiment on his high powered Ti:sapphire pulsed laser system. Unfortunately there were some logistical problems in conducting the experiments, mainly a lack of available laser time, insufficient space for a proper layout, and some communication barriers, which hampered progress. In trying to setup the experiment on the pulsed system we were having issues with collecting enough fluorescence signal without also detecting the scattered laser light; either the scattered light was seeping into the detector or there was such a strong scattered signal that an appreciable amount of light was transmitting through the filter. There were also some issues regarding timing, it is crucial that triggering is properly established such that as the oscilloscope averages over many pulse events subsequent pulses are always aligned. These were not major problems that alone would have terminated the project, they are just the issues that were being worked out when the project was stopped. While working through

these problems it was decided that efforts would be better spent on a different project and the experiment was left unfinished. Although we were not able to directly address any of the issues discussed in chapter 1 for pulsed laser heating, we have at least demonstrated the viability of this novel experimental design and measured the temperature rise during CW laser heating.

Part II

GOLD NANOPARTICLE EMBEDDING STUDY

Chapter 4

Introduction

This part of the thesis is aimed at explaining experimental studies performed on the molecular glass forming system tris-naphthylbenzene (TNB). The current chapter represents an introduction to the field of glass transition physics and is split into three sections:(i) an introduction to polymer physics which facilitates a discussion of the immense body of research studying glassy polymer films, (ii) an introduction to the glass transition and the associated theoretical models, (iii) and a literature review on the subject of glassy systems in confinement.

The subsequent chapters discuss the experimental details (5) and findings (6) of the experiments which are the focus of this part of the thesis: gold nanoparticle embedding studies on the surface dynamics of TNB.

4.1 Polymeric Systems

4.1.1 Basic Concepts

Polymers are macromolecules, a series of *monomers* covalently bonded together into long chains. Figure 4.1 illustrates the process of polymerization for a particular polymer species, polystyrene (PS). Polystyrene is just one type of polymer species and many different species exist, due to the differences in chemical structure different species will often behave very differently, figure 4.2 shows the structures of a few common polymer species. The degree of

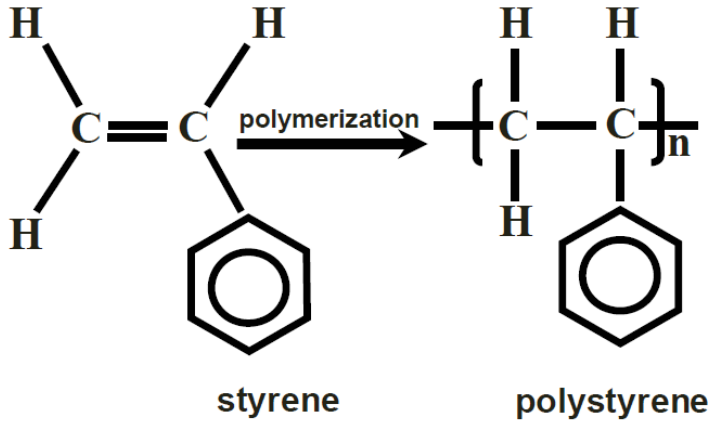

Figure 4.1: Upon polymerization the double bond between carbon atoms is broken and each carbon atom will bond to another styrene monomer. The end result is a long chain of styrene monomers linked together by a Carbon backbone. Figure adapted from [23].

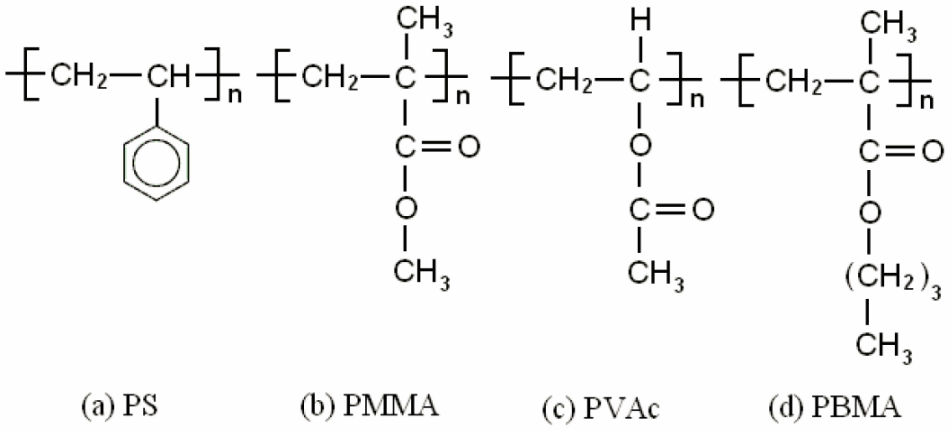

Figure 4.2: The chemical structures of some common polymer species, n indicates the degree of polymerization or the length of the chains. Notice the different species are all a result of different sidegroups attached to the carbon backbone. Image reproduced from [24].

polymerization, indicated in these images by n, is the number of monomers that are connected together to form the polymer. In a polymer system there will be some distribution of polymer lengths, i.e. not all chains will have the exact same number of monomers. There are two quantities that are commonly used to discuss the average size of the polymers in a sample, the *number average molecular weight*:

$$M_N = \int \rho(M) M dM \tag{4.1}$$

and the *weight average molecular weight*:

$$M_W = \frac{\int \rho(M) M \cdot M dM}{\int \rho(M) M dM} \tag{4.2}$$

In these expressions M is the molecular weight of a chain which is equal to the molecular weight of the monomer times the degree of polymerization, and ρ(M) is the normalized distribution function of chains with weight M, notice ρ(M)dM gives the fraction of chains with molecular weights between M and M + dM. Taking the ratio of these two quantities yields the *polydispersity index*:

$$P.I. = \frac{M_W}{M_N} \quad , \tag{4.3}$$

which is an indicator of the width of the distribution of chain sizes in the system. For a system with a uniform distribution of chain lengths, ie. all chains are of equal length, this quantity is equal to 1, otherwise this is greater than one and indicates the polydispersity of the sample.

There are a number of different structures that a polymer chain can be formed into based on the chain architecture. In the discussion above we talked about polymers as linear chains of monomers, however this is just one possible chain architecture. Figure 4.3 illustrates three possible structures, linear, branched, and star however many more exist. Additional variants can be formed by changing the *tacticity* of the polymer, this refers to the orientation of the polymers sidegroup. Consider for example polystyrene where the sidegroup is a benzene ring, this benzene ring can be ordered on the same side of the chain for all monomers (isotactic), alternating sides of the chain (syndiotactic), or randomly oriented (atactic). A simplified illustration of this concept it shown in figure 4.4.

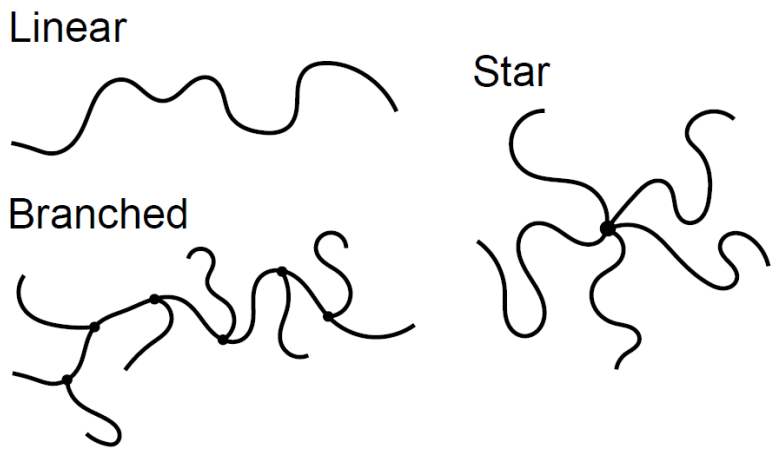

Figure 4.3: Illustrating three common polymer architectures, linear branched, and star.

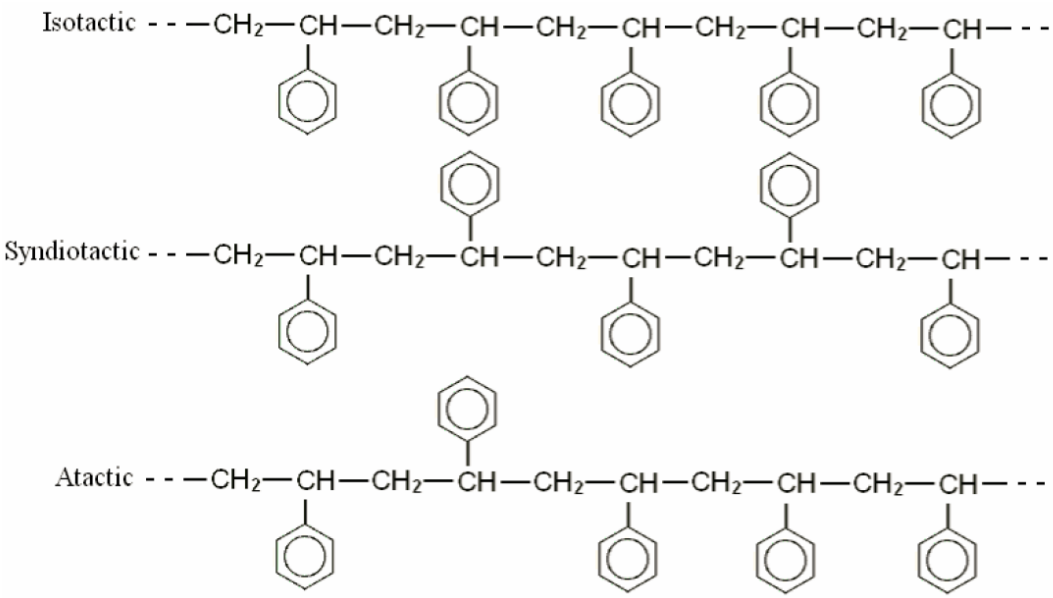

Figure 4.4: In an isotactic chain the side-groups are always ordered on the same side of the chain, in syndiotactic chains the orientation alternates with each monomer, in atactic chains the orientation is random. Image reproduced from [24].

4.1.2 Static Polymer Conformations

In discussing polymer conformations physicists often adopt a freely-jointed chain (FJC) model. The assumptions of this model are that the polymer chain can be viewed as a series of linear segments, each with length b, which are randomly oriented. Being randomly oriented means that the orientation of one segment b_i is independent of the neighbouring segments $b_{i\pm1}$. In this model the polymer is simply a random walk and it is easily shown that,

$$\langle R_{EE} \rangle = 0 \tag{4.4}$$

$$\left\langle R_{EE}^2 \right\rangle = b^2 N \tag{4.5}$$

where R_{EE} is the end-to-end vector connecting the two end-points of the chain, and N is the number of segments of length b that the chain is comprised of. A related quantity that is often used to characterize chains is the radius of gyration,

$$\left\langle R_g^2 \right\rangle = \frac{1}{N} \sum_{i=1}^{N} (R_i - R_{CM})^2 \tag{4.6}$$

where,

$$R_{CM} = \frac{1}{N} \sum_{i=1}^{N} R_i \tag{4.7}$$

is the polymer's center of mass. A straightforward analysis shows for a linear polymer,

$$\left\langle R_g^2 \right\rangle = \frac{\langle R_{EE}^2 \rangle}{6} \tag{4.8}$$

So we have our chain described as a series of N independent segments of length b, but we haven't discussed what this segment corresponds to physically. A first guess may be to use the monomer size as the length and the number of monomers as the number of segments. However neighbouring monomers are not actually independent, there is a set bond angle between monomers, there is a freedom though in the choice of the torsion angle ϕ which leads to the flexibility in the chain[1]. Figure 4.5 illustrates this concept. A better choice for the segmental unit is determined by the persistence length of the polymer. The persistence

[1]There are preferred values of ϕ corresponding to trans and gauche states but often thermal energies are strong enough to overcome these restrictions, the hindered rotation and rotational isomeric state models take this into account.

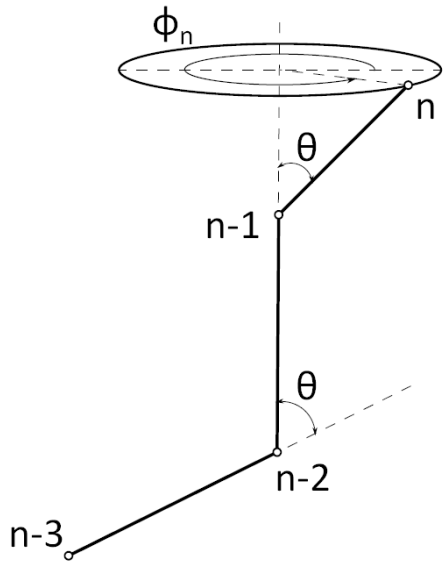

Figure 4.5: A section of a polymer chain at the monomer level. Each bond is at a constant angle θ which depends on the polymer species. The torsion angle ϕ is free to rotate which leads to the polymers flexibility.

length is essentially the distance along the chain over which correlations between monomers decay. On length scales shorter than this persistence length the polymer appears stiff, but on larger length scales the polymer will appear flexible.

It turns out that in suitable environments this model does a good job of describing chain statistics. These environments are polymer melts, and dilute solutions at the theta point. In this model we have neglected to consider:

- Solvent effects, interactions with solvent molecules
- Steric effects, excluded volume effects which prevent chain overlap
- Interactions with other chains

In a polymer solution the interactions between the polymer and solvent molecules are important. Depending on the polymer-solvent interaction (which is dependent on temperature) the solvent can classified as:

- **Good Solvent**: In a good solvent there is a favourable interaction between polymer and solvent molecules and and the polymer will adopt a swelled (relative to the result of the FJC) conformation.
- **Poor Solvent**: Contrasting a good solvent is the poor solvent where the unfavourable interaction tends to exclude solvent from the polymer chain and the chain collapses onto itself.
- **Theta Solvent**: A theta solvent is defined as a solvent where the polymer-solvent interactions are balanced such that the polymer conformation matches the predictions of the FJC model. Since the polymer-solvent interaction is temperature dependent any solvent can be made a theta solvent by taking the system to the theta temperature.

As mentioned, the ideal results of the FJC model can also be applied to a polymer melt system. In a polymer melt all space is occupied by polymers and the density is constant. This is a rather surprising result then that the interactions between polymers, neglected in th FJC model, appear to play no role in the polymer conformations. The simple explanation for this is that the interactions cancel out; a polymer in the melt interacts with itself

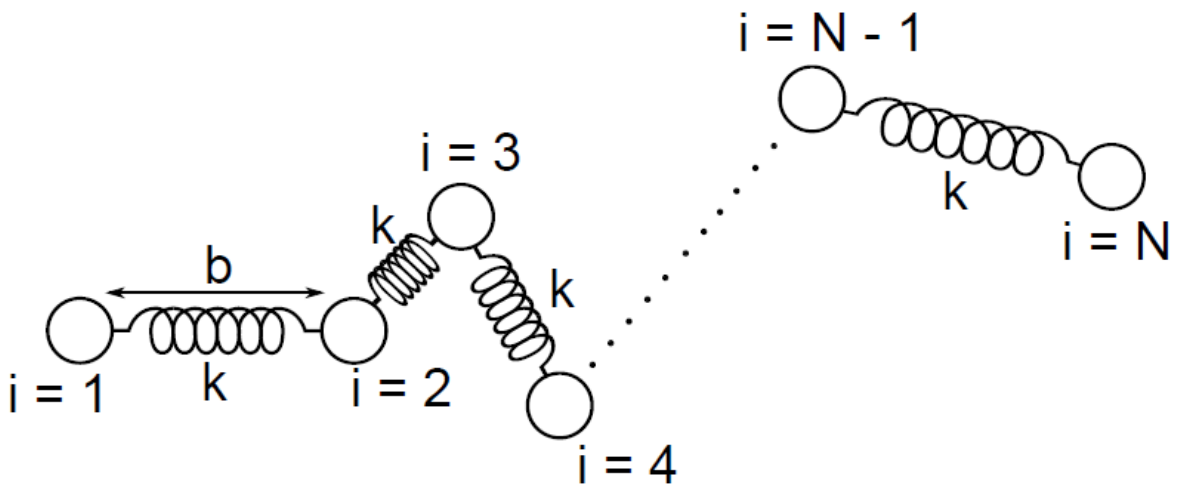

Figure 4.6: The Rouse model considers a chain of N massless beads, connected by massless springs of uniform spring constant k.

leading to an outwards force trying to swell the coil, and with other polymers leading to an inwards force acting to compress the polymer. These forces balance one another and ideal chain statistics are valid in the polymer melt.

4.1.3 Polymer Dynamics

For our purposes a full discussion on the theory of polymer dynamics is not required, here we review some important results and refer the reader to a number of excellent texts on the subject [25, 26, 27, 28]. We first consider the Rouse model. In the Rouse model we consider a chain as depicted in figure 4.6, a series of N massless beads, connected by N-1 massless springs each with spring constant k, the spring length is allowed to change but has a mean length of b. The Rouse model makes two main assumptions, i) that there are no excluded volume effects (ie. chains can pass through one another) and ii) there are no hydrodynamic interactions (solvent does not move with beads, no solvent mediated long-range interactions). The model begins by estimating the force acting on an individual bead as a viscous drag force,

$$\vec{f} = \zeta \vec{u} \tag{4.9}$$

where ζ is the viscous drag coefficient, and $\vec{u}$ is the beads velocity. This leads to a differential equation of motion known as the Rouse Equation,

$$\frac{\partial \vec{r}(s,t)}{\partial t} = \frac{3k_bT}{\zeta b^2}\frac{\partial^2 \vec{r}(s,t)}{\partial s^2} \tag{4.10}$$

here we have gone to the continuum limit and $\vec{r}(s,t)$ is the position vector of a segment at position s along the chain. Being a linear equation we can search for solutions in terms of eigenmodes,

$$\vec{r_p}(s,t) = \vec{X}_p \cos\left(\frac{p\pi s}{N}\right) e^{-t/\tau_p} \tag{4.11}$$

where $p = 0, 1, 2, ...N$ is the mode index, $\vec{X}_p$ is the mode amplitude, and τ_p is the relaxation time associated with the p^{th} mode. Upon substitution of this solution into equation 4.10 the relaxation times are found for $p > 0$ as

$$\tau_p = \frac{\zeta N^2 b^2}{3\pi^2 k_b T p^2} \tag{4.12}$$

At first glance we notice that there is a longest relaxation time corresponding to $p = 1$ which scales as N^2. Considering the form of the eigenmodes we see that this longest relaxation time corresponds to a coherent relaxation along the whole chain. We then see that a mode with index p corresponds to the coherent motion of a section of the chain with N/p segments and the relaxation time for these higher index modes scales as τ_1/p^2. Underlying the Rouse model is the assumption that the total viscous force acting on a chain is the sum of the viscous forces acting on all beads. We can use this to estimate the scaling of the diffusion coefficient of the whole chain (ie. center of mass motion) via the Einstein relation

$$D = \frac{k_bT}{\zeta_{chain}} = \frac{k_bT}{N\zeta_{bead}} \propto \frac{1}{N} \tag{4.13}$$

The Rouse model can also be used to estimate the intrinsic viscosity of a polymer solution. We can use a simple scaling argument; viscosity has the units of $energy \cdot time/volume$, the energy in a given volume V should scale as $k_bT \cdot c_{poly}$, and the relevant timescale is the $p = 1$ Rouse mode relaxation time, then we have,

$$\eta \propto \frac{k_bTc_{seg}}{N} \cdot \tau_1 \propto N \tag{4.14}$$

where c_{poly} and c_{seg} and the polymer and segment concentrations, $c_{seg} = N \cdot c_{poly}$. We can compare these predictions to experiments on polymer solutions; figures 4.7 and 4.8 show

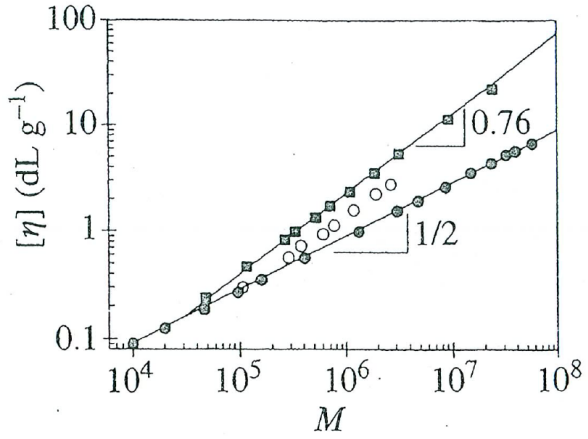

Figure 4.7: A plot of intrinsic viscosity versus molecular weight for polystyrene in 3 solvents, cyclohexane (filled circles), methyl ethyl ketone (open circles), and toluene (filled squares). The Rouse prediction of $\eta \propto M$ is not found in any of these systems. Image reproduced from [26].

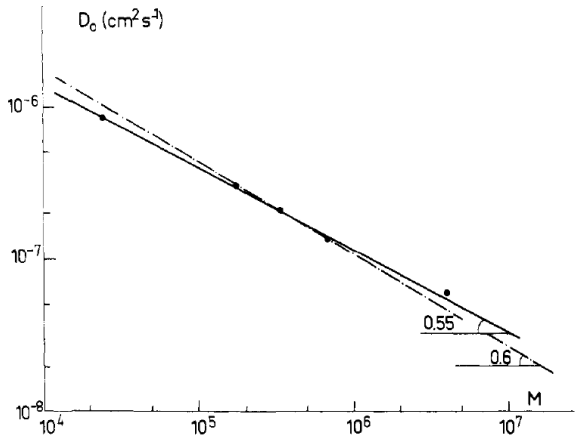

Figure 4.8: Plot of diffusion coefficient versus molecular weight for polystyrene-benzene solutions. The data finds $D \propto M^{-0.55}$ compared to the Rouse prediction of $D \propto M^{-1}$. Image reproduced from [29].

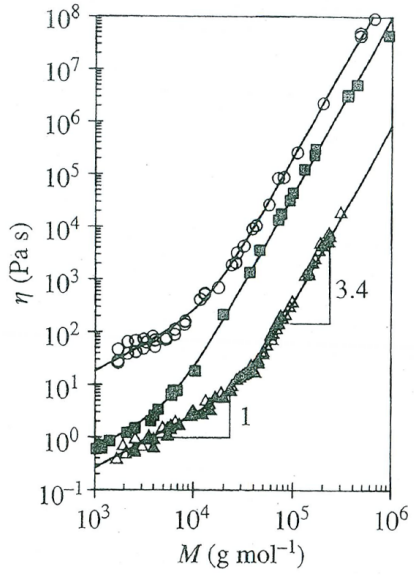

Figure 4.9: Plot of viscosity versus molecular weight for three polymer melts, polyisobutylene (open circles), polybutadiene (filled squares), polystyrene (triangles). At low molecular weights the scaling is accurately predicted by the Rouse model $\eta \propto M$, for higher molecular weights this scaling breaks down and $\eta \propto M^{3.4}$. Image reproduced from [26].

experimental results for the viscosity and diffusion coefficient of dilute polymer solutions as a function of molecular weight. The Rouse model has no success in predicting these results, a consequence of neglecting the hydrodynamic interactions. However the Rouse model is still useful in describing the behaviour of low molecular weight polymer melts. Figure 4.9 plots the polymer melt viscosity as a function of molecular weight for three polymer systems. For all data sets there are clearly two regimes; a low molecular weight regime where the predictions of the Rouse model are accurate ($\eta \propto M$), and a high molecular weight regime where this scaling breaks down and $\eta \propto M^{3.4}$. The cross-over between these two regimes occurs at the *entanglement molecular weight* (M_e), below this molecular weight the chains in the melt are unentangled and the Rouse predictions hold, above M_e the chains become entangled with one another and the Rouse predictions break down. We can however make predictions in the entangled regime by considering a new model, the de Gennes reptation model.

Next we consider the reptation model proposed by de Gennes. In a polymer melt of long

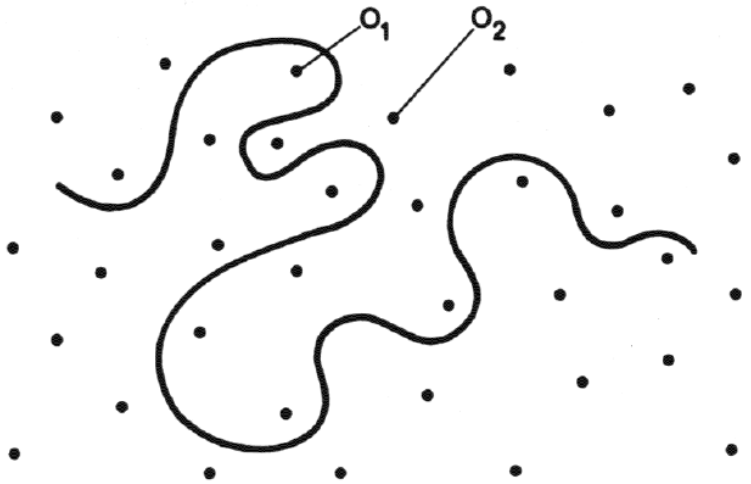

Figure 4.10: The polymer network in the melt creates a series of obstacles O_1, O_2 etc. that the chain cannot pass through. On small scales the chain can fluctuate within the tube, but large scale motions are restricted to reptation along the tube contour. Image reproduced from [28].

chains the dynamics of single chains become heavily affected by the constraints imposed by surrounding chains. Excluded volume effects in the melt restrict chains from passing through one another which naturally leads to the existence of entanglements in these systems; the Rouse model ignored excluded volume effects so it is no surprise that the model breaks down for high molecular weight melts. To study the motion of an individual chain de Gennes suggested that the constraints imposed by surrounding chains leads to the formation of an effective tube surrounding the chain. Motion of the chain on length scales comparable to the coil size are restricted to diffusion along the tube, *reptation*. Figure 4.10 shows a 2D example where the obstacles created by surrounding chains, shown as black circles, impose constraints on the motion of the chain. Figure 4.11 illustrates the destruction and creation of tube segments as the chain reptates along the contour of the tube. With the basic picture in mind we can now consider some of the predictions of the reptation model. We first consider the *terminal time* τ_t which is defined as the time required for a complete relaxation of the original tube via reptative motion. We can define a *tube diffusion coefficient* D_{tube} via the Einstein relation and a *tube friction coefficient*

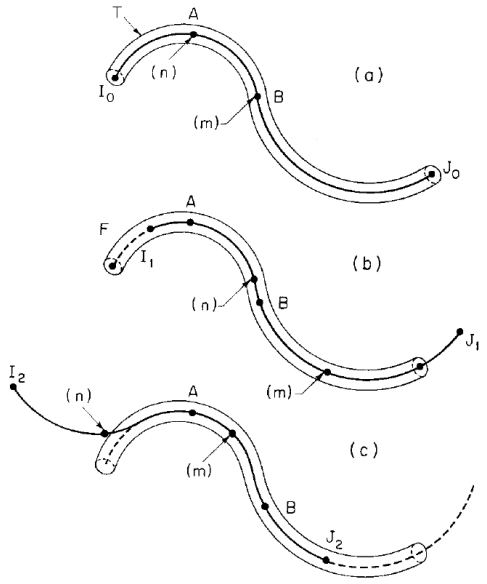

Figure 4.11: A chain constrained in it's original tube reptates to the right, as it does so a segment I_1F of the tube on the left side is evacuated. When the chain reptates back towards the left another segment J_0J_2 is evacuated on the right and the chain chooses a new path I_1I_2. Image reproduced from [30].

ζ_{tube} which should scale with N

$$D_{tube} = \frac{k_b T}{\zeta_{tube}} = \frac{k_b T}{N\zeta_o} \propto \frac{1}{N} \tag{4.15}$$

Then we can estimate the scaling of the terminal time by considering diffusive motion over a distance L, the length of the tube, which is proportional to N

$$\tau_t \propto \frac{L^2}{D_{tube}} \propto \frac{N^2}{1/N} \propto N^3 \tag{4.16}$$

Note also that the viscosity should scale with this longest relaxation time so we also have $\eta \propto N^3$. We can estimate the scaling of the *self diffusion coefficient*, D_{self}. The self diffusion coefficient represents the overall diffusive motion of the chain, whereas the tube diffusion coefficient is only concerned with motions along the contour of the tube. In the terminal time the chain has moved a distance L along the tube, however the chain has not actually diffused a distance L because the tubes are not straight. We can estimate the total distance traveled by assuming ideal chain statistics, $\langle (R(\tau_t) - R(0))^2 \rangle \propto N$ and we find for the scaling of D_{self}

$$D_{self} \propto \frac{\langle (R(\tau_t) - R(0))^2 \rangle}{\tau_t} \propto \frac{N}{N^3} \propto \frac{1}{N^2} \tag{4.17}$$

We have already seen in figure 4.9 the behaviour of the viscosity as a function of molecular weight; in the high molecular weight entangled regime experiments find $\eta \propto N^{3.4}$ which is in reasonably good agreement with the prediction of the reptation model. Figure 4.12 shows that the scaling of the diffusion coefficient as determined by experiments is $D \propto M^{-2.28}$, again in reasonably good agreement with the predictions of the reptation model. The shortcomings of the reptation model arise due to additional relaxation processes which have been neglected: constraint release whereby the finite lifetime of constraining obstacles is considered and contour length fluctuations which allow tube ends to be relaxed by contracting the chain.

4.1.4 Viscoelasticity in Polymers

Viscoelasticity in a material is defined as a response to applied stress which combines elastic and viscous behaviours. In a perfect elastic material the response to an applied stress is an

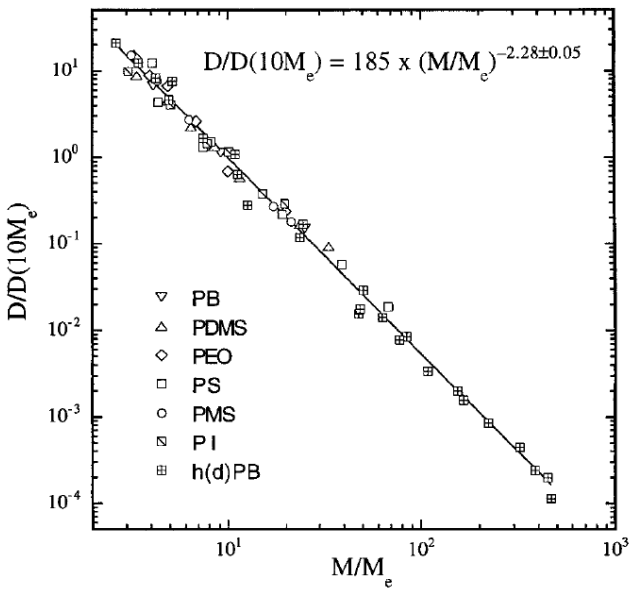

Figure 4.12: A collection of data on the self diffusion coefficient of high molecular weight polymer melts normalized and plotted as a function of rescaled molecular weight. A best fit to the entire collection of data provides $D \propto M^{-2.28\pm0.05}$. Image reproduced from [31].

elastic deformation which upon release of the stress is completely removed and the system is restored to it's original state. The elastic response is described by,

$$\sigma = \beta\epsilon \tag{4.18}$$

where σ is the applied stress, ϵ the resulting strain, and β the elastic modulus. In contrast when a stress is applied to a Newtonian liquid the work done on it is entirely dissipated through molecular motions as heat, the response is given by,

$$\sigma = \eta\frac{\partial\epsilon}{\partial t} \tag{4.19}$$

where η is the viscosity. The response of a polymer system however is not as simple. Figure 4.13 shows an example response of a polymer system to an applied uniaxial tensile load in a simple creep experiment. The response is a superposition of three components:

- An instantaneous elastic response
- A retarded elastic response
- A viscous flow

After removal of the stress there is an instantaneous contraction owing to the elastic component, followed by a slow time dependent recovery from the anelastic component, the viscous component is irreversible and does not recover. In explaining this behaviour one defines the *tensile creep compliance*,

$$D(t) = \frac{e(t)}{\sigma_0} \tag{4.20}$$

A separate experiment that one can use to elucidate the viscoelastic behaviour of polymers is a stress relaxation experiment. Here a constant strain is imposed on the system and the stress is tracked as a function of time. The stress is at a maximum instantaneously, the anelastic component results in an initial decay, and viscous flow will ultimately return the stress to zero. In describing this experiment we define the *time dependent tensile modulus*,

$$E(t) = \frac{\sigma(t)}{e_0} \tag{4.21}$$

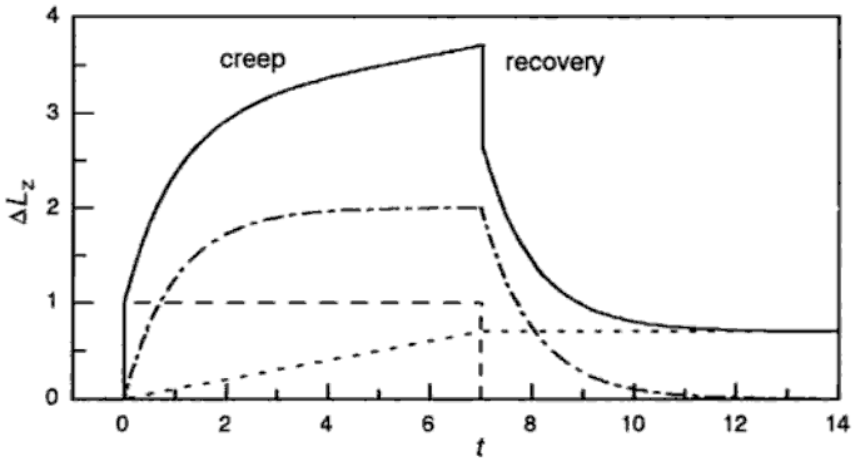

Figure 4.13: An example of a polymer response to an applied tensile load, the elongation ΔL_z (solid line) is a superposition of an elastic deformation (dashed line), viscous flow (dotted line), and a retarded anelastic component (dash-dot line). Image reproduced from [25].

Finally we consider a dynamic mechanical experiment, whereby an oscillatory stress is imposed on the sample,

$$\sigma(t) = \sigma_0 e^{i\omega t} \tag{4.22}$$

The response is a time dependent oscillatory strain but with a phase delay with respect to the stress,

$$e(t) = e_0 e^{i\omega t} \cdot e^{-i\delta} \tag{4.23}$$

In describing such an experiment one considers the *dynamic tensile compliance*,

$$D^*(\omega) = \frac{e(t)}{\sigma(t)} = \frac{e_0 e^{-i\delta}}{\sigma_0} = D' - iD'' \tag{4.24}$$

and the *dynamic tensile modulus*,

$$E^*(\omega) = \frac{1}{D^*(w)} = E' + iE'' \tag{4.25}$$

All of the above examples have been for tensile stress experiments however analogous compliances/moduli can be defined for shear experiments.

4.2 The Glass transition

A glassy material is most simply described as a material which combines the mechanical rigidity of a solid with the disordered structure of a liquid. To form a glass all that is required is a cooling from the liquid state at a sufficiently high cooling rate; the cooling rate required is largely material specific. Perhaps the most striking feature of glass formation is the dramatic change in system viscosity, upon cooling from the crystal melting temperature to the glass transition temperature the viscosity changes over some 14 orders of magnitude without any pronounced change in the molecular structure. To understand the basic concept of glass formation consider what is happening at the molecular level as a liquid is cooled. In the liquid state there is no long-range order between molecules and molecules are moving around rapidly due to thermal motions. As the liquid is cooled, thermal energy is removed from the system and molecular motions will slow. At this point one of two possibilities can occur depending on the cooling rate, for low cooling rates the molecules will begin to order into a low-energy crystalline, but for high cooling rates the molecules will not have time to order before the molecular motions are frozen out. We should then expect that for any material a transition to the glassy state exists provided a high enough cooling rate can be applied to it. Indeed this seems to be the case, experimental cooling rates of 10^5 Ks^{-1} and greater have been used to form metallic glasses [32], and simulations which can access cooling rates 10^{12} Ks^{-1} not available to experimenters have shown that even simple liquids such as Argon can form glasses [33]. Despite being an active area of research for the better part of a century, there are many outstanding issues in our understanding of the glass transition. Here we introduce some of the observed peculiarities of the glass transition and several theories attempting to explain them.

Unlike the liquid-solid phase transition there are no sudden structural changes associated with the glass transition. As a consequence the familiar signatures of the first-order liquid-solid transition, a discontinuity in the specific volume and a large latent heat, are absent in the glass transition. If we consider specific volume as a function of temperature we can find a set of curves shown in figure 4.14. When the liquid is cooled below T_m, but before the glass transition occurs, the system is in the supercooled liquid state. The supercooled liquid state is metastable, it represents a minimum in the free energy landscape but not the global minimum which is the crystal state. In this state molecular motions become very slow, however the molecules are still able to rearrange themselves

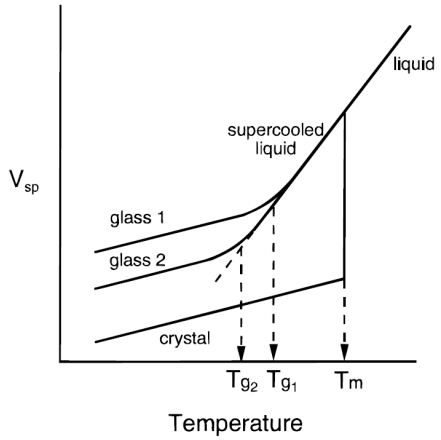

Figure 4.14: Schematic plot of specific volume versus temperature. At slow cooling rates the system can crystallize and there is a jump in the specific volume at the melting temperature T_m. The observed glass transition temperature and the properties of the resulting glass depend on the cooling rate; glass 2 is formed at a slower cooling rate than glass 1. T_g is identified here as the intersection of the extrapolated glassy specific volume and the extrapolated supercooled liquid specific volume. Image reproduced from [34].

such that the equilibrium thermodynamic properties expected from extrapolating the liquid properties are found. As the system goes through the glass transition the molecular motions become so slow that the rearrangements required to maintain these equilibrium properties are no longer possible on the experimental timescale. At this point the specific volume and other properties deviate from the extrapolated line and the system goes into an unstable state. In this glassy state the system is not at a local free energy minimum and as a result the system is constantly moving towards some local free energy minimum albeit on a timescale which may be too long to observe experimentally. This ever-present slow relaxation is called aging. If this experiment is repeated at a slower cooling rate then the experimental timescale increases and the system can find the equilibrium supercooled liquid state at lower temperatures than was available when a higher cooling rate was used; as a result a lower T_g is observed. In order to reconcile the differing T_g values obtained due to different cooling rates a common standard definition of T_g is the isoviscous definition where T_g is defined as the temperature at which $\eta = 10^{13}$ P, or similarly when the timescale of relaxation $\tau \sim 100$ s. It is clear from this example that the glass transition bears no resemblance to the first-order liquid-solid phase transition. The glass transition is often

referred to as a kinetic transition as the entire process is the result of changes to the kinetic properties of the system.

A common quantity used in describing the macroscopic properties of the supercooled liquid as the glass transition is approached is the viscosity (or equivalently a characteristic relaxation time). In this regime the viscosity can often be modeled with some success by the Vogel-Tammann-Fulcher (VTF) equation,

$$\eta = \eta_0 \exp\left(\frac{B}{T - T_\infty}\right) \tag{4.26}$$

where B and T_∞ are material specific constants determined empirically. In the limit of $T_\infty = 0$ the equation is referred to as the Arrhenius equation. Glassy systems whose viscous behaviour is well described by the Arrhenius relation are classified as *strong* glasses; In contrast materials which undergo non-Arrhenius relaxation processes (VTF or otherwise) are classified as *fragile* glasses. For $T_\infty \neq 0$ we see that VTF equation predicts a divergence in viscosity at T_∞.

Supercooled liquids are often observed to have more than one relaxation process and consequently multiple observable relaxation times. Consider for example a dielectric relaxation experiment whereby the system is given a net polarization by an electric field pulse and the systems recovery towards randomized orientations is observed. Well above T_g there is a single relaxation process known as the α-process which is well described by Arrhenius behaviour. However as the temperature is lowered towards T_g a second relaxation process termed the β-process emerges which is faster than the α-process. Simultaneously the Arrhenius behaviour of the α-process breaks down and VTF behaviour begins. Figure 4.15 shows the behaviour of the observed relaxation times dependence on temperature compiled from many experiments. Note the divergence of the α-relaxation time as predicted by the VTF equation.

An interesting problem observed by Kauzmann [35] known as the Kauzmann entropy crisis arises when one considers the entropy of a supercooled liquid. Differential scanning calorimetry can be used to track the specific heat of a supercooled liquid as it is cooled through the glass transition, integrating the specific heat curve one obtains the specific entropy as a function of temperature. Figure 4.16 shows a schematic plot of entropy as a function of temperature. For the crystal curve there is a jump in the entropy upon crystal formation at T_m. For a glass forming experiment the entropy deviates from the extrapolated supercooled liquid line. Recall that for a lower cooling rate T_g is found at lower

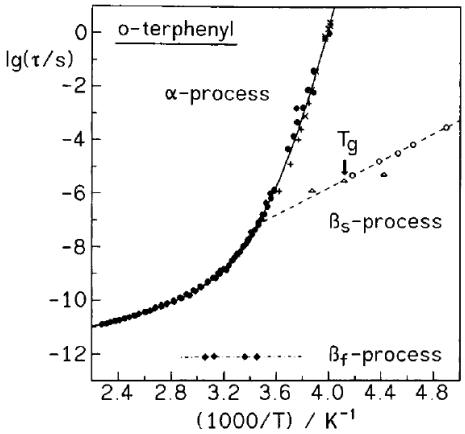

Figure 4.15: Plot of logarithm of observed relaxation times versus inverse temperature compiled from multiple experiments. There are three separate processes visible here. The slowest process is the α-process which is often well described by the VTF equation. The other processes are the β processes. Image reproduced from [34].

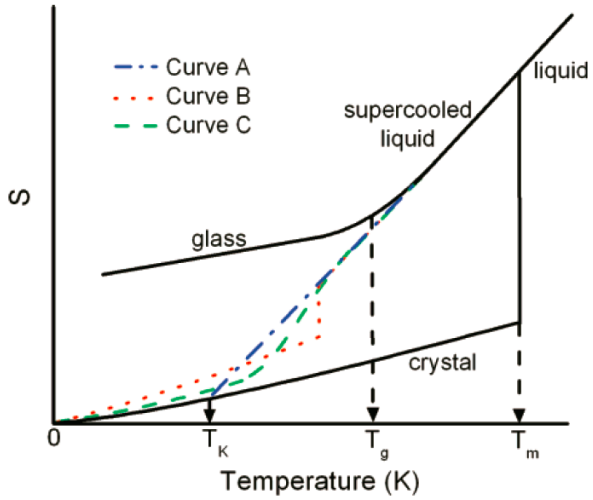

Figure 4.16: Schematic plot of entropy versus temperature illustrating the Kauzmann entropy crisis and some possible resolutions. The solid lines represent typical curves obtained for glass and crystal formation. The dot-dash line is an extrapolation of the supercooled liquid entropy, it's intersection with the crystal curve marks the Kauzmann temperature T_K. The dotted and dashed lines represent possible solutions with a first-order phase transition and no phase transition respectively. Image reproduced from [36].

temperatures, this pushes the deviation from the supercooled liquid behaviour to lower temperatures. The entropy crisis is that if one cooled the supercooled liquid at a slow enough cooling rate than an extrapolation of the observed supercooled liquid behaviour predicts an entropy equal to the crystalline state, and below this temperature the entropy of the liquid could actually be lower than the crystal. The intersection of the extrapolated supercooled liquid line with the crystal's entropy curve marks the Kauzmann temperature T_K. This intersection is typically found around $T_g - 50K$ [37]. If this supercooled liquid behaviour were to continue past T_K, not only would the entropy drop below that of the crystal, but it would soon become negative which violates the third law of thermodynamics. Unless one is willing to disregard the laws of thermodynamics it is safe to say that some process must intervene at temperatures near T_K. For this reason T_K gives us an approximate lower bound on the possible values of T_g no matter how slow the liquid is cooled. In figure 4.16 two possible solutions are proposed, the dotted line suggests that at some temperature slightly greater than T_K a first order phase transition may occur and the slope of the entropy-temperature curve in the resulting state could be low enough to ensure that the crystal curve is intersected at $T = 0$. The dashed line suggests that before reaching T_K the system is required to undergo a transition resembling the glass transition and the crystal curve is again intersected at $T = 0$.

Finally we mention the existence of nonexponential relaxation processes in supercooled liquids and glasses. It is often observed for supercooled liquids that the response functions depart from single exponential forms as the temperature is lowered towards T_g. For example in a dielectric relaxation experiment the recovery of isotropic orientations following a net polarization does not always follow a simple exponential form. In describing the observed response functions the Kohlrausch-Williams-Watts (KWW) stretched exponential equation is often used,

$$\phi(t) \propto e^{-(t/\tau)^{\beta}} \tag{4.27}$$

In reconciling nonexponential relaxation processes with a physical explanation one can imagine two scenarios; (1) the system is homogeneous and at all locations nonexponential relaxation occurs, (2) the system is dynamically heterogeneous, everywhere single exponential relaxation exist but the relaxation time varies between regions, the macroscopic response averaged over these different regions results in nonexponential behaviour. Results from computer simulations seem to suggest the heterogeneous picture [38, 39] and experimental evidence is also growing for the heterogeneous view, specifically from studies

on colloidal systems [40, 41, 42].

4.2.1 Theoretical Approaches

In spite of many years of intense theoretical efforts there exists no theory which can offer a satisfying description of all aspects of the glass transition. Here we discuss some of the leading theories.

Adam-Gibbs Theory: Cooperatively Rearranging Regions

The Adams-Gibbs theory of the glass transition [37] aims at describing the temperature dependence of supercooled liquid relaxation behaviour in terms of the configurational entropy of the system. More specifically, the theory tries to rescale the empirical relation for the relaxation behaviour, the Williams-Landel-Ferry (WLF) equation, into a more universal form. The WLF equation is given by,

$$-\log a_T = -\log \frac{\tau(T)}{\tau(T_R)} = C_1 \frac{T - T_R}{C_2 + (T - T_R)} \tag{4.28}$$

where a_T is the ratio of relaxation times at temperatures T and T_R, and the constant C_1 and C_2 are empirically determined. Often the values of $C_1 = 8.86°C$ and $C_2 = 101.6°C$ yield a good fit provided the reference temperature T_R is chosen correctly. The Adam-Gibbs theory relies upon the assumption of cooperatively rearranging regions (CRR) and heterogeneous dynamics. The system is viewed as an isothermal-isobaric ensemble of subsystems each with the size of a CRR. A CRR is formally defined by Adam and Gibbs as "*a subsystem of the sample which, upon a sufficient fluctuation in energy (or, more correctly, enthalpy), can rearrange into another configuration independently of its environment*" [37]. This leads to the idea of a characteristic length scale in the system, ξ, which is identified here as the size of a CRR. The theory is developed by finding the average probability that a CRR will undergo a rearrangement,

$$W(T) = A \exp\left(-\frac{\Delta\mu s_c^*}{k_b T S_c}\right) \tag{4.29}$$

Where A is a temperature independent constant, $\Delta\mu$ is the energy barrier per molecule for a rearrangement, s_c^* is a lower limit to the configurational entropy of a CRR, below s_c^* no rearrangement is possible, and S_c is the configurational entropy of the macroscopic

system. Since the probability of rearrangements is inversely proportional to the relaxation time, the WLF equation can be rewritten and a set of expressions for the constants C_1 and C_2 is found,

$$C_1 = \frac{1}{\log e} \cdot \frac{\Delta\mu s_c^*}{k_b \Delta C_P T_R \ln(T_R/T_2)} \tag{4.30}$$

$$C_2 = \frac{T_R \ln(T_R/T_2)}{1 + \ln(T_R/T_2)} \tag{4.31}$$

with ΔC_P the difference between the specific heats in the equilibrium supercooled liquid and the glass at T_g, and T_2 is identified as the temperature at which the configurational entropy reaches zero. The theory predicts the existence of a second-order phase transition at $T = T_2$, physically this can be interpreted as a divergence of the length scale ξ. Comparing this result to the experimental findings of 15 different glass forming materials Adam and Gibbs found that this transition should occur at a temperature of $T_g - 55°C \pm 10.9$ [37]. Note also that this theory poses to reconcile the entropy crisis by means of the second order phase transition at T_2.

Free Volume Theory

The next theory we consider is the free volume theory developed throughout the 20^{th} century in a number of papers [43, 44, 45] to name a few. The underlying idea of the free volume theory is that there exists an appreciable amount of *free volume* within the system, distributed throughout as voids. These voids facilitate the movement of molecules with a minimal energy cost. The drastic increase in system viscosity is then explained by a dearth of free volume rather than by increasing molecular motion energy barriers. The average free volume per molecule is intuitively determined by,

$$\bar{v_f} = \frac{V}{N} - v_{mol} \tag{4.32}$$

Where V and N are the macroscopic system volume and number of molecules, and v_{mol} is the volume of a single molecule. When the systems thermal expansion coefficient is a constant, as it is in the supercooled liquid, this can be rewritten as,

$$\bar{v_f} = \frac{\alpha(T - T_o)}{N} \tag{4.33}$$

where α is the thermal expansion coefficient and T_o the temperature at which the free volume reaches zero. Molecular transport or rearrangement in this model is proportional

to the probability of finding a void larger than the critical free volume v_c at which transport is not possible. This probability is assumed to take an exponential form,

$$P(v_f) = \frac{1}{\bar{v}_f} \exp\left(-\frac{v_f}{\bar{v}_f}\right) \tag{4.34}$$

The relaxation time should then be proportional to the inverse of $P(v_c)$,

$$\tau \propto A \exp\left(\frac{v_c}{\bar{v}_f}\right) \tag{4.35}$$

Inserting equation 4.33 we find the familiar VTF equation,

$$\tau \propto A \exp\left(\frac{V_c}{\alpha(T - T_o)}\right) \tag{4.36}$$

The free volume theory has success in explaining the dramatic increase in viscosity as temperature is lowered, however the theory has many shortcomings. The theory makes no predictions about the existence of nonexponential relaxation functions or of heterogeneous dynamics. A strikingly contradictory observation is that of a glass transition under isochoric conditions [46] which undermines the concept that the reductions in free volume are the cause of the slowing of molecular dynamics.

Mode Coupling Theory

One of the most successful theories of the glass transition is the mode coupling theory (MCT) [47, 48, 49, 50, 51, 52]. Mode coupling theory has been developed over the last $\sim$ 25 years, it takes it's roots from the well developed molecular theories of simple liquids. The basic concept of the MCT is not so intuitive as our other models; it relies upon the notion of nonlinear feedback mechanisms in the molecular dynamics. Glass formation is viewed as an increase in the strength of this feedback mechanism resulting in the arrest of molecular motions. The only intuitive physical notion employed in the MCT is that of the 'cage effect' whereby a particular molecule in the liquid is trapped within a cage formed by neighbouring molecules. Escape from the cage primarily occurs when the cage breaks up and the particle is free to move on. In an extended MCT formulation escape form the cage is also permitted by a hopping process whereby the particle overcomes the energy barrier of the cage. The details of the MCT formulation (as well as it's history) are quite complex and not much is elucidated from their presentation, for this reason we do not attempt

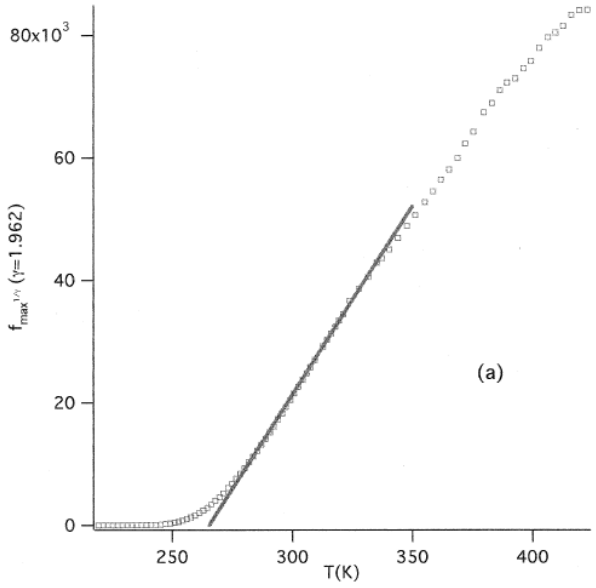

Figure 4.17: Plot of $f_{max}^{1/\gamma} \propto \tau^{-1/\gamma}$ versus temperature the open squares are experimentally determined values from dielectric relaxation experiments, the solid line represents the prediction of the MCT power law with $T_C = 262K$. Reproduced from [50].

a derivation of the MCT here and refer the reader to the references mentioned above. Rather we will discuss some of the predictions of MCT and how these predictions stand up to results of experiments and computer simulations. One of the main predictions of MCT is a power law dependence of the relaxation time, or inversely the diffusion constant,

$$\tau \propto D^{-1} \propto (T - T_c)^{-\gamma} \tag{4.37}$$

where T_c is the critical temperature where the idealized MCT predicts a divergence of the relaxation time. Figure 4.17 is a plot of $f_{max}^{1/\gamma} \propto \tau^{-1/\gamma}$ versus temperature. The open squares are experimentally determined values from dielectric relaxation experiments the solid line represents the prediction of the MCT power law. We see that the power law fits the data in a limited temperature range breaking down below $T_C = 262K$ and at high temperatures. Often the full MCT is too complex to be solved by non-numerical methods, as such simplifying assumptions are commonly made and schematic models are studied instead. One such schematic model is for the density correlation function $\Phi(t)$,

$$\ddot{\Phi}(t) + \Omega^2\Phi(t) + \nu\dot{\Phi}(t) + \Omega^2 \int_0^t m\left[\Phi(t-t')\right]\dot{\Phi}(t')dt' = 0 \tag{4.38}$$

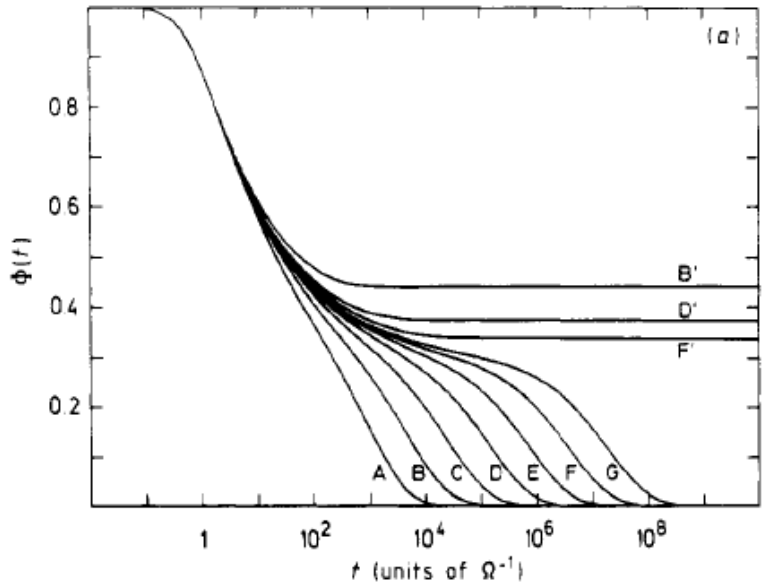

Figure 4.18: Plot of the density correlation function versus time, the different curves can be interpreted as different temperatures, with temperature decreasing from A outwards. Image adapted from [53].

where Ω is a microscopic frequency, ν a damping constant, an $m\left[\Phi(t-t')\right]$ is a coupling parameter which is itself a polynomial in Φ. Figure 4.18 shows the time dependent behaviour of this correlation function using the coupling parameter $m\left[\Phi(t-t')\right] = \lambda_1\Phi + \lambda_2\Phi^2$. In this plot the different curves are equivalent to changing temperature with high temperatures starting at A and decreasing towards G. At high temperatures, curve A, the relaxation which is almost linear on this plot corresponds physically to single exponential relaxation behaviour. As temperature is increased this process not only slows, but a second process begins to appear as a 'hump' in the curve. Physically this hump is interpreted as a manifestation of the cage effect, the cage slows relaxation and upon relaxation of the cage the particle resume it's relaxation now following a stretched exponential behaviour. The relaxation during the hump is attributed to β-relaxation and upon release of the cage the relaxation corresponds to α-relaxation. As the temperature is lowered below T_C the timescale of the β relaxation stretches out and that of α-relaxation diverges. The ability of the MCT to predict these multiple relaxation processes is one of the main strengths of the MCT. The major downfall of the MCT theory is that it predicts T_C to reside well above the

experimentally observed T_g, typically around 1.2 T_g. Thus one would not expect relaxation to occur in the supercooled liquid as T_g is approached. In the extended MCT the existence of the hopping process allows for relaxation to occur below T_C. However this is still a cause for concern because the theory predicts a divergence of relaxation times/viscosity at T_C, above T_g

Edwards Tube Model

The Edwards tube model, developed to study the dynamics of polymer systems in the vicinity of T_g, makes the simplifying assumption that a polymer melt can be represented as a series of rigid rods. The justification for this is that in the highly entangled melt the tube model, mentioned in the development of the reptation model of polymer dynamics, should be applied. To make the model simpler the tubes are straightened into rods and their rotational and diffusive motions are considered. The tube model is actually quite similar to the Adam-Gibbs theory in that the drastic slowing of dynamics is caused by the onset of cooperative rearrangements of the rods. Figure 4.19 depicts the simplified system, the rotational freedom of the central rod is hindered by the presence of the surrounding rods. In addition to reduced rotational motion, the translational motion of the rods is also hindered, specifically the model considers translational motion along the tube created from the surrounding rods. Motion along this tube will be constrained due to rods blocking the path acting as obstacles, these blockades are viewed as perfectly reflecting barriers which open and close. We follow the derivation given by Edwards and Evans [54]. Considering the effect of these blockades on the diffusion of a specific rod, the diffusion constant along the tube is found by,

$$D = \frac{D_o}{1 + gL\rho_B\tau} \tag{4.39}$$

where D_o is the diffusion constants along the tube without blockades, g a numerical constant, τ the lifetime of a blockade, L the length of the tube, and ρ_B the number of barriers per unit time. However this does not take into account that the barriers are also diffusing under the delay of other rods. Accounting for this through a self-consistent arguement the diffusion constant is given by,

$$D = D_o \left[1 - \frac{8}{3\sqrt{\pi}}(cdL^2)^{3/2}\right] \tag{4.40}$$

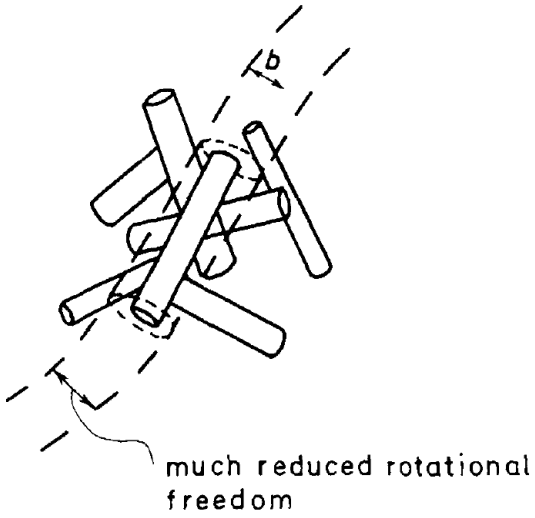

Figure 4.19: Schematic illustration of the simplified system considered in the tube model. A polymer melt is considered as a system of rigid rods. As concentration increases the rotational freedom of the rods is reduced due to the presence of the surrounding rods. The translational motion of the rod is restricted to lie along the tube created by the surrounding rods. Image reproduced from [54].

where c is the concentration of rods, and d the diameter of the rods. In a subsequent paper by Edwards and Vilgis [55] the authors extend this result by expanding the equation around T_g where the diffusion constant approaches zero,

$$D \approx \frac{D_o}{T_g}(T - T_g) \tag{4.41}$$

Up to here we have been discussing a model which only considers independent motions of rods, but by including the effect of cooperative motions of rods it can be shown,

$$D = D_o \exp\left(-\frac{\Delta T_g^2}{4T_o(T - T_o)}\right) \tag{4.42}$$

which is equivalent to the VTF equation. So by considering the simplified model of a system of rigid rods and including the concept of cooperative motions the Edwards tube model is able to predict the VTF equation. Although this is not a groundbreaking result, the Adam-Gibbs and free volume model also predict the VTF equation, the strength of the tube model lies in it's intuitively simple picture of the dynamics.

4.3 Glassy Systems in Confinement

From the discussion above it is clear that there is still much to be learned regarding the glass transition. Here we present a review of some key experimental findings and motivate the experimental work to be discussed in the subsequent chapters. Our attention here is focused on the properties of glass forming systems under confinement, where the sample geometries approach the nanoscale. Studies can be classified based on the type of measurement performed, as a thermodynamic or dynamic measurement. Thermodynamic measurements are those that measure the thermodynamic properties of the sample (specific heat, volume, etc.), dynamic measurements are concerned with quantities reflecting the molecular dynamics of the system (viscosity, relaxation times, etc.).

A distinction should be made here for glass forming materials between polymeric and molecular systems as the experiments on these systems often present different challenges. Due to the macromolecular nature of polymers, it is possible to create ultrathin polymer films, where the thickness approaches the nanoscale, which are stable against break-up. In contrast thin molecular films are difficult to create and they tend to break up into a

series of small droplets (a process known as dewetting) at thicknesses much larger than those required to observe confinement effects. For this reason experimental studies aimed at studying glassy properties for polymer systems are typically performed in thin film geometries while molecular glasses are studied under confinement within 3 dimensional nanoporous networks. We follow this distinction and break the review up into two sections, a review of the literature on molecular glasses under confinement and a discussion of the findings for thin polymer films.

4.3.1 Molecular Glasses Under Confinement

We begin by considering the properties of molecular glasses constrained within nanopores. There is a wealth of information regarding these systems resulting from many studies from multiple research groups. Unfortunately there does not seem to be a consensus within the community on a model system to study or on the porous material itself. The nanoporous material can have varying structures and furthermore the pores are commonly (but not always) given a chemical pretreatment to replace OH groups on the pore surface with a less polar group. The nature of the pore surface seems to play a significant role in the observed behaviour, and of course the material being studied can drastically change the observations, for these reasons it is often difficult to draw direct comparisons between studies. We bring together some of the major findings and attempt to point out where differing observations can be attributed to differences in the systems under study.

First let us consider measurements of the thermodynamical properties of molecular glasses under confinement in nanopores. Jackson and McKenna [56] in 1991 were among the first to measure the glass transition temperature of molecular glasses (o-terphenyl and benzyl alcohol) under confinement. The study uses differential scanning calorimetry (DSC) and observed that T_g under confinement was reduced relative to the bulk T_g. The observed reductions were on the order of ~ 10 K and were found to increase with decreasing pore size. Figure 4.20 summarizes their results. A subsequent study reported by Zhang et al. [57] also using DSC extended the study to additional materials (isopropylbenzene, glycerol, di-n-butyl phthalate, tert-butylbenzene, b-butyl acetate) and found similar behaviour with T_g reductions similar in magnitude. For the most part there is a consensus in the literature that T_g as measured through thermodynamic properties exhibits a reduction as a result of confinement into nanopores. One contradictory result can be found in the work of

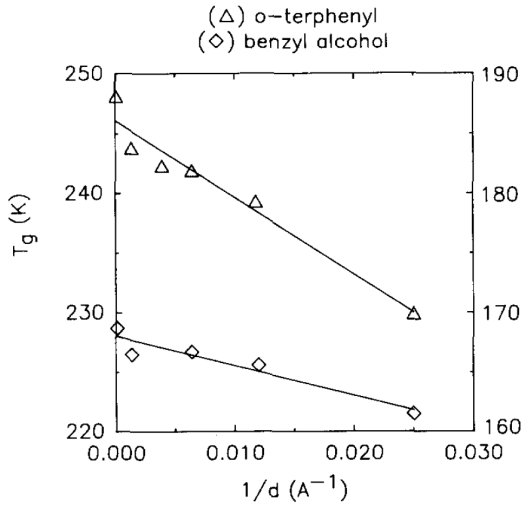

Figure 4.20: Plot of measured T_g versus the inverse of the nanopore diameter. Image reproduced from [56].

Alba-Simionesco et al. [58], using adiabatic calorimetry they found that benzene shows an increase in T_g upon confinement. This result should be interpreted as a difference due to chemical structure, experimental technique or confining material.

The next topic we explore is the observations of multiple T_g's under confinement, a topic which is closely related to that of multiple relaxation processes observed through dynamical measurements. Many studies have shown evidence for multiple glass transition processes upon confinement of molecular glasses [59, 60, 61, 62]. However the position of these transitions relative to bulk T_g tends to vary between the studies. Park and McKenna [59] studied o-terphenyl by means of DSC and found one transition below bulk T_g and one above. In agreement with the studies mentioned above [56, 57] the transition below bulk T_g was found to move to lower temperatures upon further confinement. The transition above bulk T_g displayed the opposite behaviour, moving to higher temperatures with decreasing pore diameter. However the literature does not observe this behaviour uniformly. Results from simulations [63] and dielectric relaxation studies in which the surface chemistry of the pores is modified [64, 62] show that the position (or presence) of this second process depends heavily on the strength of the interaction between the pore surface and the material under study. Arndt et al. [60] have used dielectric relaxation spectroscopy to study salol glasses in nanopores. They observe a second relaxation process which is orders of magnitude

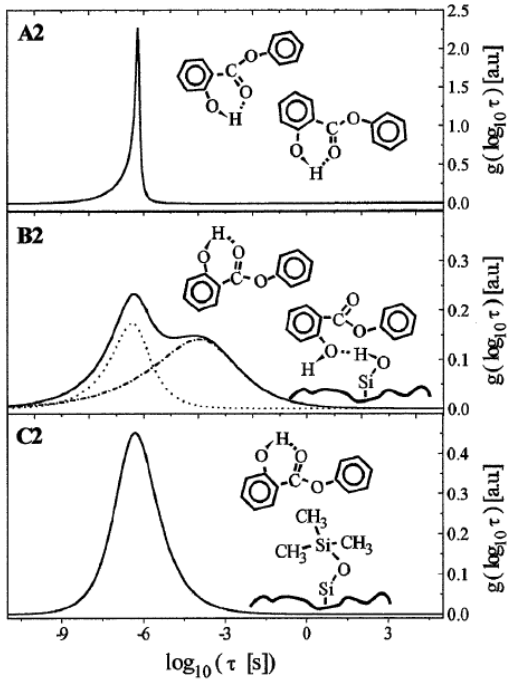

Figure 4.21: Distribution of the dielectric relaxation times for salol. The top plot is the bulk salol system, the middle plot is salol under confinement in 7.5 nm uncoated silica pores, and the bottom plot is under confinement in 7.5 nm trimethylsilyl coated silica pores. The diagrams illustrate the binding of salol molecules to the uncoated surface and the suppression of this interaction in the coated pores. Image reproduced from [60].

slower than the bulk process, however by coating the pore surfaces with trimethylsilyl, replacing the highly polar -OH coating, this secondary process can be removed entirely, see figure 4.21. The consensus then is that secondary (and even tertiary [61, 62] relaxation processes can appear upon confinement however they are strongly linked to the particular interactions between the material and the confining material. The physical picture is that in the presence of strong interactions a layer of material is formed at the pore surface which has a greatly reduced mobility relative to material closer to the pore center. Then one of the observed processes is due to relaxation of this surface layer and the other layer is attributed to relaxation of the interior material. These findings provide strong evidence for the dynamics in these confined geometries being highly heterogeneous.

The other major findings coming from dynamical studies on molecular glasses under

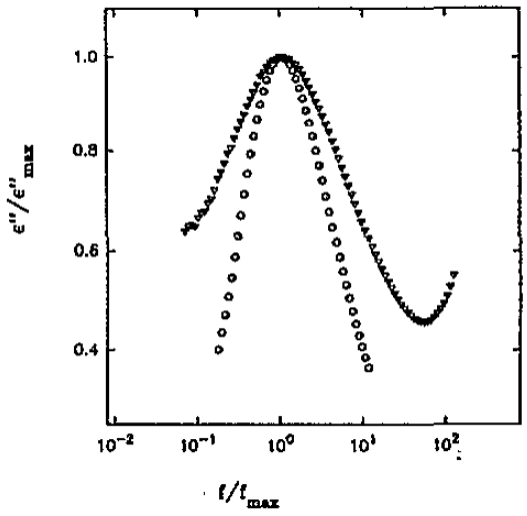

Figure 4.22: Normalized dielectric loss as a function of normalized frequency. Open circles are bulk glycerol and open triangles are glycerol under confinement in 4 nm diameter pores. Image reproduced from [65].

confinement is the behaviour of the α-relaxation process upon confinement. Using dielectric relaxation spectroscopy Pissis et al. [65] presented some of the first measurements on the dynamics of molecular glasses (glycerol, propylene glycol, and propylene carbonate) confined in nanopores, the main observation was a broadening of the dielectric relaxation. Figure 4.22 shows a plot of the normalized dielectric loss versus frequency for the bulk system and under confinement. Under confinement the spectrum is broadened relative to the bulk system. A similar broadening has been observed by Schuller et al. for propylene glycol [64] and N-methyl-ϵ-caprolactam (NMEC) [62]. These result are often interpreted in terms of the cooperativity length ξ from the Adam-Gibbs model, arguing that the dynamics should broaden as the system size approaches ξ. However this remains a questionable statement. Dielectric relaxation studies also find that the observed α-relaxation times can be increased relative to bulk upon confinement [64, 66, 67]. The authors explain this as a consequence of binding between the liquid material and the pore surface resulting in a glassy layer at the pore surface.

So we see that molecular glass forming materials upon confinement in nanopores can display a variety of behaviours regarding their dynamical and thermodynamical properties. Unfortunately the interaction between the confined fluid and the confining walls seem to

play a large role in determining the fluids response to confinement. This can often make comparisons between studies difficult. Regarding T_g in these systems, there seems to be a consensus that when the interactions between the fluid and the pores are weak the observed T_g's will tend to reduced values. In contrast, when there are strong interactions T_g can be observed to increase and dynamical measurements reveal additional relaxation processes which can be attributed to relaxation of surface layers at the pore interface.

4.3.2 Glass Transition in Thin Polymer Films

We turn our attention now to studies of the glass transition in thin polymer films where confinement is achieved by decreasing the film thickness to the nanoscale. As with molecular glasses under confinement there is a wealth of information in the literature on the topic. Unlike the situation in molecular glass systems the polymer community for the most part has done a good job of studying select model systems (usually PS or PMMA on silicon), typically studies on other systems are only performed if an explicit test of an alternate system is required. For this reason comparisons between different experimental techniques and research groups are easier to draw. We break up our discussion of the field into two sections, measurements of T_g reductions, and studies on the properties of the free surface. We pay particular attention to this second area of research as it is directly related to the topic of this thesis.

T_g Reductions

We begin our discussion, where most discussion on glassy polymer films in confinement do, with the seminal work of Keddie, Jones, and Cory [68]. Using the method of Beaucage et al. [69] for determining the glass transition temperature of a thin polymer film supported by a reflective substrate via ellipsometry, Keddie et al. measured T_g as a function of film thickness for polystyrene (PS) on silicon substrates. A striking decrease in T_g relative to it's bulk value was observed for film thicknesses $\leq$ 50nm. Rather than plotting the result from this original study we show a master plot which is a compilation of a number of studies [68, 70, 71, 72, 73, 74] including that of Keddie et al.. An additional point that can be taken from the study of Keddie et al. [68] is the importance of a samples thermal history in thin polymer film studies. Figure 4.24 plots film thickness as a function of temperature for a PS

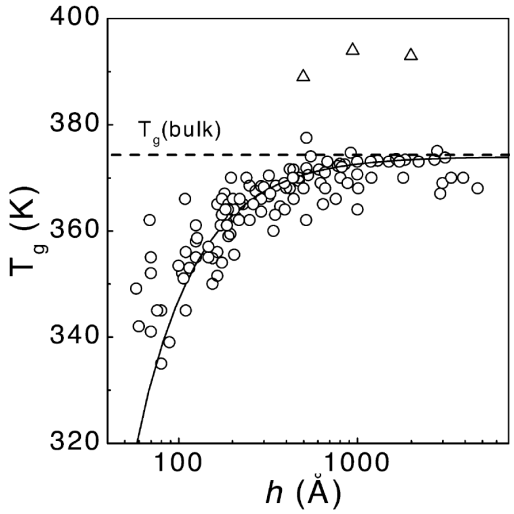

Figure 4.23: Plot of T_g as a function of film thickness, below thicknesses of $\leq$ 50nm T_g is reduced from it's bulk value. Image reproduced from [75].

film. The open circles here represent the data obtained upon first heating of the sample, the triangles and diamonds are from subsequent cooling and heating runs respectively. The difference in behaviour upon first heating can be attributed to built-in stress and/or retained solvent from the spin-coating process. To avoid this behaviour polymer films must always be annealed at temperatures above T_g prior to beginning studies. T_g in the subsequent heating and cooling runs is identified by the kink in the curve representing a change in the thermal expansivity of the film[2]. In explaining these T_g reductions the notion of a liquid-like layer at the free surface, with an enhanced mobility relative to the rest of the sample, was introduced. In this picture the size of the liquid layer is expected to grow as T_g is approached from below, and at T_g it is expected to diverge and span the entire sample. With this picture in mind the empirical relation,

$$T_g = T_g^{bulk}\left[1 - \left(\frac{a}{h}\right)^{\delta}\right] \tag{4.43}$$

is introduced to fit the observed T_g reductions. A best fit to the data in figure 4.23 yields $\delta = 1.8$ and $a = 3.2$ nm. In these studies on supported PS films no molecular weight (M_w) dependence is observed. Similar studies of T_g as a function of thickness have also been

[2]Note that the thermal expansivity as determined by this method is not the true volumetric thermal expansivity as expansion is only measured along the surface normal.

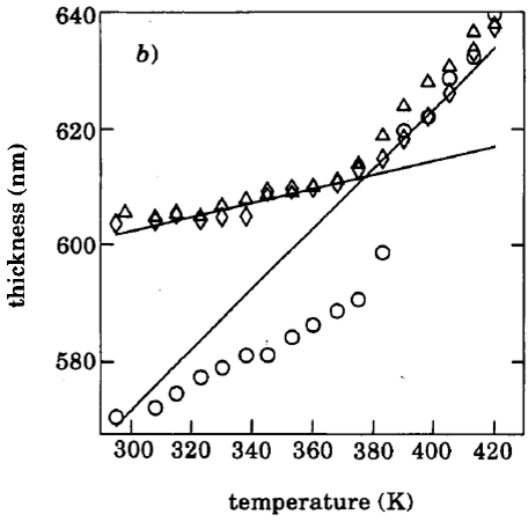

Figure 4.24: Plot of film thickness as a function of temperature. Open circles are obtained upon first heating of the sample, triangles and diamonds are from subsequent cooling and heating runs respectively. Image reproduced from [68].

performed for different polymer species. Prucker et al. [76] have considered the case of PMMA supported by a (treated) hydrophobic glass substrate and show that T_g decreases as the film thickness is decreased. Similar findings are observed for poly(methyl styrene), polysulfone, and poly(2-vinyl pyridine-co-styrene) [77, 78].

For PMMA a strong dependence on the underlying substrate and it's interaction with the polymer has been demonstrated [79]. On silicon wafers with the intact native oxide layer T_g is observed to increase with decreasing thickness, and on gold-coated silicon T_g reductions are found with decreasing thickness. Changing the stereo-chemistry of PMMA also has a drastic effect; isotactic and syndiotactic PMMA on treated silicon substrates are shown to display increased and reduced values of T_g respectively as film thickness is decreased [80]. This dependence of T_g on the substrate is explained by the notion that a strong polymer-substrate interaction leads to a reduction of polymer mobility near the substrate, the dependence on tacticity suggests there is some chain packing here. In contrast only a very weak substrate dependence is found in PS, some of the measurements compiled in figure 4.23 make use of different substrates and only a small scatter is found between them.

Given these findings on the substrate dependence, or lack there-of, of T_g reductions it

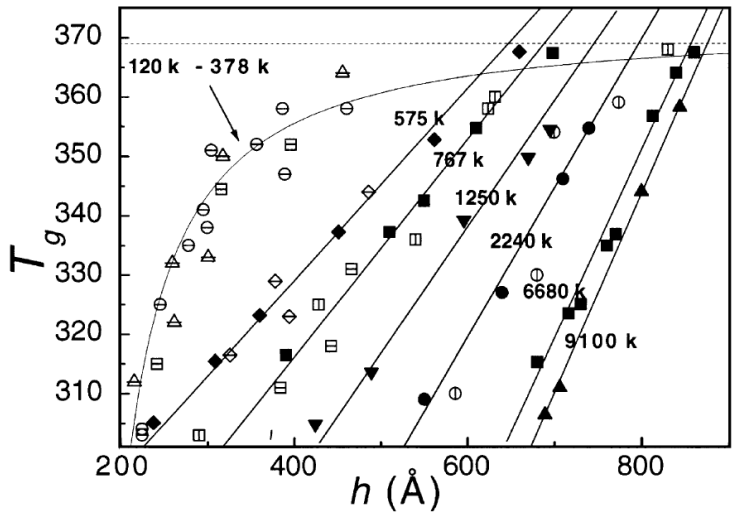

Figure 4.25: Glass transition temperature versus film thickness as determined by Brillouin light scattering (BLS) and ellipsometry on free standing films. Solid symbols obtained from ellipsometric studies [81], hollow symbols obtained from BLS, vertical bars from [73], horizontal bars from [82]. Image reproduced from [75].

is of interest to study freely standing films. In free standing films the supporting substrate is removed by floating the film off. During measurements the sample is typically held at the edges. Measurements on free standing PS films [81, 73, 82], show that the T_g reductions presented in figure 4.23 for supported PS films are greatly enhanced in the free standing configuration, figure 4.25. The T_g values of thin free standing PS films are also found to have a strong molecular weight dependence not found in supported films. For high molecular weights the qualitative behaviour of the T_g reductions changes from behaviour well described by equation 4.43 to a linear dependence. Looking at figure 4.25 we see that for molecular weights below 378 K there is no observable molecular weight dependence and the thickness dependence of T_g is again well described by equation 4.43. The crossover between high and low M_w behaviours is attributed to a competition of effects; at high molecular weights chain confinement effects are expected to cause the T_g reductions whereas the low M_w T_g reductions are attributed to finite size effects. Much more can be said about the high M_w behaviour however a full discussion is not required for the purposes of this thesis, the reader is referred to Forrest and Dalnoki-Veress [75]. In describing the low M_w behaviour one notices the film thickness dependence resembles

that of the supported PS films and equation 4.43 can again be applied. Retaining $\delta = 1.8$ a best fit yields $a = 7.8$nm which is roughly twice the value determined in the supported film fit. This leads one to return to the notion that the T_g reductions in the supported films were a result of a liquid like layer at the free surface. One would then expect that T_g reductions in the low M_w free standing films should be twice as large as their supported film counterparts, which is indeed the observed behaviour.

From these studies mentioned above it is clear that T_g reductions in thin polymer films is a commonly observed phenomenon, however it is not a universally observed phenomenon. Though this may lead some to believe there are controversies in the literature, a solid understanding of the physical mechanism responsible for T_g reductions should be able to resolve these controversies.

Surface Dynamics

This notion of heterogeneous dynamics in thin polymer films has be explored further by a number of techniques. Before discussing these experiments we note a famous quote attributed to de Gennes [83],

> *Future experiments should not aim at the determination of a single T_g, but at a distribution of T_gs*

One class of experimental measurements puts this quote to the test by measuring the local T_g value within thin layers embedded into a larger multilayer film [84, 85, 86]. The local T_g measurements are made using a fluorescent probe method. Thin films can be prepared with fluorescent molecules incorporated into the polymer network, this film can then be stacked at varying heights in a multilayer film. Figure 4.26 represents a typical plot of fluorescent intensity as a function of temperature. Much like the determination of T_g in ellipsometry experiments, T_g can be identified as the intersection of the extrapolated melt and glassy state behaviours. Using this method the local T_g can be measured as a function of depth by placing the labelled layer at different depths within the multilayer film. The studies find that the free surface T_g is reduced by an amount which depends on the overall film thickness, and that this reduced surface T_g extends tens of nanometers away from the free surface; affecting the measured T_g values over this range [86]. Figure 4.27 represents the measured T_g of the top 14 nm layer versus the overall film thickness. For films thicker

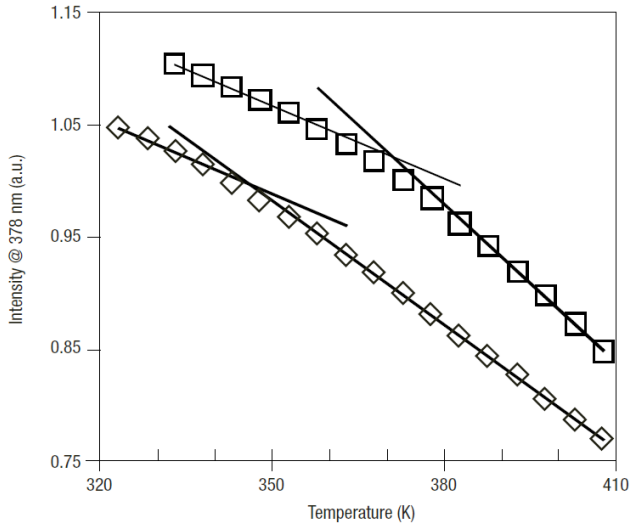

Figure 4.26: A typical plot of the fluorescence intensity from pyrene labelled PS single layer films 545 nm (squares) and 17 nm (diamonds) thick as a function of temperature. T_g can be identified by the intersection of the glassy and melt slopes. Image reproduced from [86].

than ~ 50 nm there is a large T_g reduction in this surface layer; below this thickness $T_{g,surf}$ increases towards $T_{g,bulk}$ until it intersects the curve of T_g reductions for supported PS films (solid line). There are however some issues concerning these measurements which one should take into consideration when interpreting these results. For example it may be possible that the multilayer films have an inherent built-in heterogeneity, the memory of free surfaces may not be entirely removed using the annealing conditions in [86]. Another study using the fluorescence method [87] considered the effect of the underlying material on the PS surface T_g. It was found that changing the supporting layer from PS to PMMA or P2VP could have drastic effects on the surface T_g of PS, almost removing the reductions entirely. This sensitivity to the supporting substrate has not been observed for PS in other studies and raises cause for concern. One concern that should not be overlooked here is the use of a T_g measurement which is an indirect measure of the dynamics. Furthermore T_g is only sensitive to average sample dynamics, not just the local dynamics; it should not be assumed that a T_g measurement taken in a constituent volume is unaffected by the surrounding material. Compounding this with the rather large size of the labelled layers, the spatial resolution of these studies is limited. Nevertheless the results coming from this

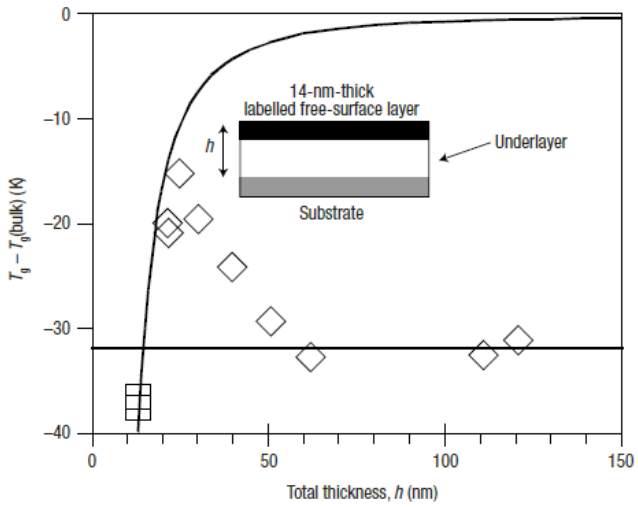

Figure 4.27: Plot of the measured T_g for a 14 nm thick fluorescently labelled layer at the free surface as a function of the overall film thickness (Diamonds). The squares are two measurements of the T_g shift for a stand alone 14 nm thick labelled film. The solid curve is a fit to data for single layer T_g as determined from the fluorescence method. Image reproduced from [86].

fluorescent technique clearly show the existence of a gradient in dynamics with the free surface being associated with higher mobilities.

The idea of enhanced surface mobilities is also supported by our final class of experiments which focus exclusively on the free surface properties and explore the notion of a free surface glass transition. The majority of the experiments discussed above have measured the thermodynamical properties of thin polymer films and in an indirect way conclusions are drawn regarding the dynamics in these films. It is prudent then to undertake studies which directly measure dynamical quantities and compare the results to those of thermodynamical studies.

Our discussion here begins by consider a class of experiments where polymer films are prepared with perturbations to the free surface topography and the relaxation of these perturbations are used to gauge the free surface dynamics. Kerle et al. were among the first to carry out such measurements [88]. Here the authors used the roughness of a calcium fluoride layer deposited onto the surface of a silicon substrate to cause a surface structure in the free surface of a PS film. By depositing a PS film on top of the calcium fluoride layer and subsequently dissolving the calcium fluoride (using HCL) a mirror image of the calcium fluoride roughness is produced on the PS film. The surface relaxation can then be measured by atomic force microscopy (AFM) at different stages of annealing. Figure 4.28 shows a representative set of AFM line scans at an annealing temperature of $\sim T_g - 32$ K. It is quite clear from this that the surface can relax at temperatures well below T_g. However at temperatures less than T_g a complete relaxation of the roughness was not observed in the 2880 min. time frame of the experiment; only the high curvature features are relaxed and the low curvature features persist.

In the work of Buck et al. [89] and Gasemjit et al. [90] a corrugated PS free surface is produced by hot embossing a master stamp into the surface of the film. The embossing is performed at temperatures well above T_g and contact is maintained for several hours to allow the polymers to locally relax into the corrugated structure. Again AFM is used to measure the surface topography at different stages of annealing. The advantage of this technique is that the regular structure of the corrugations allows one to straightforwardly model the decay process by means of the Navier-Stokes equation. Through this analysis the researchers are able to fit the observed data and extract out the surface viscosity, figure 4.29. In these studies partial relaxation of the surface roughness was observed for temperatures as much as 30 K below bulk T_g [89].

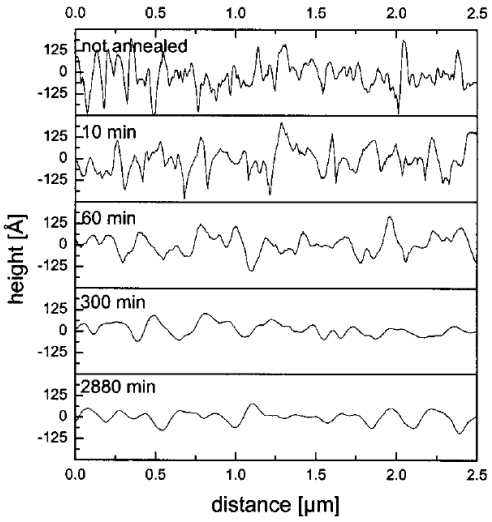

Figure 4.28: A representative set of AFM line scans for a sample annealed at $\sim T_g - 32K$. At this temperature the high curvature features are removed in the timeframe of the experiment but the low curvature features persist. Image reproduced from [88].

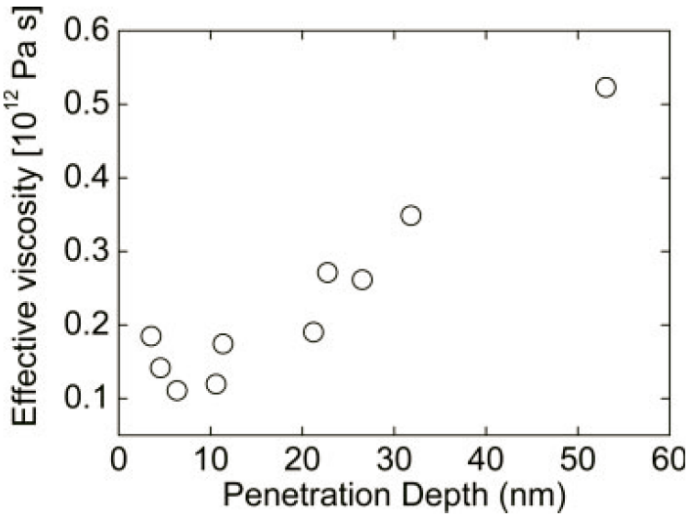

Figure 4.29: Effective surface viscosity at $T = 363K$ as a function of the penetration depth of the corrugations. Image reproduced from [90].

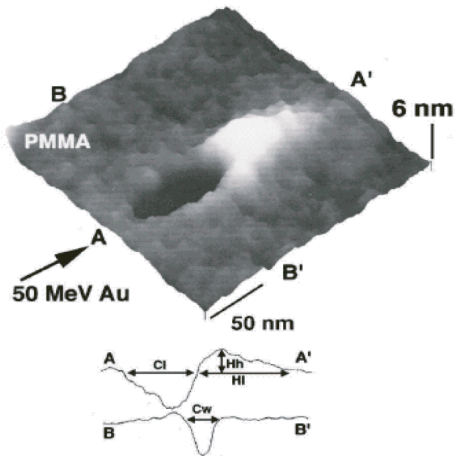

Figure 4.30: AFM image of a typical track created by Au ion bombardment. Image reproduced from [92].

Papaleo et al. [91] and Grohens et al. [92] have studied a similar process; nanometer scale tracks are created on the surface of PMMA films by bombardment with gold ions, the relaxation time of these tracks at different temperatures is tracked using AFM. Figure 4.30 shows a magnified view of a single track. The researchers tracked the relaxations of these surface features at temperatures below T_g, figure 4.31. A common definition of T_g is the temperature at which the systems relaxation time equals 100 seconds. With this definition $T_{g,surf}$ is placed at $T_g - 30$ K, consistent with the above mentioned studies.

Fakhraai et al. [93] and Qi et al. [94] have employed the method of surface nanohole relaxation to study the surface dynamics of thin PS [93] and PMMA [94] films. In these studies gold nanoparticles approximately 20 nm in diameter are deposited onto the polymer film surface and embedded several nanometers into the film by heating the film to temperatures slightly above T_g. The nanoparticles are subsequently dissolved using mercury, producing an ensemble of well defined spherical indentations in the film surface, figure 4.32. The time dependent relaxation of these deformations was then measured with AFM for temperatures below T_g. Relaxation of the surface holes was observed for temperatures as far as ~ 100 K below bulk T_g. Furthermore the relaxation occurs following a single exponential decay rather than a stretched exponential. Figure 4.33 shows the dependence of the observed lifetimes on temperature. Note the weak dependence on temperature: lifetimes change by only about 2 orders of magnitude as the temperatures is changed by about 90

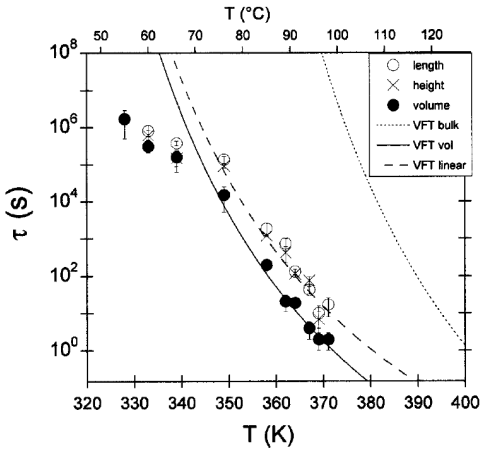

Figure 4.31: The relaxation times of the various surface feature dimensions versus temperature, for temperatures below T_g. For the higher temperatures studied (above $T = 340K$) the temperature dependence of the relaxation times is well described by VTF behaviour. A crossover from VTF to Arrhenius behaviour is observed as the temperature is decreased beyond $T = 340K$. Image reproduced from [91].

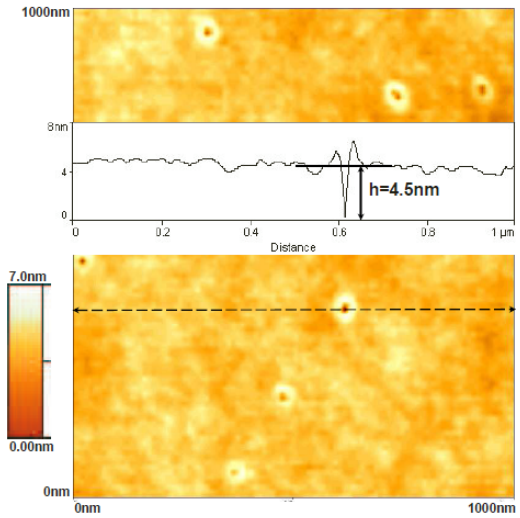

Figure 4.32: AFM image of a PS film surface showing the indentations produced from the dissolving of embedded nanoparticles. The accompanying line profile is take across the indicated position in the image, note the presence of a PS rim surrounding the holes. Image reproduced from [23].

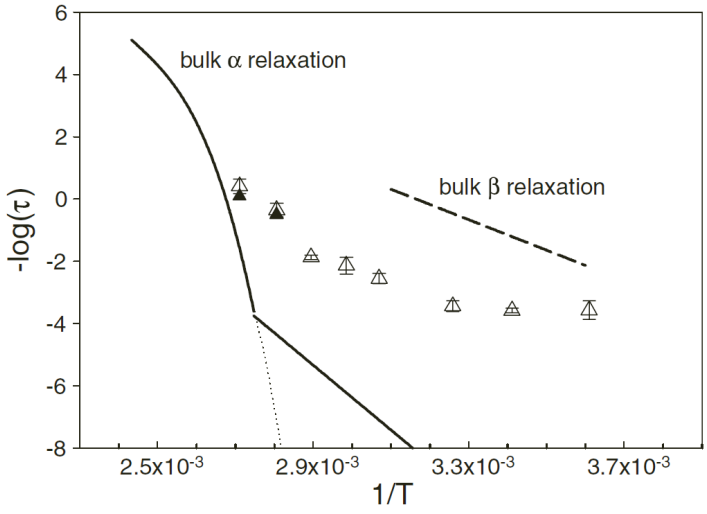

Figure 4.33: Plot illustrating the dependence of the relaxation time of surface nanodeformations on temperature. Open triangles are measured from relaxation of the holes and filled triangles from relaxation of the surrounding rims. The solid and dashed lines are the bulk α and β relaxations. Image reproduced from [93].

K. The dependence on temperature resembles that of Arrhenius behaviour but with faster dynamics then expected in the bulk (solid line). These results suggest that the surface does not experience a glass transition within the temperature window of the experiment which extends almost 100 K below bulk T_g.

Qi et al. have conducted a similar study on isotactic PMMA (i-PMMA) using the same technique [94]. The results show that the surface dynamics are enhanced relative to the bulk, however the qualitative dependence of the observed lifetimes is quite different from the case of PS. Figure 4.34 plots the dependence of the relaxation time on temperature for i-PMMA on silicon. The solid curve is the relaxation behaviour of bulk i-PMMA and the dashed curve is of the same form as the solid curve but with a shifted reference temperature. Based on this shift the authors attribute a surface glass transition at a temperature of $T_{g,bulk} - 41$ K. This study also showed a dependence on the choice of substrate, figure 4.35. We notice the correlation here with the T_g measurements from thermodynamical measurements discussed earlier in which the bulk PMMA T_g was found to have a strong substrate dependence [79, 80].

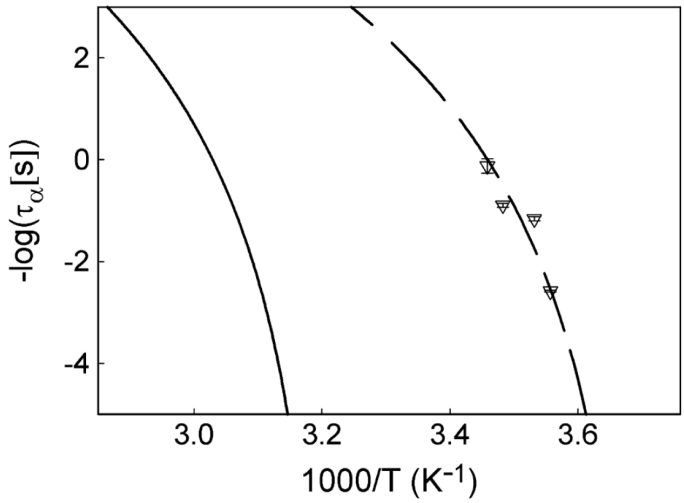

Figure 4.34: Plot illustrating the dependence of the relaxation time of surface nanodeformations on temperature for the case of i-PMMA on silicon. The solid curve is the bulk i-PMMA relaxation curve. The dashed curve is determined by a shift in the reference temperature for the bulk relaxation curve. Image reproduced from [94].

Forrest and coworkers have also studied the free surface properties of PS using the gold nanoparticle embedding technique [95, 96, 97, 24]. The technique uses AFM to track the apparent height of gold nanoparticles deposited on the surface of thin films. Nanoparticles are observed to embed into the surface at temperatures below bulk T_g indicating the presence of enhanced mobility in the free surface region, tracking the apparent nanoparticle height as a function of time provides dynamical information about the surface. Compared to the nanohole relaxation technique, this method is advantageous in that it provides a method of depth profiling the dynamics as the nanoparticles embed, furthermore the convolution of the AFM probe shape is less significant in determining a nanoparticle height as compared to a hole depth. The earlier studies [95, 96] considered a rather limited range of temperatures and embedding times and missed some of the observations found in subsequent studies [97, 24]. The main observation in these earlier studies was the existence of a liquid like surface layer $\sim$ 4nm in thickness for temperatures $\sim$ 10 K below the bulk T_g. The results coming from these nanoparticle embedding studies were interpreted in terms of a viscoelastic contact mechanics model [96] which provides an expression for the

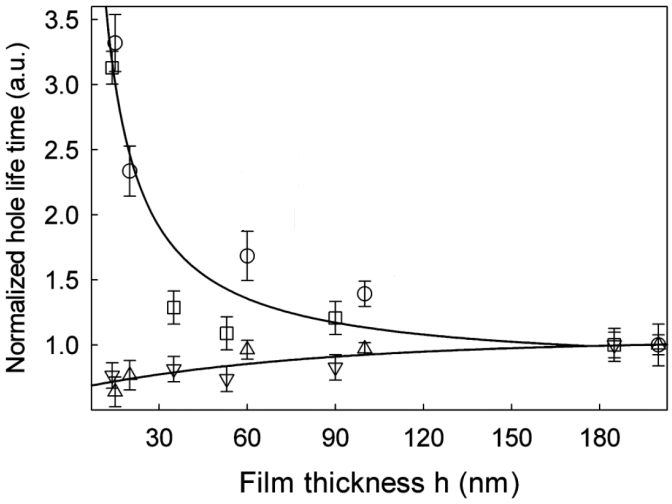

Figure 4.35: Plot combining the molecular weight, substrate, and film thickness dependencies of the surface deformation lifetimes. Data sets are as follows: circles $M_w = 212.4k$ on Si, squares $M_w = 889k$ on Si, upwards triangles $M_w = 212.4k$ on Al, downwards triangles $M_w = 889k$ on Al. Each data set is normalized to the observed lifetime in the thick film (180nm) limit. Image adapted from [94].

nanoparticle height as a function of temperature and time,

$$h(T,t) = 2R - \left(\frac{3(1-\nu)}{8\sqrt{R}} \int_0^t J(t-\xi) \frac{dF}{d\xi} d\xi \right) \tag{4.44}$$

Where ν and $J(t)$ are the Poisson's ratio and creep compliance of the viscoelastic medium (in this case PS) respectively, and F the driving force for embedding. The driving force can be approximated by assuming that the driving force for embedding results from the normal component of the surface tension of a meniscus layer which forms between the embedding medium and the spherical probe,

$$F = 2\pi R\gamma \sin(\phi) \sin(\theta + \phi) \tag{4.45}$$

where γ is the surface tension of the embedding material, θ is the equilibrium contact angle between the two systems, and γ is the angle formed by the embedding axis and the radial line connecting the sphere center and the meniscus contact line. So in this model the driving force for embedding is identified as surface tension due to the meniscus of a PS wetting layer which covers a portion of the sphere. Hutcheson and McKenna initially raised some concern over this model [98], showing that an alternate model using only the bulk PS properties could also explain the data implying a lack of enhanced surface mobility. An agreement has since been reached on the model discussed above [99].

Qi [24] presents an extensive exploration of the PS surface properties using the gold nanoparticle embedding technique considering: molecular weight dependence for $M_w = 86.8k - 1210.7k$, temperature dependence for $T = 287$ K -378 K (spanning across $T_{g,bulk}$), and sphere size dependence for diameters $D = 16$nm, 19nm, and 30nm. Figure 4.36 plots the apparent nanoparticle height versus time for temperatures ranging from $T_g - 4$ K - $T_g + 8$ K ($T_g \sim 370K$). There are several features to notice in this plot. First we note that for the highest temperature studied there is a single decay down to an embedding depth of ~ 14nm, this process is well described by a single stretched exponential function with stretching exponent $\beta = 0.8$. As the temperature is decreased we see that additional relaxation processes begin to appear with the first decay being well described by a simple exponential ($\beta = 1$), and the second decay requiring a compressed exponential fit ($\beta > 1$). The similarity between different temperatures in the first decay suggests the existence of a dynamically distinct layer at the surface with a depth of ~ 5.5 nm.

Consider next figure 4.37 showing the embedding beahviour for experimental embedding temperatures less than $T_{g,bulk}$. For the three highest temperatures the embedding depth is

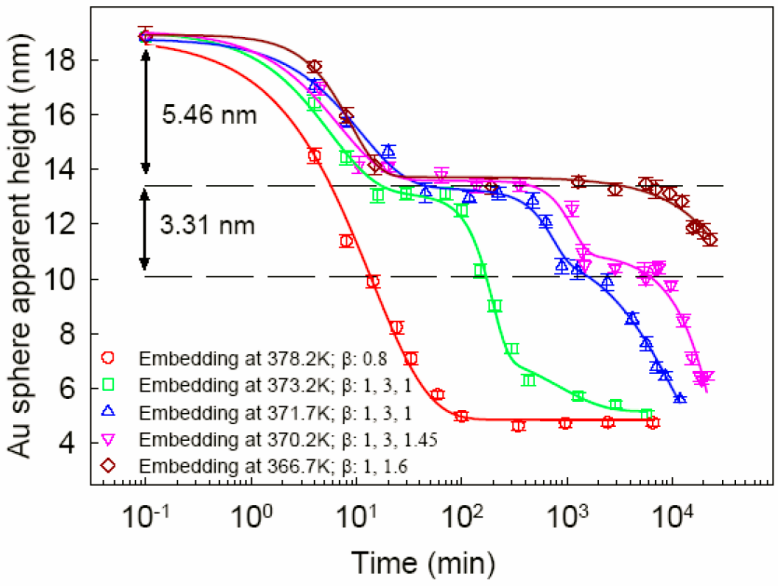

Figure 4.36: Apparent nanoparticle height versus time. Different data sets represent different experimental embedding temperatures as indicated in the lower left. The β values are those used in fitting stretched exponential functions to the different decays. Image reproduced from [24].

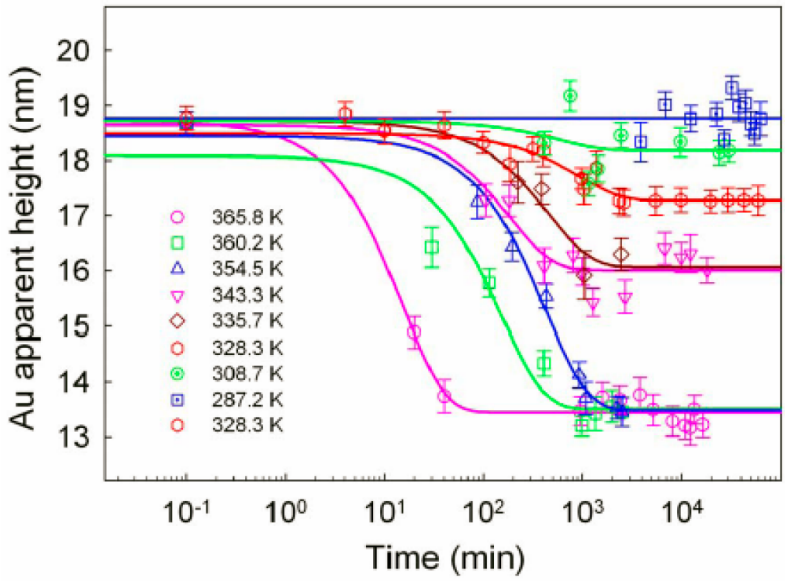

Figure 4.37: Apparent nanoparticle height versus time for temperatures below T_g. Different data sets represent different experimental embedding temperatures as indicated in the lower left. Image reproduced from [24].

consistent with the first decay process observed in figure 4.36 however the time constant for this process now shifts to longer times with decreasing temperature. As temperature is lowered further the final embedding depth decreases, suggesting that the liquid free surface layer is vitrifying. At a temperature of 287.2 K no embedding is observed within the scatter of the data. In figure 4.38 a plot of the temperature dependence of the decay constants from the exponential fits to the embedding data is plotted. This includes the surface process, the sub-surface process (the second decay in high-T plot), and the final decay from the high-T embedding plot. The black curve is the bulk PS α-relaxation behaviour shifted vertically to fit the data. The other lines are linear fits to the associated data. We notice on this plot the relative temperature dependencies of the different decay processes. The slowest process which can be attributed to a relaxation process closer to the bulk of the film is strongly temperature dependent and is found to diverge as the bulk glass transition is passed. In contrast to this the surface process has a very weak temperature dependence, a change in $\sim 70K$ only results in a change of two orders of magnitude in τ.

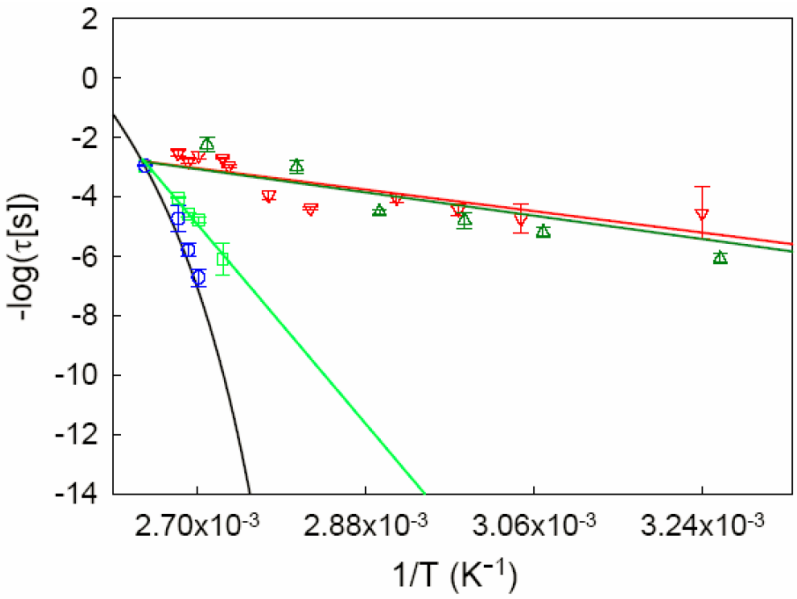

Figure 4.38: Dependence of the observed relaxation times on temperature for the separate decay processes: the final decay in the high T data (blue circles), the second decay in the high T data (bright green squares), and the first decay process from both high and low T data from this study (downwards red triangles), and nanohole relaxation studies [93] (upwards dark green triangles). Image reproduced from [24].

So we see that there is substantial evidence in the literature for the existence T_g reductions in thin polymer films, but that these reductions are not necessarily universal and may depend on the material studied as well as the interaction with an underlying substrate. We have also seen compelling evidence for the existence of enhanced surface mobility in thin polymer films. An important question remains, what is the connection (if any) between these two observations? Depth profiling of the molecular dynamics provided by nanoparticle embedding and fluorescence techniques are promising avenues of research. However the fluorescence techniques are only able to probe dynamics indirectly through T_g and their use for measuring dynamics should be questioned. In figure 4.27 the measured surface T_g using fluorescence techniques was found to increase as the overall film thickness was decreased. This behaviour has not been observed in the dynamical measurements of the free surface by means of surface perturbation relaxation or nanoparticle embedding. In the following chapters we discuss a nanoparticle embedding study on the free surface dynamics of a molecular glass forming system. Such a study is of great interest because the existence of enhanced surface dynamics has thus far only been directly observed in polymeric glass forming systems. It is then quite plausible, having only these previous studies in mind, to think that enhanced surface dynamics may be a direct result of the macromolecular nature of the polymers and not a universal feature of glass formers.

Chapter 5

Experimental Details

5.1 Sample Preparation

5.1.1 Preparation of TNB films

The films studied in this experiment are made of tris-naphthylbenzene (TNB), the molecular structure is shown in figure 5.1. This system has a bulk glass transition temperature of 347 K [100]. The powdered samples used to make the films are synthesized by Traynor and McMahon from the University of Wisconsin-Madison. Mark Ediger's research group at the University of Wisconsin-Madison prepare the films by means of physical vapour deposition. The details of the process are included for completeness. In this process a crucible holding the powdered sample is held in vacuum (2x10^{-8} Torr), below the inverted substrate (see figure 5.2). The crucible is heated and a vapor of the sample is produced, the vapor travels through the vacuum towards the substrate where it is deposited. The rate at which the material is deposited is measured using a quartz crystal microbalance which can accurately weigh the amount of material being deposited onto the substrate. This rate can then be controlled by using the observed rate as feedback to control the heating power of the crucible and thus the rate at which the vapor is produced. A deposition rate of two angstroms per second is used to produce a film with a total thickness of 300 nm. During the deposition process the substrate is held at a temperature of 296 K. The films are then annealed at a temperature of 353 K for 3 hours. Finally they are stored in a freezer before being shipped to our group. Upon receiving the films, they are immediately returned to

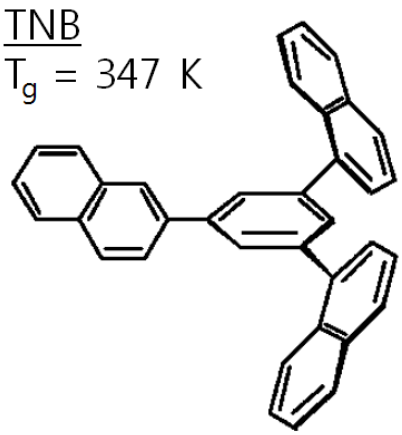

Figure 5.1: Schematic diagram of the molecular structure of 1,3-bis-(1-naphthyl)-5-(2-naphthyl)benzene (Image from [101]).

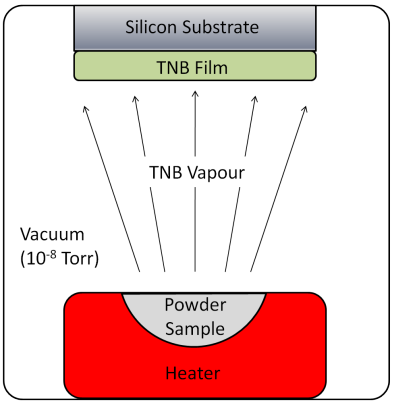

Figure 5.2: Schematic diagram of the vapour deposition process. Upon heating the powdered sample emits vapours which travel through vacuum and deposit on the substrate.

a freezer where they are stored until needed for an experiment. This is done to minimize the amount of sample aging, allowing the films to be kept for several months before use. When beginning an experiment one of these films is first removed from the freezer and allowed to slowly warm to room temperature over the course of an hour. Following this the film is placed into a small oven set at a temperature of 353 K, 7 K above the systems bulk T_g. This step is done for two reasons; it allows the films structure to relax towards an equilibrium state, and when performed for all films used it provides each film with a consistent thermal history. During this annealing process the oven cavity is purged with dry Nitrogen to avoid any potential contamination from an air environment. The sample is left in the oven for 30 minutes before the oven is switched off and the entire system is allowed to slowly cool to room temperature.

5.1.2 Gold Nanoparticle Deposition

The next step in the sample preparation is to deposit the gold nanoparticles onto the surfaces of the films. The gold nanoparticles are produced as an aqueous solution of charge stabilized colloids, their preparation is discussed in the section below. To deposit the nanoparticles we first begin by removing excess dust from three glass pipettes and one small glass vial by spraying with dry nitrogen gas. The film is then placed onto the stage of a spin-coater. Using a separate glass pipette for each component, we prepare in the small glass vial a solution of 10 drops aqueous gold nanoparticle solution and several drops of absolute ethanol. The third glass pipette is then used to briefly mix the solution and place several drops of the solution onto the surface of the film; typically this is done with the film spinning at a rate of approximately 700 RPM.

There are a number of variables which one can adjust in order to tune the density of nanoparticles on the films surface. The ethanol which is added to the solution acts to screen the charged citrate ions on the nanoparticle surfaces this acts to promote accumulation on nanoparticles on the films surface. Typically two drops of ethanol are used but by increasing this number a higher density of nanoparticles can be achieved. It should be noted though that the ethanol also acts to promote aggregation of the nanoparticles so care should be taken to quickly use the solution after the addition of the ethanol. This can be very important when one introduces an adsorption time to the process. Occasionally the nanoparticle/ethanol solution may be placed onto the stationary films surface and after an

adsorption time, removed by spinning the film. Introducing this adsorption time provides the nanoparticles in the solution a longer time to adsorb onto the films surface. Changing the spinning rate of the film will also affect the final density of nanoparticles. Typically speeds between 600 and 1000 RPM are used, below about 600 RPM the liquid drops will remain on the film's surface. The speed can be increased almost indefinitely, however above about 1000 RPM very few nanoparticles are found to adsorb.

The above describes the typical approach used to deposit gold nanoparticles from an aqueous solution onto the surface of a film. However when attempting to deposit gold nanoparticles on a system which one does not have a predetermined recipe for, some trial and error must be done to determine what works. The affinity of the nanoparticles to the films surface is heavily dependent on two factors: the species of film being studied, and the size of the nanoparticles. Smaller nanoparticles have a much stronger ability to adsorb, they can usually be deposited at rather high spinning rates and with no adsorption time. Larger nanoparticles however can be quite difficult to deposit, often a high ratio of ethanol is needed and an adsorption time must be introduced.

5.1.3 Preparation of Gold Colloids

The preparation of the gold nanoparticles used in these experiments is based on the method of Turkevich et al. [102]. The steps of the process are as follows:

1) The required materials are gathered: 250 ml glass Erlenmeyer flask, 50 ml glass beaker, two seven ml glass vials, glass graduated cylinders (10 ml and 50ml), four glass pipettes, citric acid salt ($C_6H_5O_7Na_3 \cdot H_2O$, Sigma-Aldrich C-8532, Molecular Weight = 294.10), gold chloride Hydrate ($HAuCl_4 \cdot H_2O$, Sigma-Aldrich 254169, Molecular Weight = 339.79), and magnetic stir bar. All of the glassware and the magnetic stir bar are washed using hot water and soap, rinsed **thoroughly** with deionized water, and dried.

2) Using an electronic balance with 0.1 mg precision, approximately 50 mL of a 1 mM gold chloride solution is prepared in deionized water. When making this solution it is important not to use metal instruments as the gold salt will react with the metal, glass pipettes are instead used to scoop the salt into a small glass vial. The glass vial is then filled with deionized water and emptied into the Erlenmeyer flask. Care must be taken to ensure that no significant quantity of gold chloride is left behind in the vial. Consequently

the glass vial is flushed several times until no yellowish tinge remains, with each flush the mass of water used is recorded and added to the Erlenmeyer flask. The water added in this process is subtracted from the total amount needed and the remainder is measured out with a graduated cylinder. This solution is then covered with the 50 ml beaker and put onto a hot stage at full heat, the magnetic stirrer is used at a medium speed. The solution is left for approximately 30 minutes until the solution boils.

3) While the gold chloride solution is heating, a citric acid solution is prepared in a glass vial. The amount of citric acid solution used will determine the size of colloids produced. A ratio of 10:1 gold chloride solution to citric acid solution will yield $\sim$ 20 nm spheres, adding more citric acid will give smaller spheres. The concentration of the citric acid solution is one percent by weight. For example; if 50 ml gold chloride solution was made, then for 20 nm spheres a total of 5 ml citric acid solution would be made using 0.05 g citric acid salt in deionized water.

4) When the gold chloride solution boils, the citric acid solution is quickly transferred into the Erlenmeyer flask. The stirring speed is increased to full and the solution is left to heat for another seven minutes. Upon addition of the citric acid the solutions colour will quickly change from yellow, to clear, to grey, and over the next seven minutes will stabilize towards a dark red colour.

5) After the seven minutes have elapsed the hotplate is switched off, the solution is removed from the hotplate, and allowed to cool. When cool the solution is transferred into smaller glass vials and sealed for later use. When stored in sealed vials the solution can be kept and used for around 3 months. Around this time the nanoparticles will begin to aggregate. Aggregation can be identified by a dark cloud in the bottom of the vials as the aggregated nanoparticles begin to precipitate out of solution.

The nanoparticles produced using this technique are charge stabilized against aggregation. The stabilization is provided by a citrate anion layer that covers the nanoparticle surface, coulomb repulsion of the citrate ions prevents nanoparticle aggregation. This recipe can be used to make a range of nanoparticle sizes simply by changing the ratio of gold chloride solution to citric acid solution. A similar product is commercially available from Ted Pella Inc., these commercial solutions have a narrower distribution of nanoparticle sizes (10% of average sphere size) when compared to our solutions ($\sim \pm$ 3 nm for 20 nm spheres up to $\sim \pm$ 10 nm for larger spheres, as measured by AFM). However the

nanoparticle solutions we produce are about 10x more concentrated than the commercial solutions, this is an important consideration when it comes to depositing the nanoparticles onto a films surface.

5.2 Atomic Force Microscopy

Atomic force microscopy developed in the mid-1980's [103] is an experimental technique belonging to the larger class of techniques known as scanning probe microscopy. All scanning probe microscopy techniques involve raster-scanning a sharp probe over the surface of a sample. Interactions between the probe and the surface provide information about the surface with nanometer resolution in lateral directions and, with proper care, sub-nanometer resolution perpendicular to the surface. As the name suggests, atomic force microscopy make use of the atomic force interactions between the probe and sample. This is in contrast to other SPM techniques such as scanning tunneling microscopy which uses tunneling of electrons between probe and sample or near-field scanning optical microscopy which relies on the interaction between the sample and an evanescent wave created by a light source which is brought very close to the sample surface. In AFM the probe used is a long thin Si cantilever (typically hundreds of microns in length and tens of microns in width) with a sharp tip attached to one end of it. The shape of the AFM tip can vary; typically it is pyramidal with a radius of curvature ≤ 10 nm. Sharper tips can be formed by using a conical tip shape or by using carbon nanotubes as the tip, however these tips are much less resistant to wear.

A schematic illustration of an AFM setup is shown in figure 5.3. The basic operation of the AFM is that a laser beam is focused onto the backside of the cantilever, and the reflected beam is directed onto the center of a quadrant photodiode. The position of the beam on the photodiode can be used to detect deflections of the cantilever. The cantilever position is precisely controlled using piezoelectric scanners allowing motion in the x, y, and z directions.

There are three standard modes of AFM operation; contact, non-contact, and intermittent contact. In our studies we use intermittent contact but for completeness a brief description of contact and non-contact modes is provided. Contact mode is perhaps the simplest to explain: the tip is lowered close enough to the sample surface that it begins

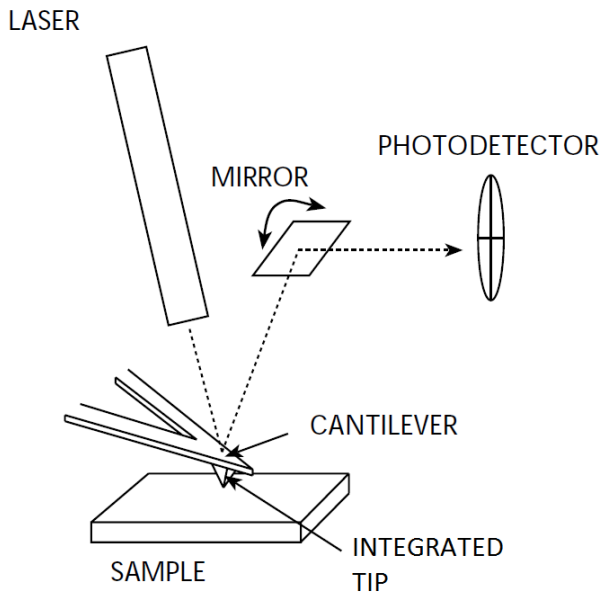

Figure 5.3: Schematic illustrating the basic operation of the atomic force microscope. A laser reflected off of the backside of the cantilever is steered via a mirror onto the quadrant photodetector. Deflection of the cantilever can be detected by a change in the position of the reflected beam on the detector. Not shown here are the piezoelectric scanners which the cantilever is mounted upon. These piezo scanners control the position of the tip in the x,y, and z directions. Image from [104].

to experience the hard-core repulsion forces from the surface. This results in a deflection of the cantilever. While scanning, the system will maintain a certain deflection of the cantilever by monitoring the position of the laser on the photodetector. When the probe encounters a surface protrusion it will deflect the cantilever further and the system will respond by retracting the z-piezo. By tracking the z-piezo height at all positions the surface is mapped out. The main downfall of contact mode operation is that the large forces involved due to the hard-core repulsion cause significant damage to both tip and sample. For this reason contact mode is ill-suited to studying soft materials. Non-contact mode operation is a better candidate for soft materials as the forces involved are much smaller, however it does have its own limitations. In non-contact mode operation the cantilever is driven near its resonance frequency to induce oscillations. As the tip and cantilever are lowered towards the surface the presence of the surface will damped the cantilevers oscillations. The amount that the surface dampens the oscillations is controlled by the setpoint. The setpoint is given as a percentage and it represents the percentage of the free air oscillation amplitude that the system will maintain. Typically this value is set somewhere around 50%, so when beginning a scan the system will lower the tip until the oscillation amplitude reaches 50% of it's original value. When scanning, a surface feature will alter the amount of dampening, the system will respond by raising or lowering the z-piezo in order to maintain the setpoint. One of the major drawbacks of non-contact mode operation is that it is possible for the probe to become attached to the surface. The oscillations of the cantilever are quite small (on the order of nm), making the restoring force quite small, so if the probe encounters a feature such as a patch of liquid it is easy for the probe to get stuck in the liquid. A good compromise between contact and non-contact modes is intermittent-contact. The basic operating principle is identical to non-contact mode, the cantilever is oscillated near it's resonance frequency and the set point is maintained during scanning. The difference is that intermittent-contact mode drives the cantilever with a much larger amplitude (on the order of 10-100's of nm) such that at it's lowest point the probe will actually be into the repulsive force regime. This larger amplitude ensures that the restoring force for the cantilever is large enough to overcome an adhesive forces between tip and sample. Furthermore since contact is only made periodically with the surface, the damage done to tip and sample is much less than in contact mode. Figure 5.4 illustrates the different regimes of operation with respect to the tip-sample force versus distance curve.

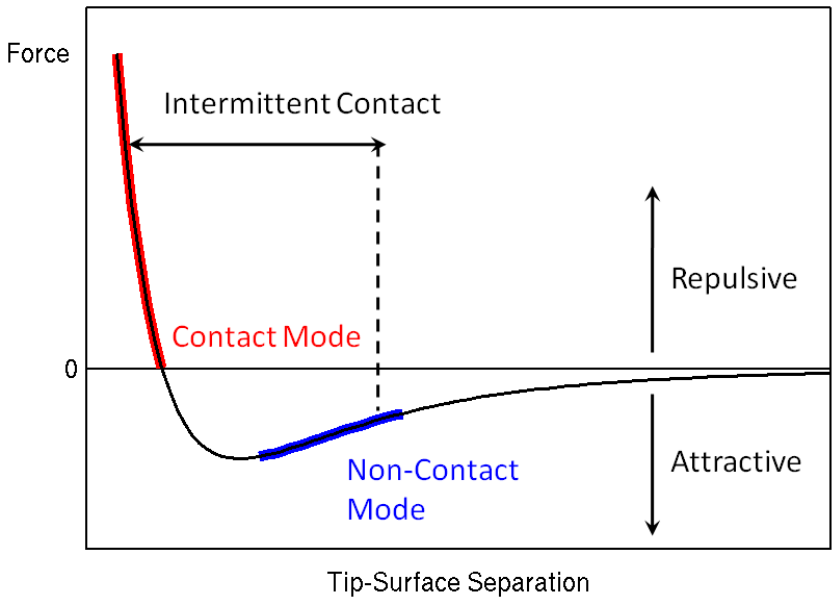

Figure 5.4: An illustrative plot of force versus tip-surface separation. Contact mode is always performed in the repulsive regime where hard-core repulsion forces are exerted. Non-contact mode takes place further from the sample in the attractive regime where the forces are due primarily to Van-Der-Waals forces. Intermittent contact mode straddles both of these regimes with one oscillation of the cantilever taking it between repulsive and attractive forces.

In order to achieve the best image quality, there is a long list of system parameters that one must be familiar with and fine tune for each image: drive amplitude, input gain, setpoint, scan rate, scan range, scan resolution (number of lines), and the PID parameters. The PID parameters, standing for proportional-integral-derivate are used in a feedback system to determine how the system will respond to the changes in deflection/oscillation amplitude that are encountered. These parameters are very important and improper setting for these will usually result in poor quality images. Determining the optimal settings for all of these parameters is not a simple task, as a result the acquisition of high quality AFM images is often referred to be somewhat of an art. One further consideration that should not be overlooked is the surfaces tilt with respect to the AFM's xy-plane, this tilt should be minimized prior to performing scans.

5.3 Isothermal Nanoparticle Embedding Procedure

Having discussed all of the experimental techniques used throughout the nanoparticle embedding studies we can now explain how a typical embedding study proceeds. Naturally the first step is sample preparation, this is performed as discussed above in section 5.1. Nanoparticle deposition was performed using a 10:1 ratio of aqueous gold nanoparticle solution to ethanol. Two drops of this mixture were dropped onto the surface of the film while spinning at 700 RPM. Once the nanoparticles have been deposited the film is brought to the AFM (Thermomicroscopes Explorer) and mounted onto an AFM stage with built in hotstage. The stage is custom built to replicate those commercially available from Linkam Scientific Instruments, as such it is compatible with the associated temperature controllers. The wafer is securely mounted to the heating element by a thin carbon sticker to ensure good thermal contact. Initially a relatively large AFM scan (typically 10x10 μm) is performed. From this scan a smaller 3x3 μm area is selected to be used for the remainder of the experiment. In choosing this smaller region one looks for an area containing approximately 5 nanoparticles with each nanoparticle having at least 500 nm between it and any other nanoparticle. This spacing is required to ensure that the presence of one nanoparticle does not affect the progress of another nanoparticle. Figure 5.5 shows an initial 10x10 μm AFM scan area and indicates the 3x3 μm area selected for that experiment. Once this area has been selected several scans will be taken at a resolution of 6 nm per data point to ensure that an accurate image of the nanoparticles has been formed. To avoid potential damage

to the AFM piezos upon heating, the AFM head must be retracted from the sample surface before heating. Alternatively one could simply lift the AFM head off the stage but it was decided early in the experimental studies that for a given embedding experiment the progress of a *specific set of nanoparticles* should be tracked throughout and lifting the AFM head makes relocating the chosen region a very difficult and time consuming task. The heating process is controlled using a Linkam TP93 controller, the maximum heating rate of 90 K/min is used to minimize the time spent at intermediate temperatures. Once the sample reaches the desired temperature it is held for 2 minutes before the heater is switched off and the sample is left to naturally cool to room temperature. The previously chosen region is again located with a large scan and several 3x3 μm scans are acquired. The rest of the experiment is performed by repeating these heating, cooling, and imaging steps however with each repetition the sample is held at the annealing temperature for an exponentially increasing amount of time. For many of the higher temperatures studied, the end of the experiment is dictated by surface crystallization. Crystalline regions will nucleate randomly on the surface, once a crystalline boundary begins to approach the area being imaged the experiment will be stopped.

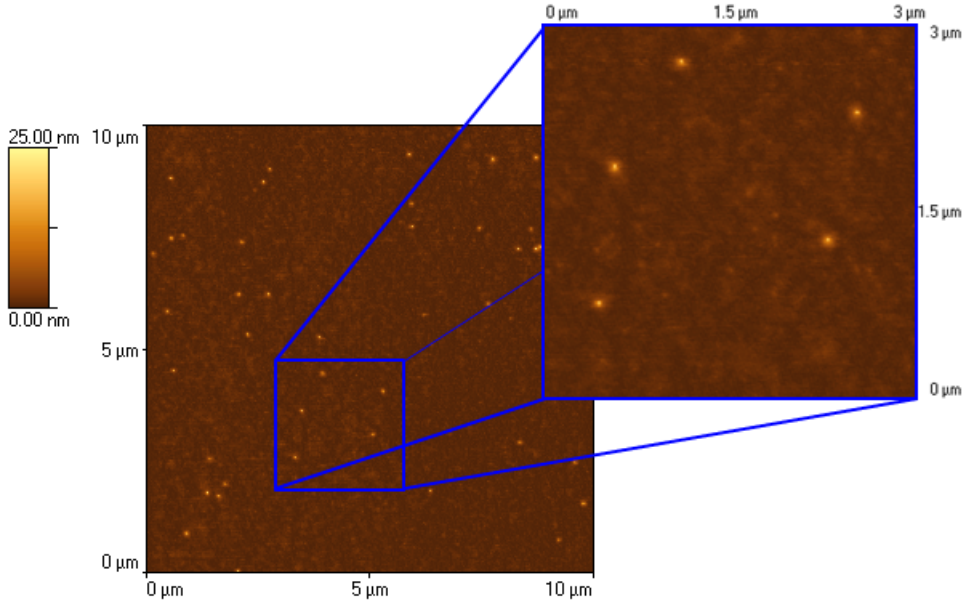

Figure 5.5: From the initial 10x10 μm scan, a smaller 3x3 μm area is selected and a higher resolution image taken of that area. The 3x3 μm area is chosen to have approximately 5 spheres with at least 500 nm between spheres.

Chapter 6

Results

The isothermal nanoparticle embedding experiments outlined in section 5.3 have been used to study the free surface properties of thin films of tris-naphthylbenzene. The experiments were performed for temperatures 315-345 K which are all below the glass transition temperature, T_g = 347 K. Through these experiments we have determined that TNB films in the glassy state display heterogeneous dynamics. We find that there is a surface relaxation process present at all of the temperatures studied, and that this surface process exhibits a weak dependence on temperature. Close to T_g a second relaxation process is observed which occurs on a much longer timescale than the surface process and has a very strong temperature dependence. We attribute this second process to the relaxation of bulk material beneath the sphere. Figure 6.1 shows a representative set of AFM images of a particular nanoparticle over the course of an experiment at T = T_g - 9 K. The surface process quickly forms a buildup of material around the sphere which is subsequently stable for thousands of minutes before the nanoparticle begins to embed into the film.

Section 6.1 discusses the surface process and section 6.2 discusses the slower bulk relaxation process. The bulk of these experiments are done using nanoparticles with a diameter of approximately 20 nm, section 6.3 presents results which look at a possible sphere size dependence of the surface process. Finally section 6.4 makes an estimate of the depth of the mobile surface layer.

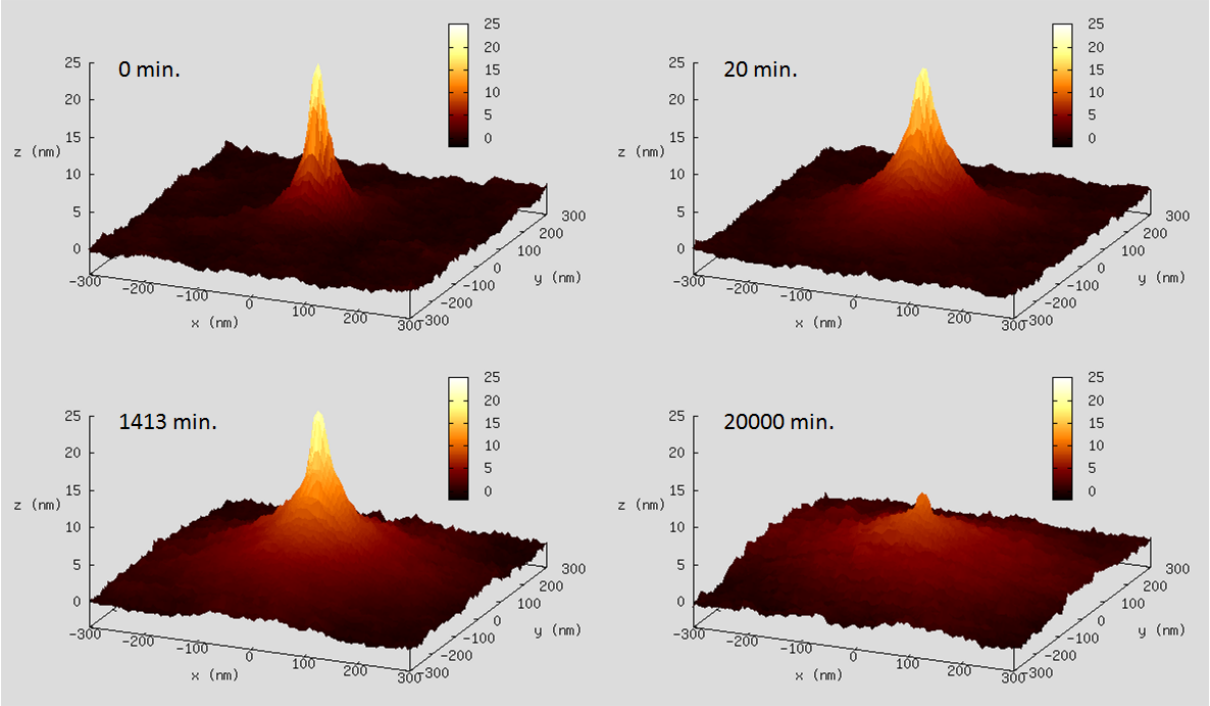

Figure 6.1: A representative set of 3D images showing the progress of a particular nanoparticle over the course of a 20000 minute experiment at T = T_g - 9 K. The surface process forms a buildup of material surrounding the nanoparticle, this forms within the first 20 minutes and is stable for the next 1400 minutes after which point embedding occurs.

6.1 Temperature Dependence of TNB Free Surface Dynamics

6.1.1 Initial Observations of a Surface Relaxation Process

Our original motivation behind these studies was to make a comparison between the free surface properties of molecular glasses in thin film geometries with the wealth of information regarding the free surface properties of thin polymer films in the glassy state [95, 96, 97, 24, 23, 94, 93, 91, 92, 105, 86, 85, 84, 87, 88, 89, 90, 98, 99]. The main purpose was to determine if the free surface of a molecular liquid below its bulk glass transition temperature would show evidence for a mobile free surface region. Our results show that the free surface of the molecular glass forming system TNB displays an enhanced mobility relative to the bulk at temperatures well below the bulk T_g. However due to the differences in molecular structure, TNB and polymer systems exhibit strikingly different stress relaxation processes in response to nanoparticles at the free surface. The AFM images shown in figure 6.2 show a grouping of nanoparticles on the surface of a TNB film prior to heating and after 5 minutes of heating at a temperature of 333 K (T_g - 14 K). These images are representative of what has been observed for all of the temperatures studied. The TNB material on the free surface is being drawn towards the nanoparticles and creating a buildup of material surrounding the spheres.

The explanation of this nanoparticle engulfment effect, illustrated in figure 6.3, is quite simple and goes as follows. Due to the favourable work of adhesion between the liquid TNB molecules and the gold sphere, the TNB first wets the sphere. In the initial stages this results in a sharp curvature in the TNB profile. Due to the surface tension of the liquid TNB, this sharp curvature produces a large stress in the film which can be relaxed by smoothing out this curvature. Upon heating to temperatures which are still below T_g the mobility at the surface is sufficient to allow diffusion of molecules towards the sphere. This results in a buildup of material surrounding the sphere which reduces the curvature of the film in the vicinity of the sphere. This process has not been observed in the nanoparticle embedding studies performed on Polystyrene. In those studies the lowest molecular weight considered was 86800 g/mol which is well above the entanglement molecular weight of about 20000 g/mol. Furthermore the radius of gyration of a chain of that molecular weight is roughly 8 nm, larger than the estimated depth of the region of

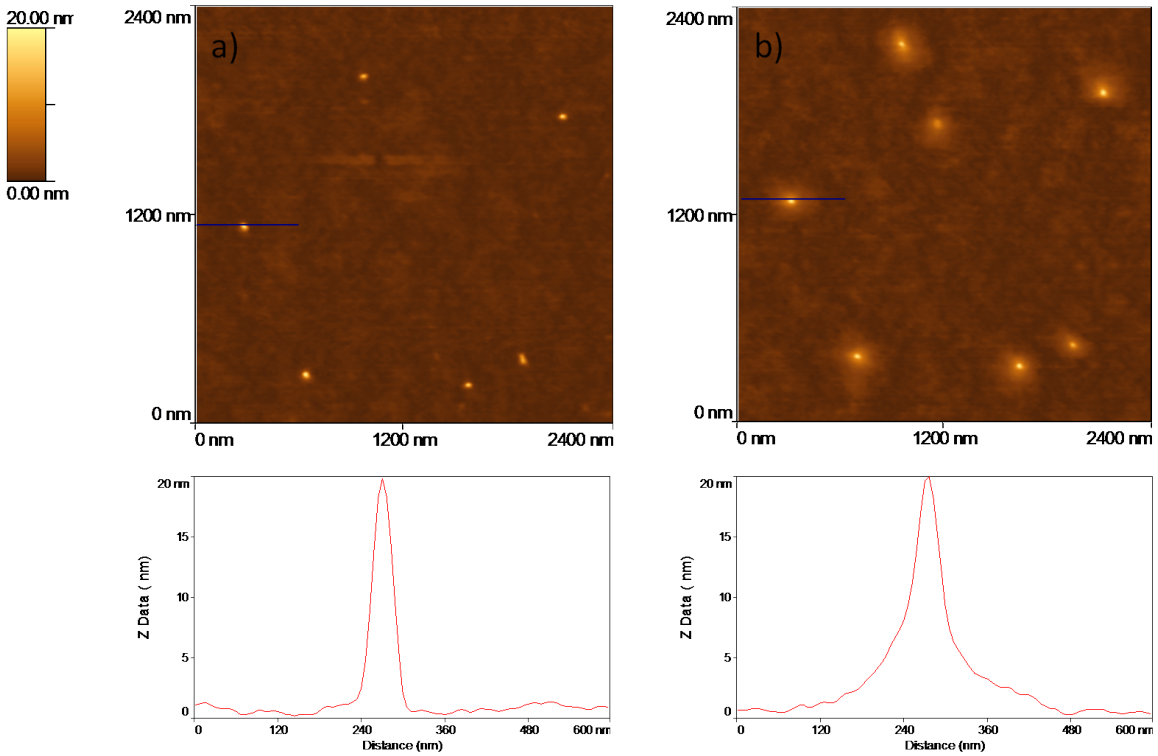

Figure 6.2: A set of AFM scans showing a grouping of nanoparticles on the surface of a TNB film. a) Prior to heating. b) After 5 minutes of heating at T = 333 K (T_g - 14 K). Below each image is a line profile taken across the nanoparticle peak as indicated by the blue line in the image.

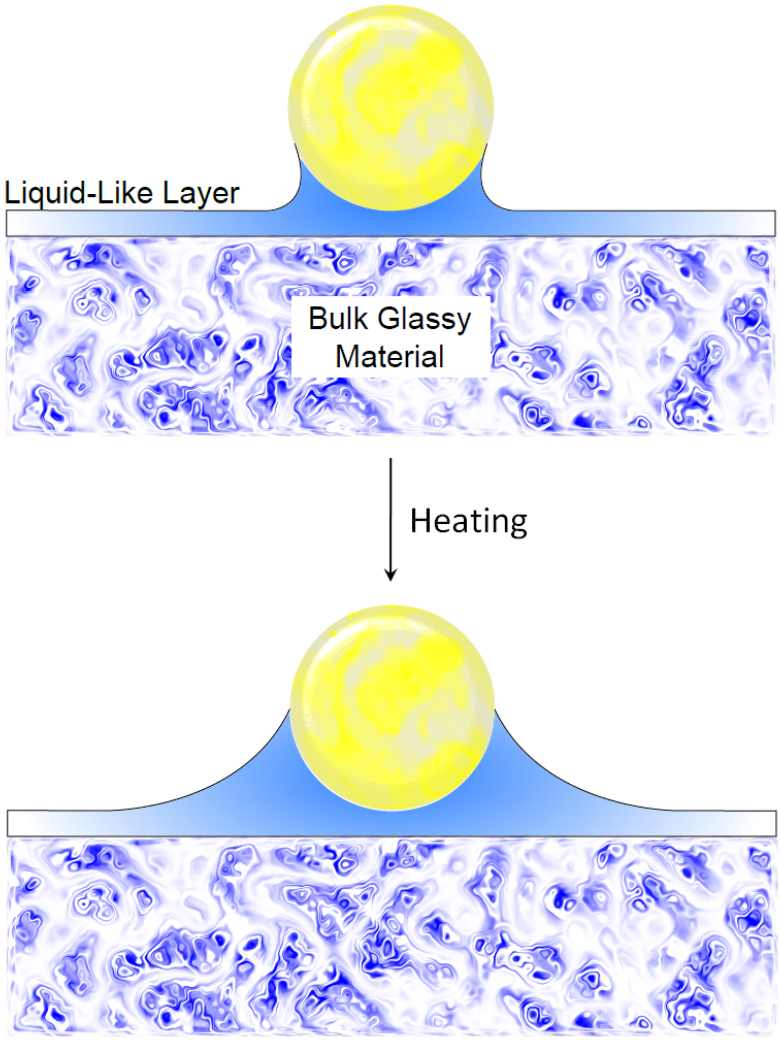

Figure 6.3: Initially TNB material in the liquid-like free surface layer wets the surface of the gold nanoparticle. The resulting curvature produces a stress in the film. Upon heating, TNB material can flow across the surface towards the sphere and even out that curvature, relaxing the stress.

enhanced mobility. Combining these facts one does not expect transport of entire polymers chains to be possible in the surface region of glassy films. Since diffusion of entire chains is required to produce a buildup of material around the sphere it is then not a surprising result that this process is not observed in those studies. A comparison of the results of this study to studies on polymer films is discussed in more detail in section 6.5.

6.1.2 Quantitative Analysis of the Surface Process

As mentioned above the nanoparticle engulfment effect had not been previously observed. It is not immediately obvious how one should attempt to quantify this process. In the discussion that follows we have made use of two complementary analyses to quantify the nanoparticle engulfment. The different analyses are shown to probe different aspects of the engulfment process which have different temperature dependencies.

Rim Height Analysis

The first analysis that we've considered to quantify the engulfment process tracks the TNB rim height as a function of time. Figure 6.4 illustrates how this value is determined from the data. A line profile is taken across the nanoparticle peak. Two values must be read off of this profile. First one needs to measure the overall nanoparticle height, this is easily done taking the maximum value of the profile. The second value needed is representative of where the TNB material makes contact with the sphere, the TNB contact height. This point is found by looking for a marked change in the slope of the profile. We define the rim height as the overall nanoparticle height minus the TNB contact height. In order to account for small variations in nanoparticle heights between nanoparticles we normalize to the nanoparticle height as determine prior to annealing, h_o. One drawback to this method is that the determination of the TNB contact height is not always as clear as shown in figure 6.4, in those cases it is often best to omit that image from the results. Furthermore the details in the immediate vicinity of the nanoparticle depend on the convolution of the AFM probe with the sphere, as such care must be taken to ensure that only sharp AFM probes are used.

Figure 6.5 represents the results of this analysis for all of the temperatures studied. Each data set represents the behaviour of a single nanoparticle, each data point is an

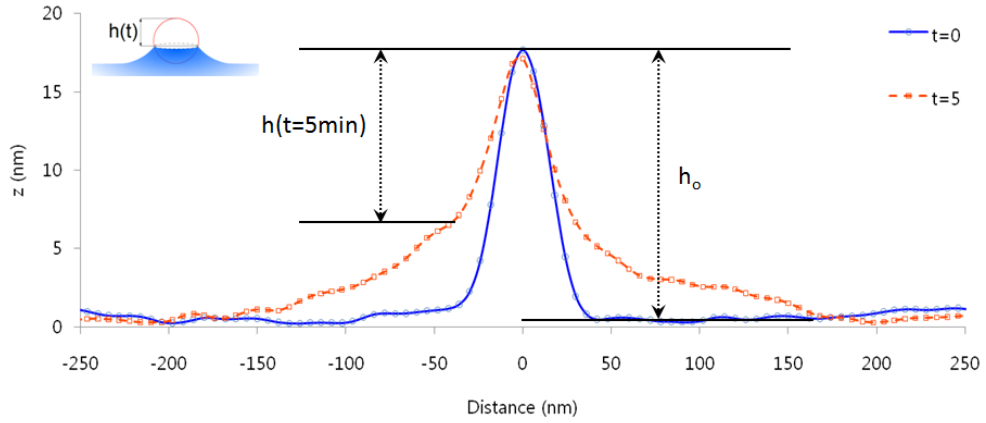

Figure 6.4: Illustrating the determination of the rim height. The rim height is found by measuring the distance between the nanoparticle peak height and the height at which the TNB material contacts the sphere. This second height is identified by a marked change in the slope of the profile.

average over multiple AFM scans and profile directions. For all of these temperatures, ranging from $T_g - 2$ K to $T_g - 32$ K, there is a rapid decay towards a plateau value of ~ 0.7 implying that the TNB buildup is engulfing the bottom 30% of the nanoparticle. Furthermore by looking at this plot there is no discernible temperature dependence to this process. However one should expect that there would be a temperature dependence to the surface mobility, as we will see with our second analysis this appears to be the case, but the rim height analysis is not overly sensitive to it.

Volume Analysis

Our second analysis of the surface process is done by tracking the volume of material as a function of time. In this analysis a series of images of a specific nanoparticle are first averaged together. The data points making up the image are then separated into bins based on their radial distance from the nanoparticle peak position, essentially creating a radially averaged histogram of the data. The total volume of material that went into each bin is calculated by summing together the z-values of all of the data points in a particular bin and multiplying by the area of each data point. In figure 6.6 are six plots, each plot represents the volume of material within a certain annulus section versus time. The first image is the

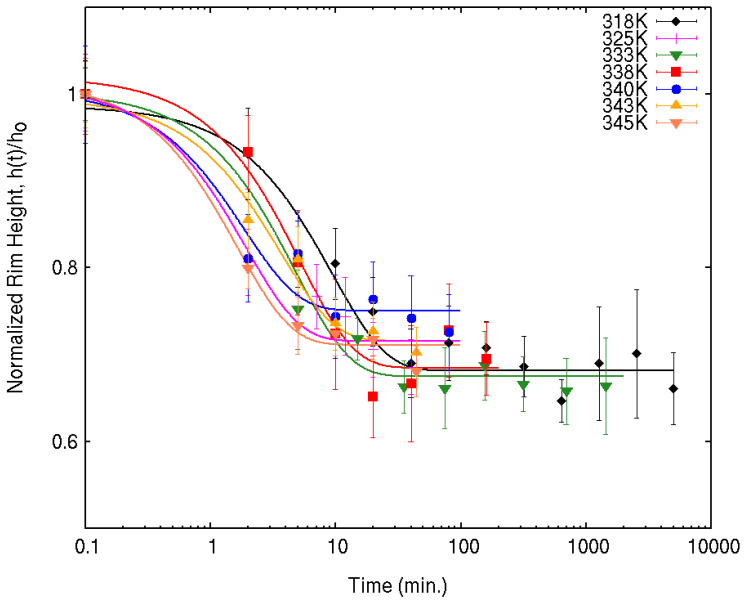

Figure 6.5: Plot of the normalized rim height versus time for the seven temperatures studied. There are two important points to notice in this graph. 1) For all temperatures there is a decay towards a plateau value of ~ 0.7. 2) There is no discernible temperature dependence to this decay. Error bars are determined by the standard deviation of the individual measurements ($\sim$ 10 measurements in most cases).

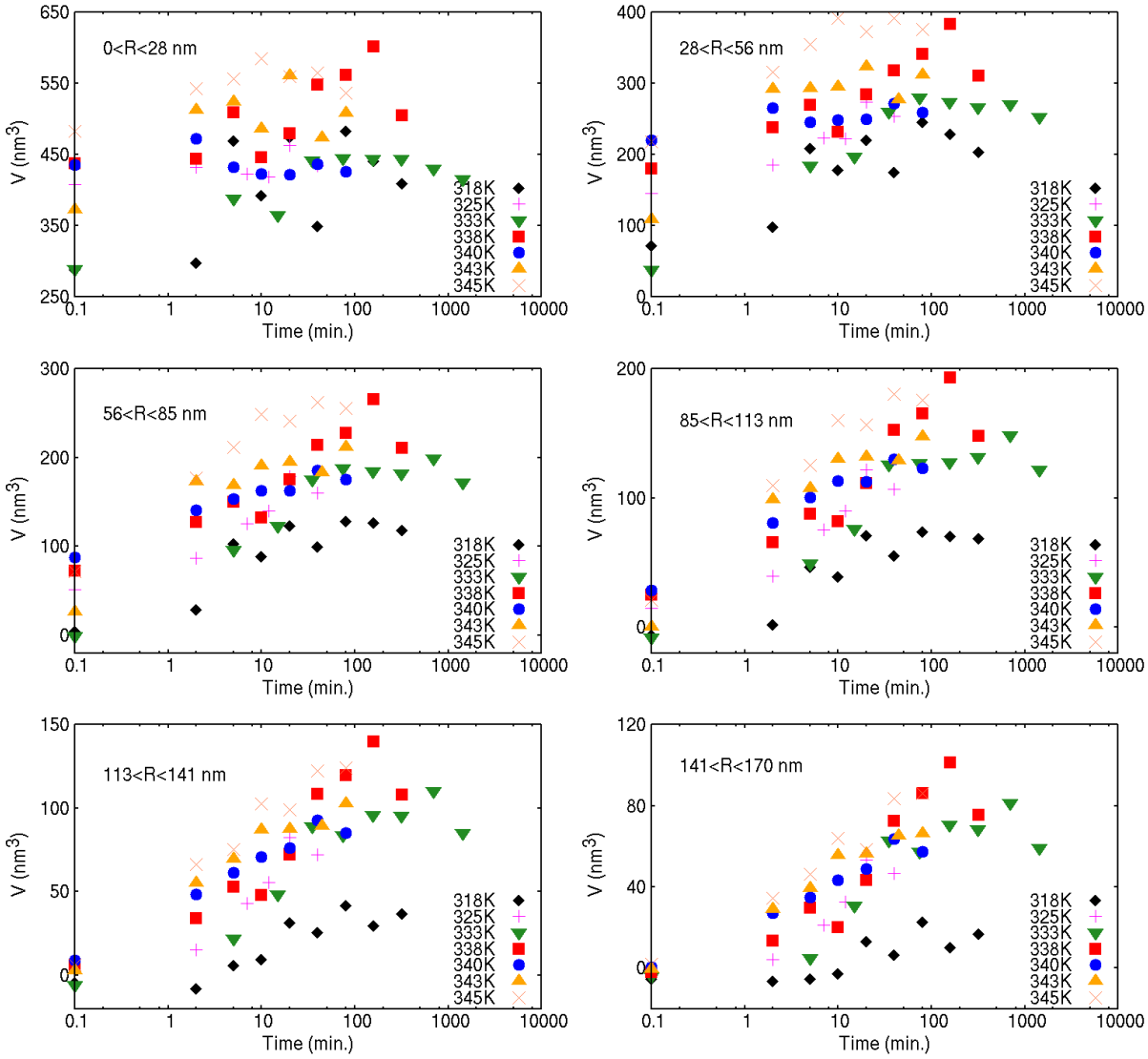

Figure 6.6: A set of plots of volume versus time. Each plot represents the volume of a different annulus section, as indicated on the plots. The different data sets in each plot represent different temperatures.

material from $0 < R < 28$ nm, the second for $28 < R < 56$ nm, etc., up to 170 nm. In the first few images we see that there is no discernible temperature dependence. However when we move out towards the final few images we see that the higher temperature data points are consistently higher than the lower temperature points. So at the higher temperatures more material is able to flow in towards the spheres. Further out from the sphere where the curvature is less the driving force for bringing in material is not as strong, this is likely why we can observe the weak temperature dependence; as the driving force decreases, at some point it will be too weak to draw material at the lower temperatures, but the higher temperatures will still be mobile enough to respond to the weak driving force.

6.2 Temperature Dependence of the Bulk Relaxation Process

The results above clearly indicate the existence of a surface relaxation process below T_g which is much faster than would be expected for a bulk glassy system. For the higher temperatures studied we have also observed a second relaxation process, an embedding of the nanoparticles. This second process is attributed to a relaxation of material beneath the sphere deeper into the bulk of the film. With the correct choice of temperature the timescale of embedding becomes completely separated from the timescale of the surface relaxation process. Figure 6.7 shows two AFM images of a grouping of nanoparticles before annealing and following 20000 min of annealing at T = 338 K ($T_g - 9$ K). In the second image we notice two things: first the buildup of material from the engulfment process is clearly visible, and second the apparent nanoparticle height is much smaller than in the first image. We have again considered two ways to analyze the results; the same rim height analysis used for the surface process, and a straightforward embedding analysis tracking the apparent nanoparticle height as a function of time.

Rim Height Analysis Of Embedding Process

Using the rim height analysis we can represent both processes with one measure on a single plot. Figure 6.8 presents the results of this analysis. We see the initial decay from the engulfment process and for the four highest temperatures studied there is a second

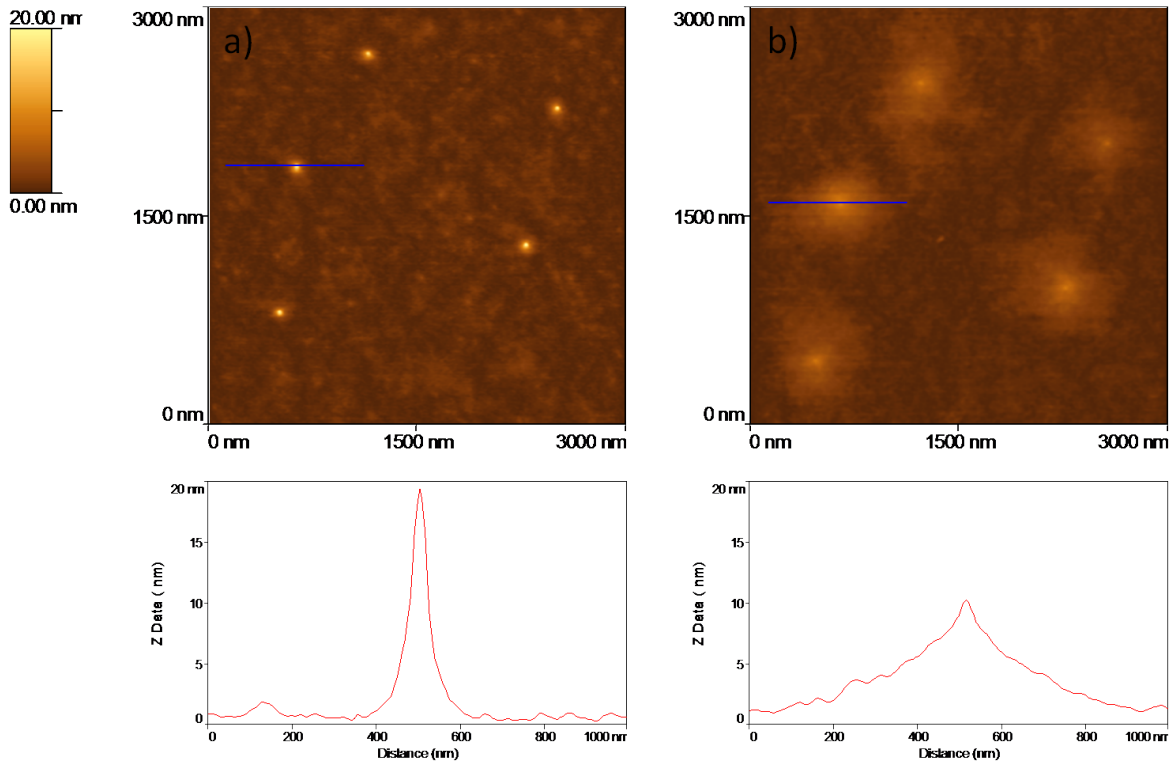

Figure 6.7: A set of AFM scans showing a grouping of nanoparticles a) Prior to annealing b) Following 20000 min of annealing at T = 338 K. The line profiles are taken at the positions indicated by the blue lines.

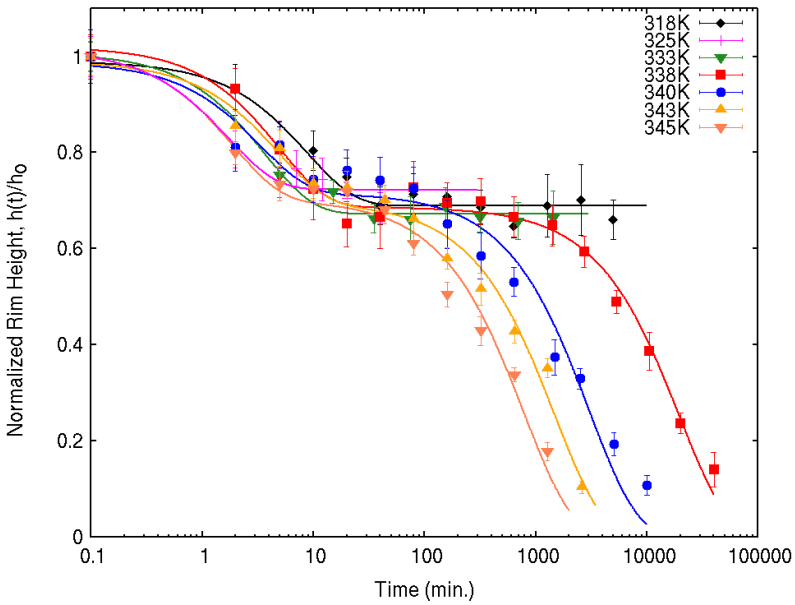

Figure 6.8: Normalized rim height versus time presented for the full length of each experiment. For the higher temperatures there is a second decay as the nanoparticles embed into the film. Error bars determined from standard deviations.

decay attributed to the embedding of the spheres into the film. For these temperatures the timescale of the embedding process is entirely separated from the surface process. This separation of timescales makes it clear that there are two separate relaxation processes occurring, this indicates the presence of heterogeneous dynamics in these films. There is the short timescale surface process which has a very weak temperature dependence, and there is a long timescale process owing to relaxation of material in the bulk of the film which has a strong temperature dependence. For example the 338 K and 340 K experiments are separated by only 2 K but there is almost an order of magnitude difference in the timescale of the decay.

Nanoparticle Height Analysis

It is not immediately obvious that the rim height should be a reliable measure of the nanoparticle embedding process. As a check we can also analyze the embedding process by tracking the apparent nanoparticle peak height as a function of time. Figure 6.9 plots the normalized nanoparticle height as a function of time for all temperatures. Throughout

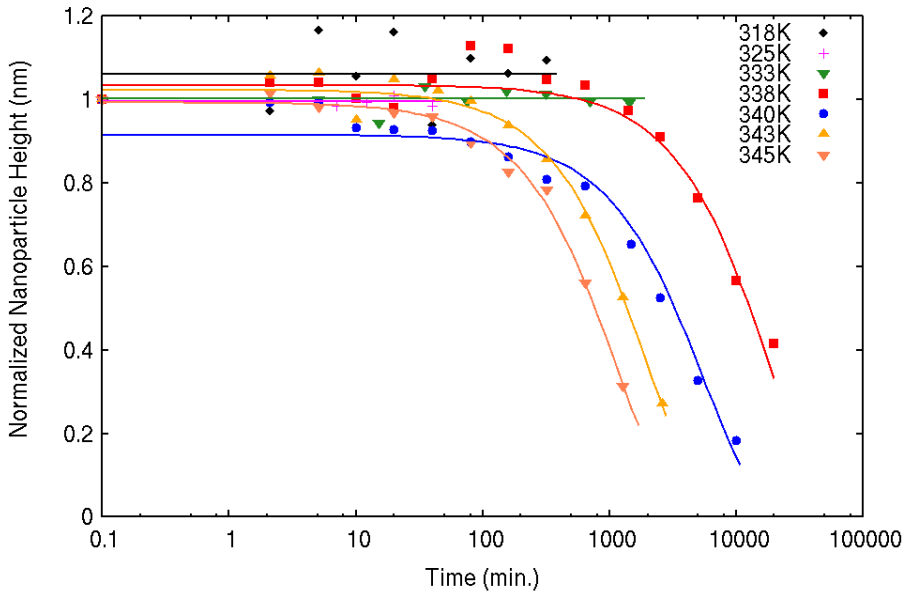

Figure 6.9: Plot of the normalized nanoparticle height versus time for the full length of each experiment. For the lower temperatures the nanoparticle heights are a constant within the time of the experiment. For the higher temperatures the peak height drops as the nanoparticle embeds. Error bars as determined from standard deviations are smaller than the point sizes.

the nanoparticle engulfment process the apparent nanoparticle heights stay constant for all temperatures, for the higher temperature curves the nanoparticle height decreases as the nanoparticle embeds. We can compare the results of this analysis to the rim height analysis by comparing the observed relaxation times as determined by an exponential fit to the data, discussed in the next section.

6.2.1 Temperature Dependence of Relaxation Times

In figures 6.8 and 6.9 exponential fits have been applied to the data. From these exponential fits we can extract out relaxation times, τ_s and τ_b, for the surface and bulk processes respectively. In figure 6.10 we plot $-\log(\tau)$ versus inverse temperature for both processes. The fit to the bulk time constants is made by vertically shifting the Vogel-Tammann-Fulcher (VTF) equation,

$$-\log(\tau) = A - \frac{B}{T - T_\infty} \tag{6.1}$$

Plazek et al. [106] fit the temperature dependence of the bulk TNB viscosity to the VTF equation. The temperature dependence of the relaxation time should be the same as the temperature dependence of the viscosity, so we can use the values of $B = 4100$ K and $T_\infty = 200$ K found by Plazek et al. for the temperature dependence and vertically shift the curve by fitting the constant A to account for the scaling between relaxation times and viscosity. This form fits the data quite well suggesting that the nanoparticle embedding process is governed by a bulk-like relaxation of the material beneath the sphere. The vertical line on this plot indicates the extrapolated intersection temperature T_{int} of the two processes, it is found at a temperature of $\sim T_g + 12$ K . One possible interpretation of T_{int} is that it represents the temperature which separates homogeneous and heterogeneous dynamics, with heterogeneous dynamics only existing below T_{int}.

Note the agreement on this plot between the bulk relaxation times as determined from the rim height and nanoparticle height analyses. This indicates that the rim height analysis is an accurate measure of the embedding process.

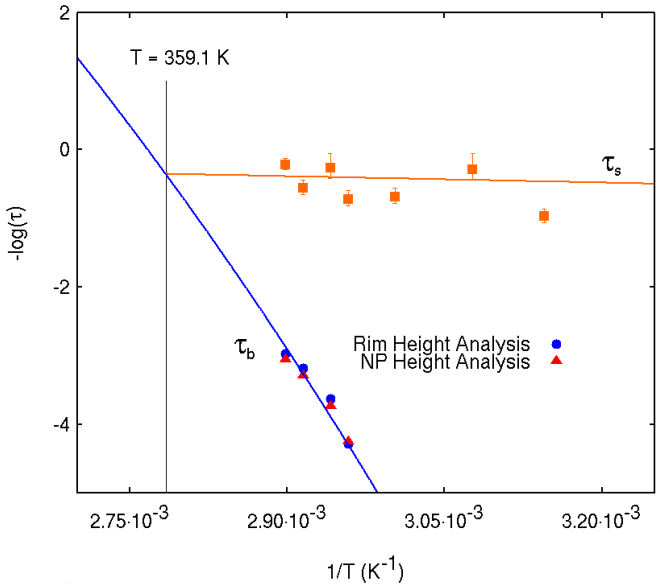

Figure 6.10: A plot of -log(τ) versus inverse temperature for the surface and bulk processes. The relaxation times of the surface shown by the orange squares are fitted to a linear function on this plot. The bulk relaxation times are fit to a vertically shifted VTF equation with parameters taken from Plazek et al. [106]. For the slow process, time constants are found through the rim height analysis (blue circles) and the apparent nanoparticle height analysis (red triangles). Error bars are determined from the standard error of the exponential fits to the decays shown in figure 6.8.

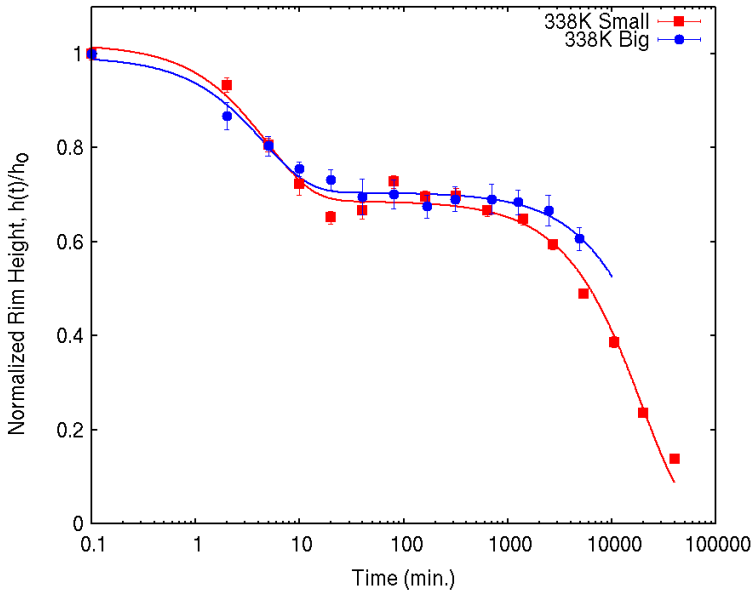

Figure 6.11: Normalized rim height versus time for the small spheres ($\sim$ 20 nm, red squares) and the large spheres ($\sim$ 40 nm, blue circles).

6.3 Nanoparticle Size Dependence

In order to elucidate the nature of the driving force for nanoparticle engulfment we have also studied the possibility of a sphere size dependence. We have performed an experiment using spheres twice the size used in the original studies at a temperature of 338 K. In figure 6.11 we plot the normalized rim height versus time for the large and small spheres at T = 338 K. From this plot we see that the engulfment process, as probed by the rim height analysis, shows no dependence on the nanoparticle size. However if we consider the amount of material in the buildup further from the sphere, a size dependence is found. Figure 6.12 shows a series of line profiles taken across the nanoparticle peaks. The first plot shows profiles taken across the $\sim$ 20 nm sphere at different stages of annealing, and similarly the second plot shows a series of profiles for the $\sim$ 40 nm sphere. For the smaller nanoparticle we see that after 20 min. the profiles are quite stable and all later time profiles lie very close to each other. The profiles for the larger nanoparticles take a longer time to stabilize indicating that the surface process is slower for the larger spheres. This indicates that the buildup of material is dependent on the nanoparticle size. As molecules diffuse towards the

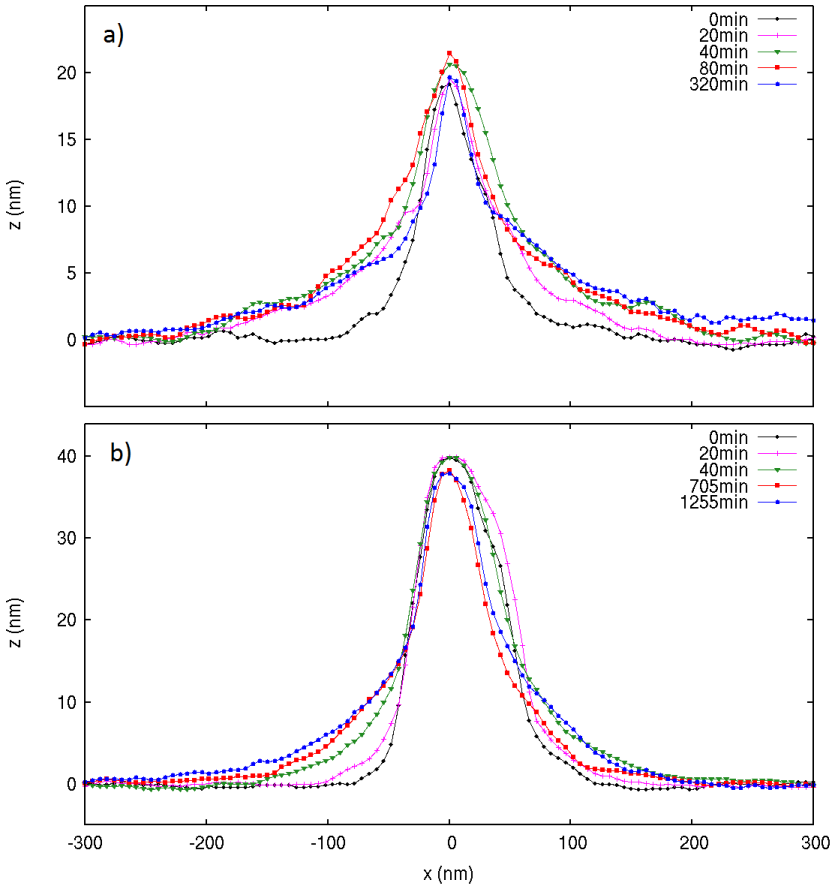

Figure 6.12: Line profiles taken across nanoparticle peak, a) $\sim$ 20 nm spheres, b) $\sim$ 40 nm spheres. The different curves show the profile at different stages of annealing.

nanoparticle they reach the area of curvature, and since it lowers the system's free energy, molecules have a high probability of accumulating around the nanoparticle, smoothing out the curvature. However the probability that a molecule will remain in the buildup is dependent on the curvature, a higher curvature increases the probability of accumulation so material does not accumulate as quickly for the larger spheres. We can make a rough estimate of how much slower the buildup is for the larger spheres by considering the volume of material in the buildup. The volume of material surrounding the small spheres at a temperature of 338 K levels off somewhere around 400000 nm^3, and it does so on a timescale of roughly 100 minutes. After 1000 minutes of annealing for the large spheres the buildup is still increasing in volume, however the volume at this time approaches the 400000 nm^3 found for the small spheres. So the accumulation of material seems to be about 10 times slower for the 40 nm sphere. Although we have only observed the initial stages of the embedding process for the larger sphere, we can see in figure 6.11 that the large spheres begin to embed at a later time than the small spheres. This is the expected result since embedding of a larger sphere requires relaxation of a larger volume of underlying material. A similar observation was found for the nanoparticle embedding studies on polystyrene, where the timescale of embedding was found to be linearly dependent on the sphere size [24].

6.4 Estimated Surface Size and Diffusion Coefficient

The data collected in this experiment also allows us to make an estimate of the depth of the mobile surface layer. By subtracting the initial volume of the nanoparticle from the volume after engulfment we can obtain the volume of material which has been displaced during the engulfment process. This volume can then be equated to the volume of a thin toroidal section.

$$V_{final} - V_o = \pi \left(R_2^2 - R_1^2\right) \xi \tag{6.2}$$

Where V_{final} is the volume of a nanoparticle after engulfment, V_o is the initial nanoparticle volume, ξ is the depth of the surface layer, and R_1 and R_2 are the inner and outer radii of the toroidal section. The inner radius can be estimated as the radius at which the buildup of material ends. From figure 6.12 we see that for the 20 nm spheres this value is approximately 200 nm. The outer radius is estimated based on the *depletion zone*.

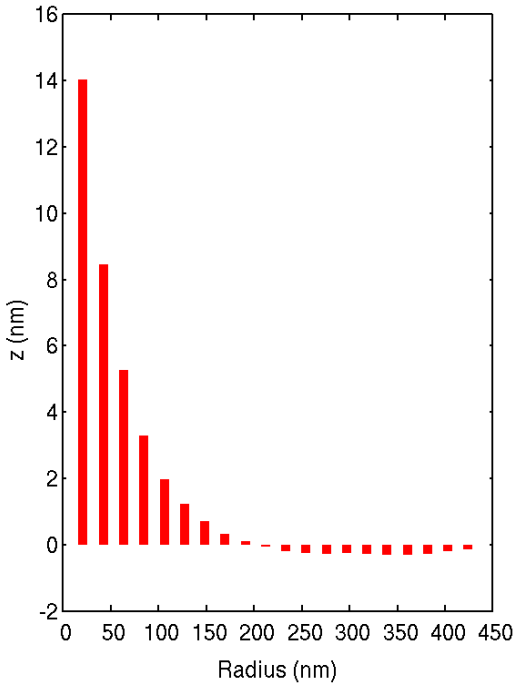

Figure 6.13: An example image displaying the depletion zone.

As the buildup of material is formed it removes TNB material from the surrounding area, creating a dip in the surface which we call the depletion zone. This depletion zone can only be seen in the early stages of the engulfment process; the depletion zone also represents an unfavourable curvature and over time material will move in to smooth away the depletion zone. It should also be noted that as material moves towards the sphere new material will be exposed to the free surface and one should expect that this material will soon become part of the mobile surface after some rejuvenation time. Figure 6.13 shows an example where the depletion zone is visible, in this image the data has been coarsened through a binning process. Based on the position of the depletion zone in this image we use a value of 500 nm for the outer radius. Figure 6.14 plots this estimated surface depth ξ versus temperature for all temperatures studied. We find the surface depth to be less than 1 nm, and is temperature dependent decreasing in size with decreasing temperature. This is in contrast to the expected temperature dependence of a cooperatively rearranging region (CRR), the characteristic length scale suggested by the Adam-Gibbs theory discussed in chapter (4). The theory suggests that in the glassy state molecular rearrangements happen in a cooperative manner over some length scale which monotonically increases with decreasing

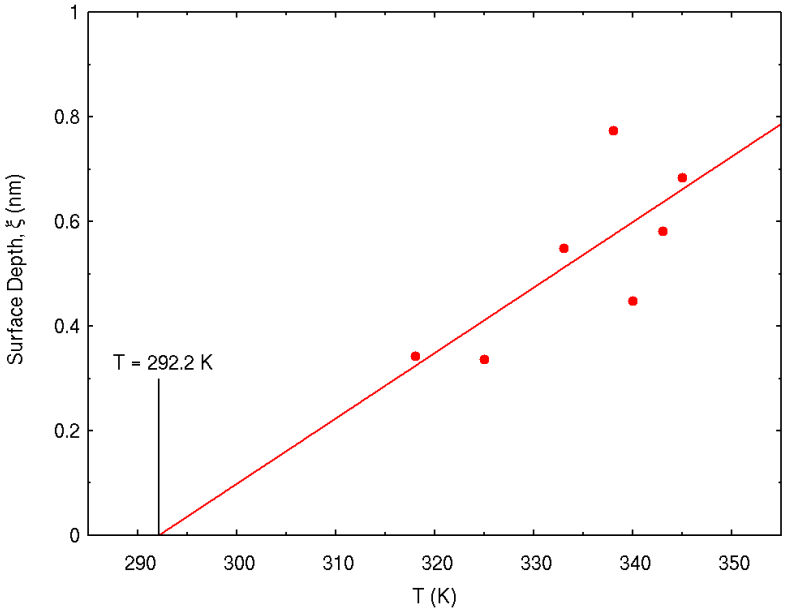

Figure 6.14: Plot of the estimated surface depth versus temperature. The volume after 80 minutes of annealing was used for V_{final} for all data sets except T = 325 K and 333 K where t = 40 and 75 were used respectively.

temperature. Since our surface depth here represents the length scale over which the dynamics are enhanced relative to the bulk, it is tempting to think that this surface depth may be connected to the size of a CRR. Given the different temperature dependencies we note that they cannot be the same quantity. In trying to reconcile a similar observation coming from the nanoparticle embedding studies on PS, Ilton et al. considered a model in which the sample's rheological temperature varied smoothly from a value at the free surface to the bulk temperature over some length scale λ. They associate this length scale with the length scale of cooperativity and show it to be increasing with decreasing temperature. The surface depth estimated here (and equivalently in the PS embedding studies) should be identified as the depth over which the rheological temperature is high enough to provide relaxation on the relevant timescale.

From this result we can do a further calculation to estimate the surface diffusion coefficient. Using the diffusion law we can write,

$$(R_2 - R_1)^2 = 4Dt \tag{6.3}$$

Subbing this into equation 6.2 we find,

$$V(t) - V_o = \pi (4Dt)\,\xi + 2\pi R_1 (R_2 - R_1)\,\xi \tag{6.4}$$

which can be rearranged and solved for the diffusion coefficient, D. In figure 6.15 we present the results of this calculation alongside other estimates of the diffusion coefficient of supercooled and glassy TNB films. We see from this plot that the surface diffusion is orders of magnitude faster than the bulk diffusion at temperatures below T_g. Furthermore our results are in line with earlier neutron reflectivity measurements of the surface diffusion; specifically in the weak temperature dependence of the surface diffusion coefficient.

6.5 Comparison To Polymer Studies

As mentioned earlier, the motivation for these studies was to see how the dynamical properties of the free surface of a molecular glass forming system would compare to the studies on polymer systems. Our first observation is that the free surface of TNB films well below T_g is more mobile than the glassy material in the interior of the film. This is evident in the existence of a surface relaxation process for all of the temperatures studied.

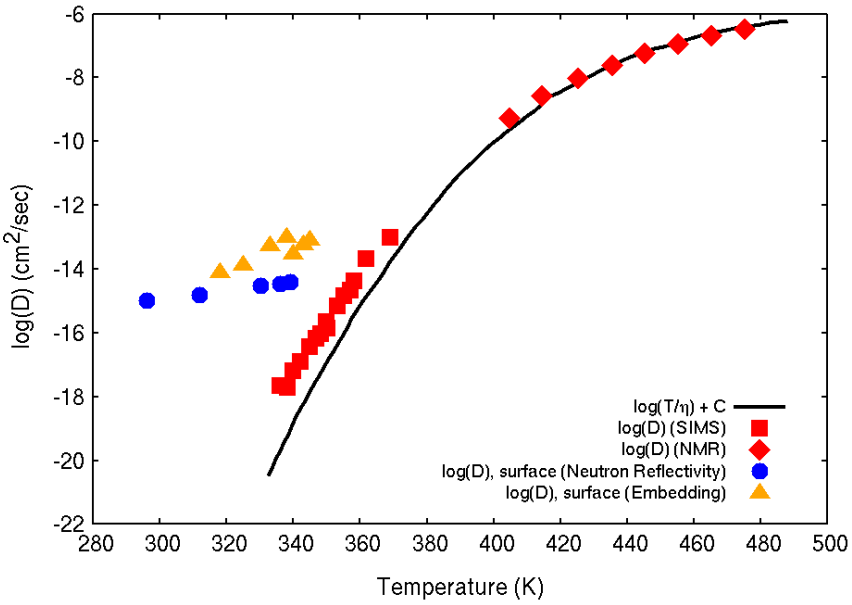

Figure 6.15: Plot of the TNB diffusion coefficient versus temperature as determined from a number of experiments. NMR measurements on supercooled TNB films (Chang et al. [107], red diamonds), SIMS measurements on supercooled TNB (Swallen et al. [101], red squares), neutron reflectivity measurements on glassy TNB films (Swallen et al. [108], blue circles), nanoparticle embedding on glassy TNB films (Present study, orange triangles), a vertically shifted plot of $\log(T/\eta)$ (Based on form of Plazek et al. [109], solid black line).

We know from the work of Forrest and coworkers [95, 96, 97, 24, 23, 94, 93] and others [91, 92, 105, 86, 85, 84, 87, 88, 89, 90] that the free surfaces of thin glassy PS and PMMA films also show an effect of enhanced surface mobility. When compared to the current study we see that there is a qualitative difference in the surface relaxation process observed in the nanoparticle embedding studies on PS [95, 96, 97, 24]. In those studies the enhanced surface mobility was displayed as an embedding of the nanoparticles into the film for temperatures below T_g. Here we find a different surface relaxation process, nanoparticle engulfment. The absence of this process for polymers is understood by the restrictions on molecular diffusion imposed by the macromolecular nature of polymers. The polymer systems studied were all well above the entanglement molecular weight M_e which greatly reduces the translational motions of chains in the melt. When the size of these coils is considered it is found that the radius of gyration of the chains is larger than the estimated depth of the mobile surface region, ~ 5 nm. Thus in the glassy state, one expects the large majority of chain segments in the mobile surface layer to be entangled with immobile chains below the surface layer. With these ideas in mind it is then no surprise that nanoparticle engulfment is not observed in those studies. Recently we have begun conducting nanoparticle embedding studies on low molecular weight PS (less then M_e) and initial observations show that the nanoparticle engulfment process is present. The embedding behaviour of the surface process in PS films is then viewed as the alternative relaxation process when chain diffusion is not possible.

Our next observation from the current studies is that for glassy TNB films at temperatures $\lesssim T_g$ two processes are observed; a fast surface process and a slower process attributed to relaxation of material deeper into the film. A comparison should be made between figures 6.10 and 6.16. Figure 6.16 represents the embedding behaviour of nanoparticles on PS for temperatures spanning across T_g down to about $T_g - 80$ K [24]. The comparison is quite striking, with the exception of the additional middle process in the case of PS, the plots are remarkably similar[1]. Both systems exhibit a weakly temperature dependent surface process which persists well below T_g and a strongly temperature dependent process owing to relaxation of material in the bulk of the film. In both systems the slower bulk like process is well described by the VTF equation. The intersection temperature T_{int} is also found to be similar for the two systems, for TNB we have observed $T_{int} = T_g + 12$ K

[1]The middle process is thought to be a strictly polymeric effect as a result of entanglements in the polymer network

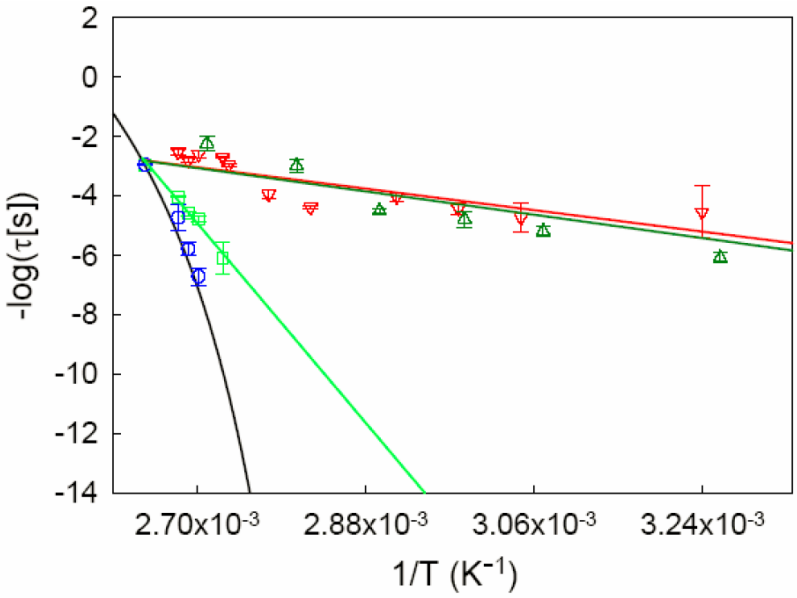

Figure 6.16: Dependence of the observed relaxation times on temperature for the case of PS. The fastest process (triangles) is the surface process, the slowest relaxation (circles) is the bulk material, and the intermediate process (squares) is a sub-surface layer relaxation. Image reproduced from [24].

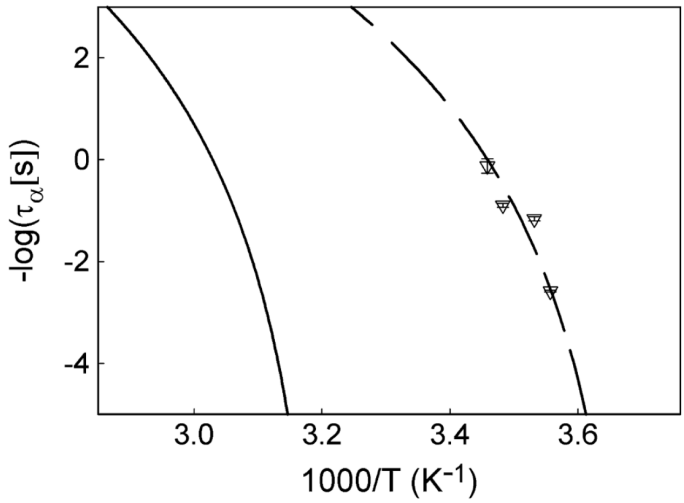

Figure 6.17: Plot illustrating the dependence of the relaxation time of surface nanodeformations on temperature for the case of i-PMMA on silicon. The dashed curve is determined by a shift in the reference temperature for the bulk relaxation curve (solid curve). Image reproduced from [94].

and for PS previous studies found $T_{int} = T_g + 9$ K.

We can also compare our results to surface asperity relaxation studies on PMMA [94, 91, 92]. From those studies we see that the temperature dependence of the surface relaxation process in PMMA is qualitatively different from the cases of PS and TNB. Figure 6.17 plots the relaxation times for i-PMMA as determined from surface nanohole relaxation studies. The study shows the existence of enhanced surface mobility in i-PMMA, but the surface relaxation has a temperature dependence which appears to be the same as the bulk system shifted to lower temperatures. This is in stark contrast to the findings of this study and those on PS where the surface process is found to have a much weaker temperature dependence than the bulk. The differences in chemical structure between PMMA and PS have previously been suggested as the cause for this contrast [94]. It is then possible that the striking similarity between the PS and TNB surfaces may be related to the similarities in their molecular chemistry. PS and TNB molecular structures are shown in figures 4.1 and 5.1 respectively.

6.6 Conclusions

This is not the first study to observe the effects of an enhanced surface mobility in a molecular glass, however it may be the most convincing and direct. Bell et al. [110] tracked the diffusion of ions into a molecular glass 3-methylpentane upon heating from deep in the glassy state. They found that diffusion began some ~ 25 K below the bulk glass transition suggesting enhanced mobility at the free surface. Swallen et al. [100] indirectly observed the effect of enhanced surface mobility during vapour deposition of TNB glass films. The authors find that when deposition is performed at a temperature of $0.85T_g$ the result is a highly stable glass film. They attribute the stability to enhanced mobility on the films surface during the slow deposition process; as material is deposited it can quickly rearrange to find a low energy configuration. For the most part studies on molecular glass dynamics have been restricted to systems under confinement in nanopores making direct comparisons to this work troublesome. Comparisons are more readily drawn to studies on the surface properties of polymers, discussed above (section 6.5). The similarities between TNB and PS are remarkable given the differences in molecular *structure*. Both systems show an enhanced mobility in the vicinity of the free surface with a surface relaxation process which is very weakly dependent on temperature. In contrast PMMA also shows an enhanced surface mobility but with a temperature dependence well described by bulk dynamics shifted to lower temperatures. This seems to suggest that the similarities between PS and TNB may be related to similarities in their molecular *chemistry*.

This study shows direct and conclusive evidence that the TNB surface dynamics are enhanced relative to the bulk. Contributing to the growing body of literature on surface dynamics in glassy systems this result adds substantial weight to the view that enhanced surface mobility is a universal property of glass forming systems. This suggests that effects such as chain confinement, stress induced during spin coating, and chain end enrichment, brought up in suggesting that enhanced surface mobility is strictly a polymeric effect, do not play a role in the development of enhanced surface dynamics.

In large the field of glassy systems under confinement is directed by experimental studies and in general theoretical approaches fall short in explaining more than a specific subset of experimental observations. Computer simulations are a promising avenue of research, however do to the inherent complexity of glassy systems great care must be taken both in performing the simulations and in interpreting the validity of their findings. Some key

issues that future studies should aim at addressing are as follows. One important question relates to the observation of the strong molecular weight dependence in T_g measurements on freely-standing films. It is curious that this molecular weight is entirely absent in supported films. If T_g reductions are intimately connected to the free surface mobility as many believe than it is of great interest to study the free surface properties of freely standing films. It seems this question could be partially addressed by a measure of the spacial extent through which interfaces effect local dynamics. Although fluorescence studies on multilayer films have attempted to address this question by measuring 'local' T_g's, there is cause for concern in that T_g is an indirect measure of dynamics. Another outstanding issue is that of the physical significance of the size of the mobile surface layer and it's possible connection to the length scale over which dynamics are correlated. Studies focusing on these issues are sure to have a significant impact on the intense and exciting area of research of confined glassy materials.

Appendix A

A.1 Binning Volume Analysis Programs

The following is a Fortran program (and module) written to perform the binning analysis used for analysing the TNB data. Similar programs have been used in the volume analysis, and embedding analysis but they only differ in the relatively simple calculations that are performed in place of the binning process so this program has been provided as the example. The main program file and the processing module follow.

A.1.1 Main Program File

```
Program Main
 !*********************************************************************
 !Progam reads in series of AFM data files, averages over all images
 !of a particular time, and coarsens the averaged data by binning data
 !coarsened data is written to file. It is hardcoded for use on images
 !with 200x200 data points at a resolution of 6nm.
 !*********************************************************************
 use process_mod
 implicit none
 !---------------------------------------------------------------------
 !Variable Definitions
 !---------------------------------------------------------------------
 !z is the raw data read in from file, z_crop is this data after
```

```
!after processing, z_avg is the average over all z_crop's.
!Radii is like a dual matrix to z_crop where each entry's value equals
!it's radius, reduces computations during binning process
!histo is a N*3 matrix, N is determined by the desired number of bins,
!the first column filled with the radii which separate the different
!bins, all data which falls into a certain region is added to the
!corresponding element of the second dimension, and the third
!dimension records the number of entries into a bin.
!The various character strings are used for handling file names.

real :: z(1:200,1:200), z_crop(-50:50,-50:50), z_avg(-50:50,-50:50)
real :: Radii(-50:50,-50:50)
real, allocatable :: histo(:,:)
real :: r
integer :: a,b
integer :: i,j,k,m
integer, parameter :: n = 20 !This is the number of bins
character(len=1024) :: filename,time,dir,filelist,tmpfilename
character(len=512), DIMENSION(50) :: timelist
!*********************************************************************
!*********************************************************************
!Program will look in 'directory' for filelists corresponding to the
!times listed in timelist. It opens the files listed in that filelist
!and processes the data.
!*********************************************************************
!*********************************************************************
!Set directory and timelist here
!These are the only things that ever need to be changed

timelist(1:13) = (/"0","2","5","10","20","40","80","167","310", &
     "705","1255","2455","END"/)
dir ='../Datafiles/May3_BigSpheres/'
!--------------------------------------------------------------------
```

```
!Prepare histogram array

allocate(histo(1:n,1:3))
do i=1,n,1
   histo(i,1) = sqrt(5000.0)/n*i
end do
!---------------------------------------------------------------------
!Prepare Radii matrix

do i=-50,50,1
   do j=-50,50,1
      Radii(i,j) = (i**2)+(j**2)
   enddo
enddo
Radii = sqrt(Radii)
!*********************************************************************
!*********************************************************************
do m = 1,999,1
   !-----------------------------------------------------------------
   !Open filelist corrsponding to the m'th time in timelist
   if(timelist(m).eq.'END') EXIT
   tmpfilename = TRIM(dir)//"filelist_"//TRIM(timelist(m))//"min.txt"
   open(13,file=tmpfilename,status='old')
   read(13,*) time
   !-----------------------------------------------------------------
   !Write info to terminal
   write(*,*) '*****************************************************'
   write(*,'(A25,A80)') 'USING FILELIST:          ', tmpfilename
   write(*,'(2A10)') 'TIME =    ', time
   if(time.eq.'0') time = '0.1'
   !-----------------------------------------------------------------
   !Zero quantities
   z = 0.0
```

```
z_crop = 0.0
z_avg = 0.0
histo(:,2) = 0
histo(:,3) = 0
!*****************************************************************
!Read in filenames from the filelist unit, until 'END' is read in
!*****************************************************************
do i=1,999,1
   !---------------------------------------------------------------
   read(13,*) filename
   if(filename.eq.'END') EXIT
   tmpfilename = TRIM(dir)//TRIM(filename)
   open(14,file=tmpfilename,status='old')
   !---------------------------------------------------------------
   !Read in the z data from currently open file
    read(14,*) !read over header
   read(14,*) z !reads in 200x200 matrix
   !---------------------------------------------------------------
   !Call process routine to center/crop about NP peak, and level to
   !a baseline value. a & b are the peak coordinates in z.
    call process(z,z_crop,a,b)
   !---------------------------------------------------------------
   !Add to the running average for this time
   z_avg = z_avg + z_crop
   close(14)
end do
!*****************************************************************
!*****************************************************************
!Average the cropped data

z_avg = z_avg/(i-1)
!---------------------------------------------------------------
!Binning the data:
```

```
    !Go through each element of z_avg and add it's value to the correct
    !histo bin, based on the radius of each point. The values go into
    !the second column of histo, the third column keeps track of the
    !number of values added into that bin.
     do i =-50,50,1
       do j= -50,50,1
          r = Radii(i,j)
          do k = 1,n,1
             if(r.le.histo(k,1))then
                histo(k,2) = histo(k,2) + z_avg(i,j)
                histo(k,3) = histo(k,3) + 1
                r = 999999
             end if
          end do
       end do
    end do
    !---------------------------------------------------------------------
    !Average by dividing row 2 by row 3
    histo(:,2) = histo(:,2)/histo(:,3)
    !---------------------------------------------------------------------
    !open file to save binned data to and write to it.
     tmpfilename = TRIM(dir)//"histo_"//TRIM(time)//"min"//".txt"
    open(17,file=tmpfilename,status='unknown')
    do i = 1,n,1
       write(17,*) histo(i,1) ,histo(i,2)
    end do
    close(17)
    close(13)
    !*********************************************************************
    !*********************************************************************
 end do
end Program Main
```

A.1.2 Processing Module

```
module process_mod
 !=====================================================================
 !Contains a subroutine which takes a 200x200 matrix, finds the peak
 !location, subtracts off the baseline value (ignoring points within
 !50 pixels of the peak), and generates a 101x101 matrix centered on
 !the peak position.
 !=====================================================================
contains
 subroutine process(z,z_crop,a,b)
   implicit none
   !---------------------------------------------------------------------
   !Variable Definition

   real :: z(1:200,1:200), z_crop(1:101,1:101)
   real :: base
   integer :: max_coord(2)
   integer :: a,b
   !---------------------------------------------------------------------
   !Find the index of the NP peak

   max_coord = maxloc(z)
   a = max_coord(1)
   b = max_coord(2)
   !---------------------------------------------------------------------
   !Ignoring values within 50 points of peak, determine baseline,
   !subtract this baseline from all data points

   base = SUM(z(1:a-51,1:200)) + SUM(z(a-50:a+50,1:b-51)) + &
        SUM(z(a-50:a+50,b+51:200)) + SUM(z(a+51:200,1:200))
   base = base/( SIZE(z(1:a-51,1:200)) + SIZE(z(a-50:a+50,1:b-51)) + &
        SIZE(z(a-50:a+50,b+51:200)) + SIZE(z(a+51:200,1:200))  )
```

```
   z = z - base
   !---------------------------------------------------------------------
   !Select only data within 50x50points area of peak

   z_crop = z(a-50:a+50,b-50:b+50)
   !---------------------------------------------------------------------
 end subroutine process
 !=====================================================================
end module process_mod
```

Bibliography

[1] Kelly K.L., Coronado E., Zhao L.L., Schatz G.C., *The Optical Properties of Metal Nanoparticles: The Influence of Size, Shape, and Dielectric Environment*, The Journal of Physical Chemistry B, **107**, p. 668, 2003. 3, 5

[2] Link S., El-Sayed M.A., *Shape and size dependence of radiative, non-radiative and photothermal properties of gold nanocrystals*, International Reviews in Physical Chemistry, **19**, p. 409, 2000. 4, 5

[3] Huang X., El-Sayed I.H., Qian W., El-Sayed M.A., *Cancer Cell Imaging and Photothermal Therapy in the Near-Infrared Region by Using Gold Nanorods*, Journal of the American Chemical Society, **128**, p. 2115, 2006. 5

[4] Sosa I.O., Noguez C., Barrera R.G., *Optical Properties of Metal Nanoparticles with Arbitrary Shapes*, The Journal of Physical Chemistry B, **107**, p. 6269, 2003. 5

[5] Chen J., Wang D., Xi J., Au L., Siekkinen A., Warsen A., Li Z.Y., Zhang H., Xia Y., Li X., *Immuno Gold Nanocages with Tailored Optical Properties for Targeted Photothermal Destruction of Cancer Cells*, Nano Letters, **7**, p. 1318, 2007. 5

[6] Loo C., Lowery A., Halas N., West J., Drezek R., *Immunotargeted Nanoshells for Integrated Cancer Imaging and Therapy*, Nano Letters, **5**, p. 709, 2005. 5

[7] Gobin M., Lee M.H., Halas N.J., James W.D., Drezek R.A., West J.L., *Near-Infrared Resonant Nanoshells for Combined Optical Imaging and Photothermal Cancer Therapy*, Nano Letters, **7**, p. 1929, 2007. 5

[8] Weissleder R., *A clearer vision for in vivo imaging*, Nature Biotechnology, **19**, p. 316, 2001. 6

[9] Gao X., Cui Y., Levenson R.M., Chung L.W.K., Nie S., *In vivo cancer targeting and imaging with semiconductor quantum dots*, Nature Biotechnology, **22**, p. 969, 2004. 8

[10] Pustovalov V.K., Smetannikov A.S., Zharov V.P., *Photothermal and accompanied phenomena of selective nanophotothermolysis with gold nanoparticles and laser pulses*, Laser Physics Letters, **5**, p. 775, 2008. 9

[11] Huang X., Jain P.K., El-Sayed I.H., El-Sayed M.A., *Determination of the Minimum Temperature Required for Selective Photothermal Destruction of Cancer Cells with the Use of Immunotargeted Gold Nanoparticles*, Photochemistry and Photobiology, **82**, p. 412, 2006. 9, 10

[12] Pitsillides C.M., Joe E.K., Wei X., Anderson R.R., Lin C.P., *Selective Cell Targeting with Light-Absorbing Microparticles and Nanoparticles*, Biophysical Journal, **84**, p. 4023, 2003. 10, 11

[13] Goldenberg H., Tranter C.J., *Heat flow in an infinite medium heated by a sphere*, British Journal of Applied Physics, **3**, p. 296, 1952. 10

[14] Zharov V.P., Galitovskiy V., Lyle C.S., Chambers T.C., *Superhigh-sensitivity photothermal monitoring of individual cell response to antitumor drug*, Journal of Biomedical Optics, **11**, p. 064034, 2006. 11

[15] Kurita H., Takami A., Kodaa S., *Size reduction of gold particles in aqueous solution by pulsed laser irradiation*, Applied Physics Letters, **72**, p. 789, 1998. 11

[16] Zharov V.P., Mercer K.E., Galitovskaya E.N., Smeltzer M.S., *Photothermal Nanotherapeutics and Nanodiagnostics for Selective Killing of Bacteria Targeted with Gold Nanoparticles*, Biophysical Journal, **90**, p. 619, 2006. 12

[17] Letfullin R.R., George T.F., Duree G.C., Bollinger B.M., *Ultrashort Laser Pulse Heating of Nanoparticles: Comparison of Theoretical Approaches*, Advances in Optical Technologies, **2008**, p. 251718, 2008. 12, 13

[18] ONeal D.P., Hirschb L.R., Halasc N.J., Paynea J.D., West J.L., *Photo-thermal tumor ablation in mice using near infrared-absorbing nanoparticles*, Cancer Letters, **209**, p. 171, 2004. 13

[19] Hirsch L.R., Stafford R.J., Bankson J.A., Sershen S.R., Rivera B., Price R.E., Hazle J.D., Halas N.J., West J.L., *Nanoshell-mediated near-infrared thermal therapy of tumors under magnetic resonance guidance*, Proceedings of the National Academy of Sciences, **100**, p. 13549, 2003. 14

[20] Glogowski E., He J., Russell T.P., Emrick T., *Mixed monolayer coverage on gold nanoparticles for interfacial stabilization of immiscible fluids*, Chemical Communications, **2005**, p. 4050, 2005. 16, 17

[21] Brust M., Walker M., Bethell D., Schiffrin D.J., Whyman R., *Synthesis of Thiol-derivatised Gold Nanoparticles in a Two-phase Liquid-Liquid System*, Journal of the Chemical Society, Chemical Communications, **1994**, p. 801, 1994. 16

[22] Du H., Fuh R.A., Li J., Corkan A., Lindsey J.S., *PhotochemCAD: A computer-aided design and research tool in photochemistry*, Photochemistry and Photobiology, **68**, p. 141, 1998. 19

[23] Fakhraai Z., *Dynamics of polymer thin films and surfaces*, Ph.D. thesis, University of Waterloo, 2007. 29, 72, 95, 115

[24] Qi D., *On near-free-surface dynamics of thin polymer films*, Ph.D. thesis, University of Waterloo, 2009. 29, 31, 74, 76, 77, 78, 79, 95, 110, 115, 116

[25] Strobl G., *The Physics of Polymers:Concepts for Understanding their Structure and Behaviour*, Springer, 1996. 35, 44

[26] Rubinstein M., Colby R.H., *Polymer Physics*, Oxford University Press, 2003. 35, 37, 38

[27] Doi M., Edwards S.F., *The Theory of Polymer Dynamics*, Oxford University Press, 1986. 35

[28] de Gennes P.G., *Scaling Concepts in Polymer Physics*, Cornell University Press, 1979. 35, 39

[29] Adam M., Delsanti M., *Dynamical Properties of Polymer Solutions in Good Solvent by Rayleigh Scattering Experiments*, Macromolecules, **10**, p. 1229, 1977. 37

[30] de Gennes P.G., *Reptation of a Polymer Chain in the Presence of Fixed Obstacles*, The Journal of Chemical Physics, **55**, p. 572, 1971. 40

[31] Lodge T.P., *Reconciliation of the Molecular Weight Dependence of Diffusion and Viscosity in Entangled Polymers*, Physical Review Letters, **83**, p. 3218, 1999. 42

[32] Klement W., Willens R.H., Duwez P., *Non-crystalline Structure in Solidified Gold-Silicon Alloys*, Nature, **187**, p. 869, 1960. 45

[33] Sano Y., Nishio K., Koga J., Yamaguchi T., Yonezawa F., *Simulational study of glass transition in argon*, Journal of Non-Crystalline Solids, **345**&**346**, p. 546, 2004. 45

[34] Ediger M.D., Angell C.A., Nagel S.R., *Supercooled Liquids and Glasses*, The Journal of Physical Chemistry, **100**, p. 13200, 1996. 46, 48

[35] Kauzmann W., *The Nature of the Glassy State and the Behavior of Liquids at Low Temperatures*, Chemical Reviews, **43**, p. 219, 1948. 47

[36] Kearns K.L., Swallen S.F., Ediger M.D., Wu T., Sun Y., Yu L., *Hiking down the Energy Landscape: Progress Toward the Kauzmann Temperature via Vapor Deposition*, The Journal of Physical Chemistry B, **112**, p. 4934, 2008. 48

[37] Adam G., Gibbs J.H., *On the Temperature Dependence of Cooperative Relaxation Properties in Glass-Forming Liquids*, The Journal of Chemical Physics, **43**, p. 139, 1965. 49, 50, 51

[38] Donati C., Douglas J.F., Kob W., Plimpton S.J., Poole P.H., Glotzer S.C., *Stringlike Cooperative Motion in a Supercooled Liquid*, Physical Review Letters, **80**, p. 2338, 1998. 49

[39] Hurley M.M., Harrowell P., *Kinetic structure of a two-dimensional liquid*, Physical Review E, **52**, p. 1694, 1995. 49

[40] Weeks E.R., Crocker J.C., Levitt A.C., Schofield A., Weitz D.A., *Three-Dimensional Direct Imaging of Structural Relaxation Near the Colloidal Glass Transition*, Science, **287**, p. 627, 2000. 50

[41] Berthier L., Biroli G., Bouchaud J.-P., Cipelletti L., El Masri D., L'Hôte D., Ladieu F., Pierno M., *Direct Experimental Evidence of a Growing Length Scale Accompanying the Glass Transition*, Science, **310**, p. 1797, 2005. 50

[42] Kegel W.K., van Blaaderen A., *Direct Observation of Dynamical Heterogeneities in Colloidal Hard-Sphere Suspensions*, Science, **287**, p. 290, 2000. 50

[43] Turnbull D., Cohen M.H., *Free-Volume Model of the Amorphous Phase: Glass Transition*, The Journal of Chemical Physics, **34**, p. 120, 1961. 51

[44] Cohen M.H., Turnbull D., *Molecular Transport in Liquids and Glasses*, The Journal of Chemical Physics, **31**, p. 1164, 1959. 51

[45] Hirschfelder J., Stevenson D., Eyring H., *A Theory of Liquid Structure*, The Journal of Chemical Physics, **5**, p. 896, 1937. 51

[46] Ferrer M.L., Lawrence C., Demirjian B.G., Kivelson D., Alba-Simionesco C., Tarjus G., *Supercooled liquids and the glass transition: Temperature as the control variable*, The Journal of Chemical Physics, **109**, p. 8010, 1998. 52

[47] Jäckle J., *Models of the glass transition*, Report on Progress in Physics, **49**, p. 171, 1986. 52

[48] Leutheusser E., *Dynamical model of the liquid-glass transition*, Physical Review A, **29**, p. 2765, 1984. 52

[49] Bengtzelius U., Götze W., Sjölander A., *Dynamics of supercooled liquids and the glass transition*, Journal of Physics C, **17**, p. 5915, 1984. 52

[50] Cummins H.Z., Li G., Hwang Y.H., Shen G.Q., Du W.M., Hernandez J., Tao N.J., *Dynamics of supercooled liquids and glasses: comparison of experiments with theoretical predictions*, Zeitschrift Für Physik B, **103**, p. 501, 1997. 52, 53

[51] Kob W., *The mode-coupling theory of the glass transition*, Supercooled Liquids, **676**, p. 28, 1997. 52

[52] Donth E., *The glass transition: relaxation dynamics in liquids and disordered materials*, Springer, 2001. 52

[53] Götze W., Sjögren L., *Scaling properties in supercooled liquids near the glass transition*, Journal of Physics C, **21**, p. 3407, 1988. 54

[54] Edwards S.F., Evans K.E., *Dynamics of Highly Entangled Rod-like Molecules*, Journal of the Chemical Society, Faraday Transactions 2, **78**, p. 113, 1982. 55, 56

[55] Edwards S.F., Vilgis Th., *The Dynamics of the Glass Transition*, Physica Scripta, **T13**, p. 7, 1986. 57

[56] Jackson C.L., McKenna G.B., *The glass transition of organic liquids confined to pores*, Journal of Non-Crystalline Solids, **131**, p. 221, 1991. 58, 59

[57] Zhang J., Liu G., Jonas J., *Effects of confinement on the glass transition temperature of molecular liquids*, Journal of Physical Chemistry, **96**, p. 3478, 1992. 58, 59

[58] C., Dosseh G., Dumont E., Frick B., Geil B., Morineau D., Teboul V., Xia Y., *Confinement of molecular liquids: Consequences on thermodynamic, static and dynamical properties of benzene and toluene*, European Physical Journal E, **12**, p. 19, 2003. 59

[59] Park J.Y., McKenna G.B., *Size and confinement effects on the glass transition behavior of polystyrene/o-terphenyl polymer solutions*, Physical Review B, **61**, p. 6667, 2000. 59

[60] Arndt M., Stannarius R., Groothues H., Hempel E., Kremer F., *Length scale of cooperativity in the dynamic glass transition*, Physical Review Letters, **79**, p. 2077, 1997. 59, 60

[61] Arndt M., Stannarius R., Gorbatschow W., Kremer F., *Dielectric investigations of the dynamic glass transition in nanopores*, Physical Review E, **54**, p. 5377, 1996. 59, 60

[62] Schüller J., Richert R., Ficsher E.W., *Dielectric relaxation of liquids at the surface of a porous glass*, Physical Review B, **52**, p. 15232, 1995. 59, 60, 61

[63] KobWand Binder K Scheidler P, *Cooperative motion and growing length scales in supercooled confined liquids*, Europhysics Letters, **59**, p. 701, 2002. 59

[64] Schüller J., Mel'nichenko Yu.B., Richert R., Fischer E.W., *Dielectric studies of the glass transition in porous media*, Physical Review Letters, **73**, p. 2224, 1994. 59, 61

[65] Pissis P., Daoukaki D., Apekis L., Christodoulides C., *The glass transition in confined liquids*, Journal of Physics: Condensed Matter, **6**, p. L325, 1994. 61

[66] Gorbatschow W., Arndt M., Stannarius R., Kremer F., *Dynamics of H-bonded liquids confined to nanopores*, Europhysics Letters, **35**, p. 719, 1996. 61

[67] Melnichenko Y.B., Schuller J., Richert R., Ewen B., Loong C.K., *Dynamics of hydrogen-bonded liquids confined to mesoporesA dielectric and neutron spectroscopy study*, Journal of Chemical Physics, **103**, p. 2016, 1995. 61

[68] Keddie J.L., Jones R.A.L., Cory R.A., *Size-Dependent Depression of the Glass Transition Temperature in Polymer Films*, Europhysics Letters, **27**, p. 59, 1994. 62, 64

[69] Beaucage G., Composto R., Stein R.S., *Ellipsometric study of the glass transition and thermal expansion coefficients of thin polymer films*, Journal of Polymer Physics B, **31**, p. 319, 1993. 62

[70] DeMaggio G.B., Frieze W.E., Gidley D.W., Zhu M., Hristov H.A., Yee A.F., *Interface and Surface Effects on the Glass Transition in Thin Polystyrene Films*, Physical Review Letters, **78**, p. 1524, 1997. 62

[71] Fukao K., Miyamoto Y., *Glass transitions and dynamics in thin polymer films: Dielectric relaxation of thin films of polystyrene*, Physical Review E, **61**, p. 1743, 2000. 62

[72] Fukao K., Miyamoto Y., *Glass transition temperature and dynamics of alpha-process in thin polymer films*, Europhysics Letters, **46**, p. 649, 1999. 62

[73] Forrest J.A., Dalnoki-Veress K., Dutcher J.R., *Interface and chain confinement effects on the glass transition temperature of thin polymer films*, Physical Review E, **56**, p. 5705, 1997. 62, 65

[74] Wallace W.E., van Zanten J.H., Wu W., *Influence of an impenetrable interface on a polymer glass-transition temperature*, Physical Review E, **52**, p. R3329, 1995. 62

[75] Dalnoki-Veress K., Forrest J.A., *The glass transition in thin polymer films*, Advances in Colloid and Interface Science, **94**, p. 167, 2001. 63, 65

[76] Prucker O., Christian S., Bock H., Ruhe J., Frank C.W., Knoll W., *On the glass transition in ultrathin polymer films of different molecular architecture*, Macromolecular Chemistry and Physics, **199**, p. 1435, 1998. 64

[77] Kim J.H., Jang J., , Zin W.C., *Estimation of the thickness dependence of the glass transition temperature in various thin polymer films*, Langmuir, **16**, p. 4064, 2000. 64

[78] Kim J.H., Jang J., , Zin W.C., *Thickness dependence of the glass transition temperature in thin polymer films*, Langmuir, **17**, p. 2703, 2001. 64

[79] Keddie J.L., Jones R.A.L., Cory R.A., *Interface and surface effects on the glass transition temperature in thin polymer films*, Faraday Discussions, **98**, p. 219, 1994. 64, 73

[80] Grohens Y., Hamon L., Reiter G., Soldera A., Holl Y., *Some relevant parameters affecting the glass transition of supported ultra-thin polymer films*, European Physical Journal E, **8**, p. 217, 2002. 64, 73

[81] Dalnoki-Veress K., Forrest J.A., Murray C., Gigault C., Dutcher J.R., *Molecular weight dependence of reductions in the glass transition temperature of thin freely standing polymer films*, Physical Review E, **63**, p. 031801, 2001. 65

[82] Mattsson J., Forrest J.A., Börgesson L., *Quantifying glass transition behavior in ultrathin free-standing polymer films*, Physical Review E, **62**, p. 5187, 2000. 65

[83] de Gennes P.G., *Glass transitions in thin polymer films*, European Physical Journal E, **2**, p. 201, 2000. 66

[84] Ellison C.J., Torkelson J.M., *Sensing the glass transition in thin and ultrathin polymer films via fluorescence probes and labels*, Journal of Polymer Science B, **40**, p. 2745, 2002. 66, 95, 115

[85] Ellison C.J., Kim S.D., Hall D.B., Torkelson J.M., *Confinement and processing effects on glass transition temperature and physical aging in ultrathin polymer films*, European Physical Journal E, **8**, p. 155, 2002. 66, 95, 115

[86] Ellison C.J., Torkelson J.M., *The distribution of glass-transition temperatures in nanoscopically confined glass formers*, Nature Materials, **2**, p. 695, 2003. 66, 67, 68, 95, 115

[87] Roth C.B., McNerny K.L., Jager W.F., Torkelson J.M., *Eliminating the enhanced mobility at the free surface of polystyrene: Fluorescence studies of the glass transition tmperature in thin bilayer films of immiscible polymers.*, Macromolecules, **40**, p. 2568, 2007. 67, 95, 115

[88] Kerle T., Lin Z., Kil H.C., Russell T.P., *Mobility of polymers at the air/polymer interface*, Macromolecules, **34**, p. 3484, 2001. 69, 70, 95, 115

[89] Buck E., Petersen K., Hund M., Krausch G., Johannsmann D., *Decay kinetics of nanoscale corrugation gratings on polymer surface: evidence for polymer flow below the glass temperature*, Macromolecules, **37**, p. 8647, 2004. 69, 95, 115

[90] Gasemjit p., Johannsmann D., *Thickness of the soft layer on glassy polystyrene surfaces*, Journal of Polymer Science B, **44**, p. 3031, 2006. 69, 70, 95, 115

[91] Papaléo R.M., Leal R., Carreira W.H., Barbosa L.G., *Relaxation times of nanoscale deformations on the surface of a polymer thin film near and below the glass transition*, Physical Review B, **74**, p. 094203, 2006. 71, 72, 95, 115, 117

[92] Grohens Y., Papaleo R.M., Hamon L., *Ion crater healing and variable temperature ellipsometry as complementary probes for the glass transition in thin polymer films*, European Physical Journal E, **12**, p. S81, 2003. 71, 95, 115, 117

[93] Fakhraai Z., Forrest J.A., *Measuring the Surface Dynamics of Glassy Polymers*, Science, **319**, p. 600, 2008. 71, 73, 79, 95, 115

[94] Qi D., Fakhraai Z., Forrest J.A., *Substrate and Chain Size Dependence of Near Surface Dynamics of Glassy Polymers*, Physical Review Letters, **101**, p. 096101, 2008. 71, 73, 74, 75, 95, 115, 117

[95] Teichroeb J.H., Forrest J.A., *Direct Imaging of Nanoparticle Embedding to Probe Viscoelasticity of Polymer Surfaces*, Physical Review Letters, **91**, p. 016104, 2003. 74, 95, 115

[96] Sharp J.S., Teichroeb J.H., Forrest J.A., *The properties of free polymer surfaces and their influence on the glass transition temperature of thin polystyrene films*, European Physical Journal E, **15**, p. 473, 2004. 74, 95, 115

[97] Ilton M., Qi D., Forrest J.A., *Using Nanoparticle Embedding to Probe Surface Rheology and the Length Scale of Surface Mobility in Glassy Polymers*, Macromolecules, **42**, p. 6851, 2009. 74, 95, 115

[98] Hutcheson S.A., McKenna G.B., *The properties of free polymer surfaces and their effect upon the glass transition temperature of thin polystyrene films*, Physical Review Letters, **94**, p. 076103, 2005. 76, 95

[99] Sharp J.S., Forrest J.A., Fakhraai Z., Khomenko M., Teichroeb J.H., Dalnoki-Veress K., *Reply to comment on The properties of free polymer surfaces and their effect upon the glass transition temperature of thin polystyrene films by S.A. Hutcheson and G.B. McKenna*, European Physical Journal E, **22**, p. 287, 2007. 76, 95

[100] Swallen S.F., Kearns K.L., Mapes M.K., Kim Y.S., McMahon R.J., Ediger M.D., Wu T., Yu L., Satija S., *Organic Glasses with Exceptional Thermodynamic and Kinetic Stability*, Science, **315**, p. 353, 2007. 81, 118

[101] Swallen S.F., Traynor K., McMahon R.J., Ediger M.D., Mates T.E., *Self-Diffusion of Supercooled Tris-naphthylbenzene*, Journal of Physical Chemistry B, **113**, p. 4600, 2009. 82, 114

[102] Turkevich J., Stevenson P.C., Hillier J., *A Study of the Nucleation and Growth Processes in the Synthesis of Colloidal Gold*, Discussions of the Faraday Society, **11**, p. 55, 1951. 84

[103] Binnig G., Quate C.F., Gerber Ch., *Atomic Force Microscope*, Physical Review Letters, **56**, p. 930, 1986. 86

[104] ThermoMicroscopes, 1171 Borregas Avenue Sunnyvale, California 94089, *SPMLab Version 5.01 Software Reference Manual*, August 2000. 87

[105] Buck E., Petersen K., Hund M., Krausch G., Johannsmann D., *Decay kinetics of nanoscale corrugation gratings on polymer surface: Evidence for polymer flow below the glass temperature*, Macromolecules, **37**, p. 8647, 2004. 95, 115

[106] Plazek D.J., Magill J.H., *Physical Properties of Aromatic Hydrocarbons, I. Viscous and Viscoelastic Behaviour of 1:3:5-Tri-α-Naphthyl Benzene*, The Journal of Chemical Physics, **45**, p. 3038, 1966. 106, 107

[107] Chang I., Sillescu H., *Heterogeneity at the Glass Transition: Translational and Rotational Self-Diffusion*, Journal of Physical Chemistry B, **101**, p. 8794, 1997. 114

[108] Ediger M., Swallen S., Kearns K., *Comparison of surface mobility of polymeric and low molecular weight glass-formers*, in *Bulletin of the American Physical Society*, 2008. 114

[109] Plazek D.J., Magill J.H., *Physical Properties of Aromatic Hydrocarbons, IV. An Analysis of the Temperature Dependence of the Viscosity and the Compliance of 1,3,5 Tri-α-naphthylbenzene*, The Journal of Chemical Physics, **49**, p. 3678, 1968. 114

[110] Bell R.C., Wang H., Iedema M.J., Cowin J.P., *Nanometer-Resolved Interfacial Fluidity*, Journal of the American Chemical Society, **125**, p. 5176, 2003. 118